First-Principles Investigations of Solid-State Electrolytes and Coatings for Solid-State Batteries

By

Yihan Xiao

A dissertation submitted in partial satisfaction of the

requirements for the degree of

Doctor of Philosophy

in

Engineering – Materials Science and Engineering

in the

Graduate Division

of the

University of California, Berkeley

Committee in charge:

Professor Gerbrand Ceder, Chair
Professor Mary Scott
Professor Bryan D. McCloskey

Fall 2020

Abstract

First-Principles Investigations of Solid-State Electrolytes and Coatings for Solid-State Batteries

by

Yihan Xiao

Doctor of Philosophy in

Engineering – Materials Science and Engineering

University of California, Berkeley

Professor Gerbrand Ceder, Chair

Solid-state batteries (SSBs) are considered to be the next-generation energy storage devices. By replacing the flammable organic liquid electrolyte in conventional Li-ion batteries (LIBs) with an inorganic solid-state electrolyte (SSE), SSBs hold the promise to offer increased energy density, power density and safety compared with LIBs. However, two critical bottlenecks remain in the development of SSBs towards commercialization: the development of SSEs with ionic conductivities rivaling those of conventional liquid electrolytes, and the stabilization of interfaces between SSB components, including the active material, SSE and conductive additives.

Over the past sixty years, extensive experimental efforts have been devoted to the search of solid materials with high ionic conductivities at room temperature, which have led to discoveries of numerous classes of superionic conductors (SICs) that were employed as SSEs in solid-state batteries. For interface stabilization, the use of coating has been demonstrated to be an effective strategy in mitigating parasitic interface reactions in SSBs. Despite these advances, the low throughput of experimental trial-and-error approaches has bottlenecked the speed of new materials discovery for SSB development. On the other hand, thanks to the recent advances in first-principles calculations, the ability to accurately compute material properties in silico combined with large material databases has provided a computational approach to high-throughput screening of materials with the target functionality, revolutionizing the material discovery process.

In this dissertation, I focus on leveraging first-principles techniques based on density functional theory (DFT) to search for new SSEs and coating materials for SSB applications. Chapter 1 introduces the concept of solid-state batteries and recent advances in the studies of SSEs and interface stability. Chapter 2 is devoted to a computational search for lithium oxide SICs for SSE development. In this chapter, I first revisited the ion-conduction mechanisms in lithium garnet and NASICON (sodium superionic conductor) structures, the two most used oxide SSEs, based on their Li diffusion networks. Three network features that are beneficial for superionic conduction were identified, i.e., a 3D ion diffusion network, short distances between occupied Li sites, and "homogenous local environments." Then, I performed a high-throughput screening to identify new

lithium oxide conductors with these beneficial features. At the end of this search, I proposed 7 candidates as promising lithium oxide SICs with room-temperature ionic conductivity of ~0.1 mS/cm or higher predicted by first-principles calculations. Furthermore, several new structural frameworks emerged, including spinel, oxy-argyrodite, sodalite, and $Li_xM(SeO_3)_2$, opening up exciting opportunities for lithium oxide SSE development.

Chapter 3 employs a computational framework to evaluate and screen materials for cathode coatings in SSBs, focusing on their phase stability, electrochemical and chemical stability, and ionic conductivity. From this tiered screening, polyanionic oxide coatings were identified to exhibit optimal properties, with LiH_2PO_4, $LiTi_2(PO_4)_3$, and $LiPO_3$ being particularly appealing candidates. Some lithium borates exhibiting excellent (electro)chemical stability at various interfaces were also highlighted. These results demonstrated the promise of using optimized polyanionic materials as cathode coatings for SSBs.

Finally, Chapter 4 summarizes the main findings of the dissertation and provides an outlook for the future directions of SSB development.

Table of Contents

Acknowledgments

Six years ago, UC Berkeley offered me an opportunity to explore the scientific research and higher education in the US as a PhD student. I took it, and the journey had since then been filled with amazement, inspiration, and struggles. I realized that my life had been fundamentally reshaped by the time and the people at Cal, to which I will always be grateful.

I thank my advisor, Prof. Gerbrand Ceder, for accepting me to his group and his guidance during my PhD. I appreciate the freedom he gave me in exploring my research directions and his patience and advice when I encountered obstacles. He is also a role model of leadership, professionalism, expertise, vision, high standards, and soft skills beyond academia. I also thank my former advisor, Prof. Ting Xu, for the opportunity to work in her lab as an experimentalist in the first two and a half years of my PhD. The experience of doing research from both theoretical and experimental sides has become a unique treasure to me.

My PhD life as a junior student would have been much harder without the tremendous help from my mentors, Peter Bai and William D. Richards. Peter is more than a great mentor but also a sincere friend. I am also grateful to Valentina Lacivita and Penghao Xiao for their generous help when I started learning the first-principles calculations. I also have many thanks to the solid-state battery team in the Ceder group for the inspiring discussions, close collaborations, and the joyful lunchtime after subgroup meetings.

Also, thank you to my buddies. Howard Tu and Tan Shi, I will miss the time playing pool together at Tap Haus after work. And Shuai Lou, with whom I first shared the same flight to the US and then the same bedroom wall for four years. Without them, my life at Berkeley would not have been so much fun.

I am grateful to my parents, Zhongjin Xiao and Weihua Wu, for their unconditional support in the past twenty-eight years. They have no idea of what I was working on during my PhD, but they constantly encouraged me to look on the bright side of life and comforted me as they always did.

Finally, to my girlfriend, Yanyan Huang, who had the extraordinary courage and faith to start a long-distance relationship across the Pacific Ocean and maintained it for five years. Although we were half a world away, she was always there during my hard times and when I made important decisions. I have no idea how many sacrifices she has made, but I do know how lucky I am to have her in my life.

Chapter 1: Introduction

Part of this chapter has been published in:

Xiao, Y., Wang, Y., Bo, S. H., Kim, J. C., Miara, L. J., & Ceder, G. (2020). Understanding interface stability in solid-state batteries. Nature Reviews Materials, 5, 105–126.

1.1 Solid-state batteries (SSBs)

Rechargeable Li-ion batteries (LIBs) have revolutionized the energy-storage market and enabled the widespread use of portable electronic devices and electric vehicles. However, commercial Li-ion batteries that use organic liquid electrolytes suffer from problems of flammability, low ion selectivity, limited electrochemical stability, and poor stability of the solid-electrolyte interphase (SEI) against Li metal.[1]

Solid-state batteries (SSBs) using solid-state electrolytes (SSEs) are considered to be one of the most promising candidates for the next-generation batteries. By replacing the liquid electrolyte in conventional LIBs with an SSE, SSBs hold the promise to offer improved energy densities and safety by reducing flammability, improving the cycle life and enabling the use of alkali-metal anodes. A schematic illustration of an SSB is shown in Figure 1.1. Unlike currently used organic liquid electrolytes, inorganic solid-state conductors are non-flammable or have much higher onset temperatures for thermal runaway. The reactivity of liquid electrolytes with electrodes also contributes substantially to the capacity fade of the battery.[2,3] Such electrolyte decomposition can, in principle, be mitigated by selecting an inorganic material that is thermodynamically stable or can passivate further reactions with electrodes. Indeed, minimal capacity fade over 10,000 cycles was observed in a solid-state cell employing a thin-film lithium phosphorus oxynitride (LiPON) electrolyte.[4] SSEs may also enable the use of lithium or sodium metal anodes, which have much higher volumetric and gravimetric capacities than graphite or hard carbon.[5,6] In liquid electrolytes, the formation of metal dendrites can short-circuit the cell.[7,8] By contrast, some SSEs have shown potential to suppress dendrite formation,[4,9,10] but the general effectiveness of ceramics in preventing dendrite growth between the electrodes remains in question.[11,12]

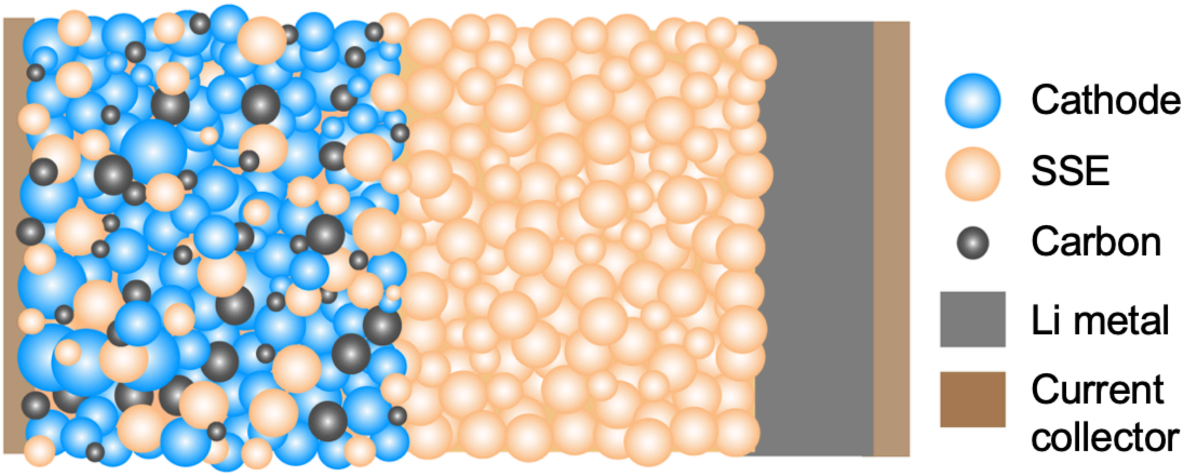

Figure 1.1 Schematic illustration of a solid-state battery.
Blue particle: active cathode material, orange particle: SSE, black particle: carbon, grey rectangle: Li metal, brown rectangle: current collector.

Nevertheless, there remain two critical bottlenecks in the development of SSBs towards commercialization: the development of SSEs with ionic conductivities rivaling those of conventional liquid electrolytes, and the stabilization of solid/solid interfaces between SSB components, including the active material, SSE and conductive additives. In the rest of Chapter 1, I provide an overview of recent investigations of inorganic solid-state electrolytes and interface (in)stability in SSBs.

1.2 Solid-state electrolytes in SSBs

One of the key properties of an SSE is its room-temperature ionic conductivity (σ_{rt}). The lack of solid superionic conductors (SICs) with room-temperature ionic conductivities comparable to those of liquid electrolytes has been a grand challenge in developing SSEs. For example, the room-temperature conductivities of $LiPF_6$ and $NaPF_6$ in the liquid solvent ethylene carbonate : dimethyl carbonate are 5–10 mS/cm.[13,14] Thanks to the extensive research efforts, several SSEs have been reported to exhibit room-temperature ionic conductivities in the range of 1–10 mS/cm or even higher, with an alkali-ion transference number close to 1 (compared with values often below 0.5 in liquid electrolytes).[13]

SSEs can be categorized by their anion chemistries, and the two most dominant categories are sulfides and oxides. Sulfides, especially thiophosphates based on the Li–P–S system, have emerged as leading SSE candidates because of their high ionic conductivities. In addition, their solution processability and ability to deform under cold pressing provide sulfides with an advantage for cell manufacturing compared with oxides. This category includes thio-LISICON (lithium superionic conductors)-type compounds $Li_{4-x}M_{1-x}P_xS_4$ (M=Ge, Si),[15,16] $Li_{10}GeP_2S_{12}$ (LGPS)[17] and its derivatives,[18,19] $Li_2S–P_2S_5$ glass[20] and $Li_7P_3S_{11}$ glass-ceramic,[21] and argyrodites Li_6PS_5X (X = Cl, Br, I).[22,23] To date, the highest room-temperature Li-ion conductivity reported in an SSE is 25 mS/cm in LGPS-type $Li_{9.54}Si_{1.74}P_{1.44}S_{11.7}Cl_{0.3}$.[18] High ionic conductivity has also been achieved in Na-ion sulfides such as Na_3PS_4,[24,25] Na_3SbS_4[26] and $Na_{10}SnP_2S_{12}$.[27,28]

Oxide-type SSEs include the cubic-garnet-structured $Li_xA_3B_2O_{12}$ (A=La, Nd, Mg, Ba, etc., B=Te, Ta, Nb, Zr, In, etc.),[29] NASICON (sodium superionic conductor)-structured $Li_{1+x}A_xB_{2-x}(PO_4)_3$ (A=Al, La, In, Cr, etc., B=Ti, Ge, Zr, Hf, Sn, etc.),[30] antiperovskites Li_3OX (X=Cl or Br),[31] perovskites $Li_{3x}La_{2/3-x}TiO_3$,[32] β-alumina,[33] and LISICONs with the γ-Li_3PO_4 framework (e.g., $Li_{2+2x}Zn_{1-x}GeO_4$).[34,35] However, the room-temperature bulk ionic conductivities of oxide SSEs are generally lower than those of sulfides, and their large grain-boundary resistance further restricts the total ionic conductivity.[36–40] Because of the mechanical rigidity of oxides, high-temperature sintering is usually required to produce a dense SSE pellet and to achieve intimate contact between the SSE and the electrode within the electrode composite.[29,39,41,42]

Another category of SSEs is based on borohydride anions such as BH_4^- and $B_nH_n^{2-}$ (n=10, 12).[43] For example, $Li_2B_{12}H_{12}$ and $Na_3(BH_4)(B_{12}H_{12})$ exhibit high room-temperature ionic conductivities on the order of 0.1 mS/cm.[44,45] In particular, the carbon-substituted borohydride $Na_2(CB_9H_{10})(CB_{11}H_{12})$ possesses an exceptional room-temperature ionic conductivity of approximately 70 mS/cm with an activation energy as low as 226 meV.[46] Recently, halide-type SSEs have received renewed interest since the discovery of two lithium halide ionic conductors Li_3YCl_6 and $LiYBr_6$ with room-temperature ionic conductivities approaching or surpassing 1 mS/cm.[47] Various other halide SICs with comparable ionic conductivities have also been reported, including Li_3ErCl_6,[48] $Li_2Sc_{2/3}Cl_4$,[49] $Li_{3-x}M_{1-x}Zr_xCl_6$ (M=Er, Y),[50] $Li_{3+x}ScCl_{3+x}$[51] and $Na_{3-x}Er_{1-x}Zr_xCl_6$.[52]

Despite the progress of SSE development, the experimental discovery of new SICs has been laborious and painstaking. For example, over the past 60 years, only six structural families of oxide SICs have been discovered:[53,54] β-alumina (1960s),[33] NASICONs (1970s),[55,56] LISICONs (1970s),[34] perovskites (1990s),[57] garnets (2000s),[58,59] and antiperovskites (2000s–2010s).[31,60] Since the discovery of the prototype compounds in each family, experimental and computational efforts have been made to explore the compositional space to optimize their ionic conductivity, stability, and processability.[18,19,29,32] However, exploring the more complex structural space to discover new frameworks for SICs remains a critical bottleneck.

Recently, computational studies of known SICs using first-principles methods based on density functional theory (DFT), such as DFT-based nudged elastic band (NEB) method and ab initio molecular dynamic (AIMD) simulation, have shed light on various mechanisms and structural features that can individually or synergistically lead to superionic conduction. These features and mechanisms include polarizable anions (e.g., S^{2-}),[61] a bcc anion framework,[62] the cooperative motion of Li ions,[63,64] a frustrated Li sublattice,[65] and enlarged Li sites.[66] These mechanistic understandings of ion conduction have guided the design of ionic conductors,[62,64,66] and have led to predictions of new SIC candidates having structural frameworks often dissimilar to those of known SICs.[66–68] Successful examples that have been validated by experiments include $Li_{1+2x}Zn_{1-x}PS_4$ ($\sigma_{rt} = 8 \times 10^{-4}$ S/cm),[69,70] predicted to be promising based on its bcc anion framework feature,[62,69] and $Li_{1+x}Ta_{1-x}Zr_xSiO_5$ ($\sigma_{rt} = 2.97 \times 10^{-5}$ S/cm),[71,72] predicted to be promising based on its enlarged Li site feature.[64,66] Therefore, the mechanism- and feature-guided computational search strategies for SICs allow for more efficient explorations of the structural space than the conventional trial-and-error approaches.

1.3 Interface stability in SSBs

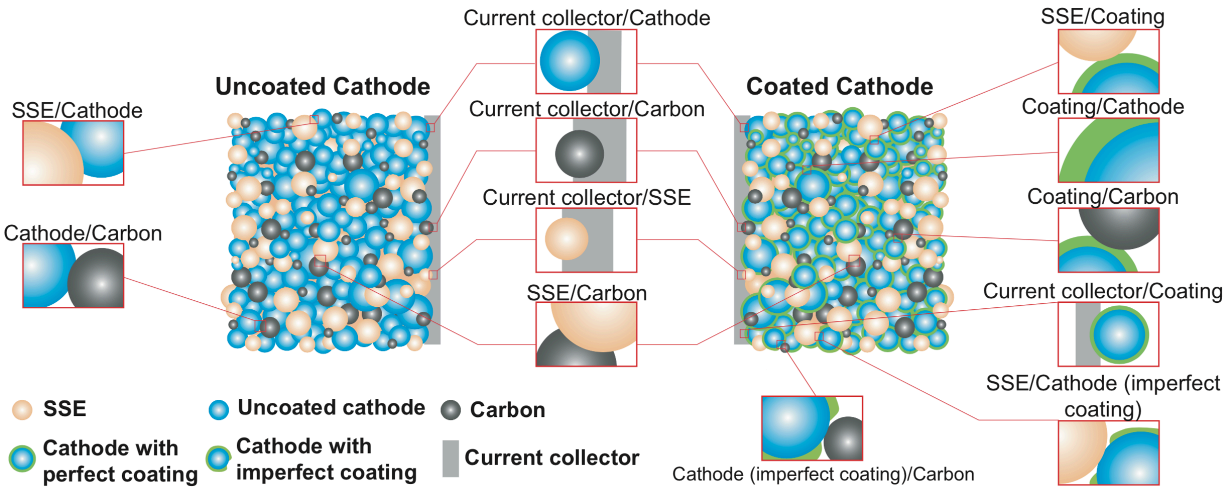

Figure 1.2 Interfaces in cathode composites of SSBs.
Schematic illustration of various interfaces in cathode composites of solid-state batteries with and without cathode coating.

Although high ionic conductivities have been achieved in various SSEs, the power density, rate capacity, and capacity retention of SSBs employing these SSEs remain poor, impeding their ultimate commercial usage.[61,73] These poor properties reflect the high resistance at various solid/solid interfaces in SSBs, which grows upon cycling. Each interface in an SSB can be categorized into one of three main classes according to its stability:[74,75] type I, thermodynamically stable interface with no driving force for reactions; type II, reacting to form a non-passivating interphase with both electronic and ionic conductivity, denoted as mixed ionic–electronic conducting interphase (MCI); and type III, reacting to form a stable SEI with negligible electronic conductivity, limiting further reaction. Long-term stable battery performance can only be expected for type I (stable) and type III (passivating) interfaces. For the latter, the ionic conductivity of the SEI is critical for battery performance.

The wide variety of interfaces present in cathode composites with coated and uncoated active cathode materials is schematically illustrated in Figure 1.2. Most studies focus on the cathode/SSE interface, because good ion transport across this interface must be maintained at all times. Thermodynamic stability at this interface is difficult to maintain because of the narrow electrochemical stability windows of many SSEs and their non-negligible chemical reactivity with the cathode. Specifically, because the active cathode material must also allow the transport of electrons, the SSE in contact with cathode particles is subjected to the alkali chemical potential set by the cathode voltage. When the SSE is not thermodynamically stable at such a high voltage, it tends to decompose into phases that often have reduced ionic conductivity. Additionally, the interdiffusion of elements and chemical reactions between the SSE and cathode can also generate phases that impede ion conduction across the interface.[76,77] One strategy used to satisfy the stringent stability requirement is to use an electronically insulating but ionically conducting electrode coating. The addition of such a coating layer creates two new interfaces: one between the coating and the electrode material and the other between the coating and the SSE. However, if coating-layer imperfections leave part of the electrode surface in contact with the SSE, as shown in Figure 1.2, unfavorable interfacial reactions still occur in the coated electrode system. Among the remaining interfaces in cathode composites, decomposition of the SSE can also occur at the current collector/SSE and carbon/SSE interfaces, where the SSE is subjected to the working lithium or sodium chemical potential.[78–80] Although neither ion nor electron transport across these interfaces is required for battery cycling, such decomposition unavoidably compromises the high bulk ionic conductivity of the SSE over time. On the alkali-metal-anode side, the instability of the SSE arises from its reduction by metallic lithium or sodium. If the SSE contains a metal or metalloid element(s), such reduction often leads to the generation of electron-conductive products at this interface, rendering it a detrimental MCI that continuously consumes the SSE.[74,75,81]

Next, we focus on the experimental and computational findings for interface stability related to sulfide SSEs and oxide SSEs. Although sulfide materials combine excellent mechanical processability and ionic conductivity, experimental investigations and DFT calculations indicate that their chemical stability and electrochemical stability are severely limited. First, the facile oxidation of S^{2-} results in poor electrochemical stability, which is limited to approximately 2–2.5 V in the cathode composite.[77,81,82] S^{2-} oxidation leads to condensation of PS_4 units with a general decrease in lithium content and, ultimately, even results in the formation of elemental sulfur.[78,83–85] Such oxidation decomposition is considered one of the main causes of the large first-cycle capacity loss in a high-voltage solid-state cell.[83] Although this degradation is mostly considered to occur at the cathode/SSE interface, it occurs even at non-functional interfaces such as the carbon/SSE and current collector/SSE interfaces.[78–80] Such degradation reduces the effective ionic conductivity in the cathode composite. Because the SSE decomposition products that form at high voltage are generally highly oxidized and alkali-deficient, they may retard further decomposition. Second, when oxide cathodes are in contact with sulfide SSEs, there is a further driving force for degradation via the exchange of S^{2-} and O^{2-}, leading to the formation of PO_4^{3-} polyanions and transition-metal sulfides,[77,81,86–89] which causes impedance growth and capacity loss. Against the Li-metal anode, reduction of all but just a few metal or metalloid ions in sulfides occurs, creating electronically conducting products that form an MCI.[77,81,82] This phenomenon is a particular problem for some highly conducting sulfides that contain Ge, Si, Sn and Sb.[74,81,90–94] The addition of halogens to sulfide SSEs, such as I and Cl, may contribute to the formation of a passivating SEI containing Li halides that prevents further reduction.[9,92,95,96]

Compared with sulfide SSEs, oxide-type SSEs generally exhibit higher oxidation stability and improved chemical stability with oxide cathodes.[77,81,82] However, the high processing temperature can degrade electrode materials such as $LiNi_xCo_yMn_{1-x-y}O_2$[97] and $LiCoO_2$,[98] and promote the chemical reactivity at the SSE/electrode interface.[99,100] Among oxide SSEs, the most frequently used lithium garnet $Li_7La_3Zr_2O_{12}$ (LLZO) has often been claimed to be stable with Li metal and to voltages above 5 V,[101–103] but the collective computational and experimental data suggest that the oxidation occurs at a lower voltage between 3–4 V.[81,82,104,105] The observed oxidation decomposition at a low voltage indicates that LLZO cannot be paired with a high-voltage cathode such as $LiNi_{0.5}Mn_{1.5}O_4$ (~4.7 V).[106,107] Chemical mixing of garnets with oxide cathodes is much less severe than that of sulfide SSEs;[81] however, the high-temperature co-sintering of the garnet SSE and the cathode material required for processing not only destabilizes the garnet SSE by Li loss but also promotes elemental interdiffusion and transition-metal reduction. For example, the high-temperature reaction product La_2CoO_4 at the $LiCoO_2$/garnet interface contains a reduced transition-metal cation Co^{2+} from the cathode and La^{3+} from the garnet SSE.[108] Therefore, techniques such as low-temperature and short-time sintering and interfacial modification such as coating are desirable for garnet SSEs. On the anode side, whereas the Zr-containing garnet only has a minor thermodynamic driving force (20 meV/atom) predicted by DFT to react with Li metal,[77] the Nb-containing garnet can clearly be reduced by Li metal, as evidenced by both DFT calculations and experimental data.[109–111] Strongly reducible dopants such as Fe^{3+} further deteriorate the reduction stability of garnets.[112] The Zr- and Ta- containing garnets have high barriers for topotactic Li insertion,[109] which likely kinetically stabilize these systems against a Li-metal anode. However, if Li insertion occurs in cubic garnets, a tetragonal phase (stabilized by the higher Li content) forms and increases the interfacial impedance.[113] In principle, the slight reduction of Zr^{4+} in LLZO by Li metal would also increase the electronic conductivity of the interphase and slowly propagate into the bulk electrolyte.

Given the interface instability involving various classes of SSEs, engineering stable interfaces in SSBs is critical to further improving the cell performance. As shown in Figure 1.2, a coating layer is often applied to prevent the direct contact between the active material and the electrolyte.[114,115] In principle, either the electrode or the electrolyte could be coated to stabilize the electrode/electrolyte interface. A buffer layer has been used in the protected lithium electrode in Li-air batteries to prevent the reduction of Ti^{4+} in NASICON-type solid-state electrolytes by metallic lithium.[116] On the cathode side, coating the electrode is usually preferred because coating the SSE would significantly increase the resistance along ion migration pathways. Several cathode coating materials have improved the performance of SSBs, including Li_3PO_4,[117] $LiAlO_2/Al_2O_3$,[118] $LiTaO_3$,[119]

$LiNbO_3$,[73,120,121] $Li_4Ti_5O_{12}$,[115,122] Li_2SiO_3,[76] Li_3BO_3,[123] and Li_2ZrO_3.[124] However, the composition of cathode coating materials remains to be optimized.

1.4 Motivation and outline

Despite these exciting advances in SSBs, the discovery and optimization of new SSEs combining high ionic conductivity and good (electro)chemical stability, as well as new coating materials that stabilize the electrode/SSE interface, are still of critical importance. In the previous sections, it has been demonstrated that first-principles-based computational methods have greatly deepened our understanding of interfacial (in)stability in SSBs and ion-conduction mechanisms in SSEs. The latter has in turn facilitated the discovery of several new solid superionic conductors. In this dissertation, I focus on leveraging these computational tools to search for the next-generation SSEs and cathode coating materials for SSBs, aiming to tackle the two critical bottlenecks in the SSB development as discussed in section 1.1. The remainder of the dissertation is organized into the following chapters:

Chapter 2 is devoted to a computational search for lithium oxide SICs as the next-generation SSEs. First, I revisited the ion-conduction mechanisms in lithium garnet and NASICON structures and identified three beneficial features of their Li diffusion networks for achieving superionic conduction. Then, a high-throughput computational screening was performed to identify new lithium oxide conductors having these features. As a result of the screening, seven promising lithium oxides were found to exhibit high room-temperature ionic conductivity of approximately 0.1 mS/cm or higher predicted by AIMD simulations.

Chapter 3 presents a computational framework to evaluate and screen materials for cathode coatings in SSBs, focusing on their phase stability, electrochemical and chemical stability, and ionic conductivity. From this tiered screening, polyanionic oxide coatings were identified as exhibiting optimal properties, with LiH_2PO_4, $LiTi_2(PO_4)_3$, and $LiPO_3$ being particularly appealing candidates. Some lithium borates exhibiting excellent (electro)chemical stability at various interfaces were also highlighted.

Chapter 4 summarizes the main findings of the dissertation and provides an outlook for the future directions of SSB development.

Chapter 2: Computational screening of Li oxide superionic conductors for solid-state batteries

2.1 Introduction

Solid-state electrolytes composed of SICs with high ionic conductivities are the key component of SSBs.[125,126] Among various classes of SSEs, oxide-type SSEs have the advantages of a relatively wide electrochemical stability window,[77,81,82,127] good chemical stability with oxide electrodes,[77,81,82,127] and good thermal stability.[128] However, to date, their applications in high-energy-density lithium SSBs have been largely limited to two structural families: cubic lithium garnets[29] and NASICONs.[30] Other oxide SSEs such as LiPON,[10] antiperovskites,[31] perovskites,[32] and LISICONs[34,35] have been used less frequently because of their relatively low ionic conductivities[126] or poor electrochemical stability against a Li metal anode.[127] In contrast, sulfide SSEs with various structure types have been developed and widely applied in lithium SSBs, including Li_2S–P_2S_5 glass,[20] $Li_7P_3S_{11}$ glass-ceramics,[21] $Li_{10}GeP_2S_{12}$[17] and its derivatives,[18,19], argyrodites,[22,23,129] β-Li_3PS_4,[130,131], and $Li_{1+2x}Zn_{1-x}PS_4$.[69,70,132] Moreover, the ionic conductivities of current oxide SSEs are generally at least one order of magnitude lower than those of sulfide SSEs.[126] Therefore, it is important to discover new lithium oxide SICs with novel structural frameworks (i.e., a crystal structure excluding mobile ions) and high room-temperature ionic conductivities for future development of oxide-SSE-based SSBs.

In this chapter, we performed a computational screening for new lithium oxide SICs with novel structural frameworks. We started by revisiting the ion-conduction mechanisms in lithium garnet and NASICON, the two most often used oxide SICs for SSB applications. Two crucial factors for achieving superionic conduction in both SICs were identified, i.e., a 3D percolation Li diffusion network and a moving "activated local environment." We then translated these factors into three structural features and performed a high-throughput screening to identify compounds with these features. Next, we stuffed excess Li ions into the screened structures and evaluated their ionic conductivities using AIMD simulations. Finally, we proposed 7 promising lithium oxide SIC candidates with high room-temperature ionic conductivity (~0.1 mS/cm or higher) and reasonable synthesizability. Their structural frameworks such as spinel, oxy-argyrodite, sodalite, and $LiM(SeO_3)_2$ open up new opportunities for enriching the structural families of lithium oxide SICs.

2.2 Results

2.2.1 Li diffusion networks in garnet and NASICON structures

To achieve high ionic conductivity in a material, Li ions need to migrate between Li sites with a low activation energy. Here, we define the Li diffusion network as a graph of face-sharing Li sites in the crystal structure of a material. A Li site is defined as the center of a polyhedron formed by O^{2-} anion corners and is represented by a node in the network, and "face" is defined as an O^{2-} triangular facet of a polyhedron. The face-sharing relation between two Li sites is represented by an edge between corresponding nodes in the network. Thus, the Li diffusion network can be viewed as a road map for Li-ion transport in the material. For example, Figure 2.1A and 2.1D show the crystal structures of Li3 garnet ($Li_3La_3Te_2O_{12}$) and pristine NASICON ($LiTi_2(PO_4)_3$), respectively. Simplified 2D representations of their Li diffusion networks are presented in Figure 2.1B and 2.1E, respectively. For clarity, Li sites not participating in the ion conduction are not displayed in the network.

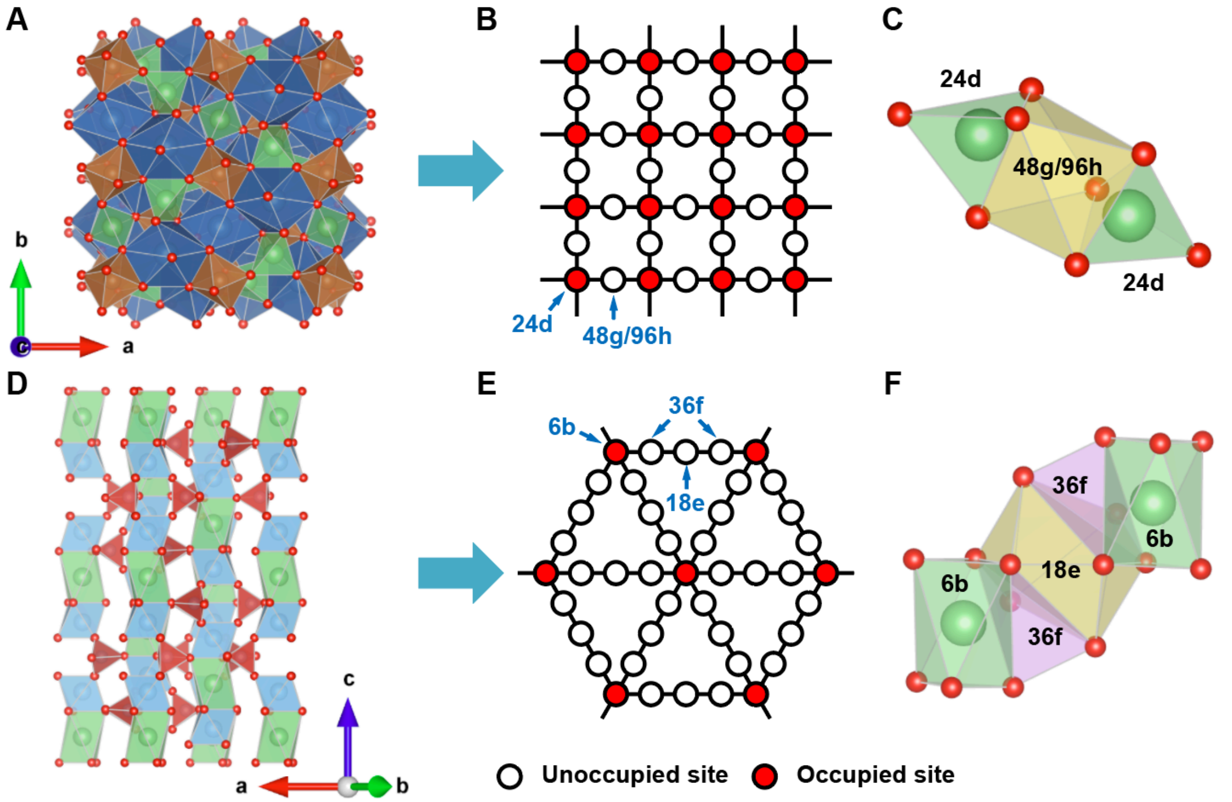

Figure 2.1 Crystal structures, 2D representations of Li diffusion networks, and local environments of Li3 garnet and pristine NASICON.

(A–C) Crystal structure of Li3 garnet with the composition $Li_3La_3Te_2O_{12}$ (A) and simplified 2D representation of its Li diffusion network (B). The site arrangement in the local environment between neighboring 24d sites is shown in (C). Green tetrahedrons: Li 24d sites, yellow octahedrons: Li 48g/96h sites, brown octahedrons: TeO_6, blue polyhedrons: LaO_8.

(D–F) Crystal structure of NASICON with the composition $LiTi_2(PO_4)_3$ (D) and simplified 2D representation of its Li diffusion network (E). The site arrangement in the local environment between neighboring 6b sites is shown in (F). Green octahedrons: Li 6b sites, yellow polyhedrons: Li 18e sites, purple tetrahedrons: Li 36f sites, red tetrahedrons: PO_4, blue octahedrons: TiO_6. Green spheres: Li ions, red spheres: O^{2-} anions. Each circle in the Li diffusion network represents a Li site. An edge between two circles exists if their corresponding sites are face-sharing with each other. Empty circles: unoccupied Li sites, solid red circles: occupied Li sites.

Garnets are known to have a framework that is beneficial for Li-ion conduction.[63,133–136] The Li diffusion network of garnets is 3D, and every two neighboring tetrahedral (tet) 24d sites are bridged by an intermediate octahedral (oct) 48g/96h site (Figure 2.1B).[29,137] As a result, each percolation path in the garnet framework has the –tet–oct–tet–oct– site configuration. In a Li3 garnet such as $Li_3La_3Te_2O_{12}$, only the tetrahedral 24d sites are fully occupied by Li ions, whereas the octahedral 48g/96h sites are vacant (Figure 2.1B).[135] Notably, all local environments between two neighboring 24d sites are symmetrically equivalent, which we describe as "homogenous local environments" of the Li3 garnet network. The specific site arrangement of this local environment is shown in Figure 2.1C.

The Li diffusion network of NASICONs is topologically similar to that of the Li3 garnet in three ways: 1) the network is also 3D;[138] 2) only the crossing nodes (octahedral 6b sites) in the network are occupied for the pristine composition (Figure 2.1E),[138] and 3) the network also has homogenous local environments, as shown in Figure 2.1E and 2.1F. These shared topological similarities between garnet and NASICON networks suggest a common pattern in their ion-conduction mechanisms, which will be discussed in the next section. However, one significant difference between the two networks is that the distance between occupied crossing nodes is much larger in the pristine NASICON (6.02 Å) than that in the Li3 garnet (3.94 Å). The difference exists because there are three intermediate bridging nodes (36f, 18e, 36f) between crossing nodes in the NASICON (Figure 2.1F),[138] whereas in the Li3 garnet, there is only one (Figure 2.1C).

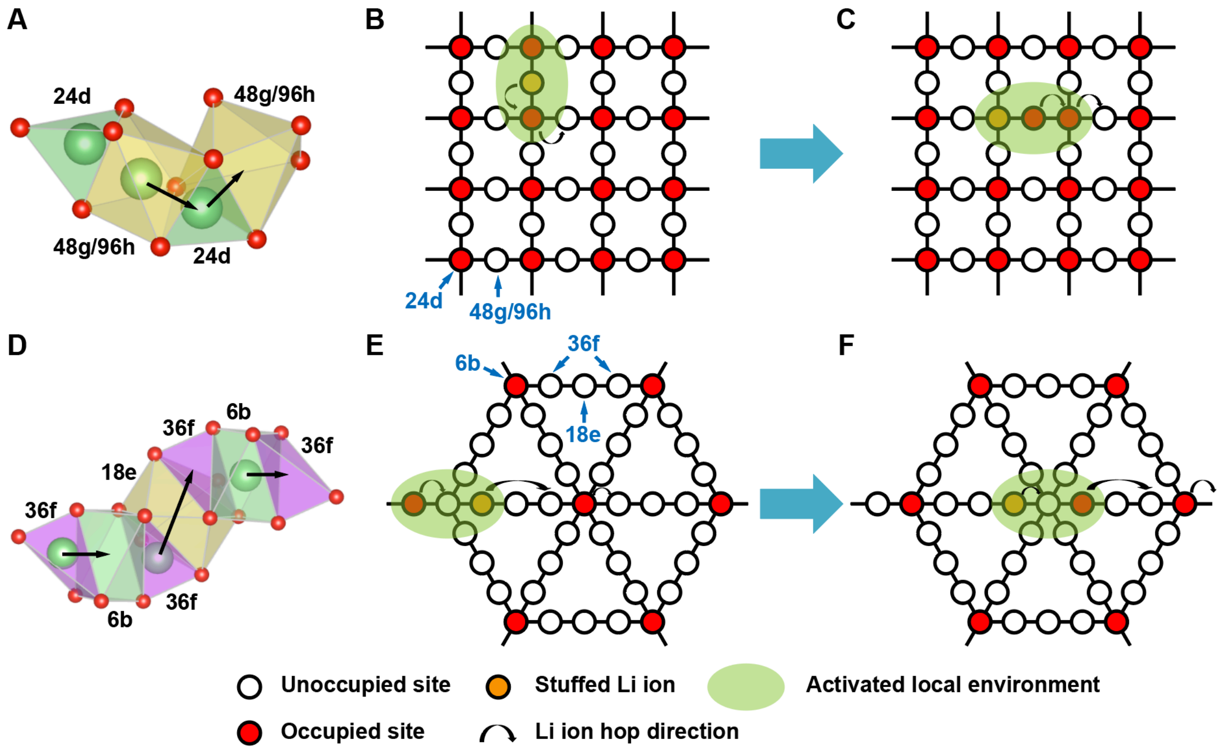

Figure 2.2 Li-ion conduction in Li-stuffed Li3 garnet and NASICON via cooperative hopping of Li ions in "activated local environment."

(A–C) Cooperative hopping of two Li ions in 24d and 48g/96h sites in the Li-stuffed garnet framework illustrated in the local environment (A) and in the simplified 2D Li diffusion network (B). The Li diffusion network after one step of cooperative hopping is shown in (C). Green tetrahedrons: Li 24d sites, yellow octahedrons: Li 48g/96h sites.

(D–F) Cooperative hopping of three Li ions in 36f, 36f, and 6b sites in the Li-stuffed NASICON framework illustrated in the local environment (D) and in the simplified 2D Li diffusion network (E). The Li diffusion network after one step of cooperative hopping is shown in (F). Green octahedrons: Li 6b sites, yellow polyhedrons: Li 18e sites, purple tetrahedrons: Li 36f sites.

Empty circles: unoccupied Li sites, solid red circles: occupied Li sites, solid orange circles: sites occupied by the stuffed Li ions. Green ellipses: activated local environments, arrows: the next hopping directions of Li ions.

2.2.2 Ion-conduction mechanisms in garnet and NASICON frameworks

The ion-conduction mechanisms in garnet and NASICON frameworks have been extensively studied both computationally and experimentally.[63,64,135,138,139] The Li diffusion network helps us to illustrate these mechanisms,[63,135] as shown in Figure 2.2, based on which we can identify network features that are beneficial for achieving high ionic conductivity.

The lithium garnet $Li_xA_3B_2O_{12}$ (denoted as "Lix garnet") has a robust framework that can accommodate a wide range of Li concentrations (x = 3–7, or Li3–Li7).[29,133] Experimentally, even a slight increase of x from 3 to 3.1 leads to a steep increase of ionic conductivity of 3 orders of magnitude at 400 °C.[140] As x further increases toward 7, the room-temperature conductivity approaches the order of 10^{-4} S/cm,[29,102] with a peak value of approximately 10^{-3} S/cm achieved at x = 6.4[29,141] or 6.7.[142] Previous computational studies have mostly focused on the ion-conduction mechanism of garnets with x near 7.[63,64,135] At such a high Li concentration, AIMD simulation results have suggested that the low activation energy of approximately 300 meV can be attributed to the cooperative motion of Li ions in the face-sharing tetrahedral 24d sites and octahedral 48g/96h sites resulting from the strong coulombic interaction between them.[63,64]

In contrast, the ionic conduction mechanism of garnets at x = 3+δ have been computationally less explored, despite the "switching-on" of the fast ionic conduction behavior at this composition.[29,139,140] In a pristine Li3 garnet, Li-ion migration involves moving a tetrahedral Li ion to a neighboring octahedral site with a barrier larger than 1 eV,[65,135,140] explaining its negligible conductivity at room temperature. As a dilute amount of Li ions is stuffed into the Li3 garnet to reach x = 3+1/8, DFT computation shows that the stuffed Li ion resides in the octahedral 48g/96h site, creating a local tet–oct–tet Li-ion arrangement, as shown in Figure 2.2A and the green shaded area in Figure 2.2B. The short Li^+–Li^+ distance of 2.27 Å between the face-sharing tetrahedral and octahedral Li ions induces strong coulombic repulsion similar to that in the Li7 case,[63,64] suggesting that cooperative motion may also occur in the Li3+δ garnets. Specifically, the stuffed octahedral Li ion moves to a face-sharing tetrahedral site and pushes the Li ion originally at that site to another octahedral site, as illustrated in Figure 2.2A and 2.2B. Indeed, an activation energy of only 160 meV was calculated using the NEB method for this mechanism (Figure 2.S1); this low NEB barrier is further supported by a similar activation energy of 198 ± 84 meV determined from AIMD simulation (Figure 2.S2).

From the viewpoint of the Li diffusion network, the conduction mechanism of the NASICON-structured $Li_{1+x}Al_xTi_{2-x}(PO_4)_3$ is similar to that of Li3+δ garnet,[138] which can be attributed to the similarities in their network topology. Indeed, upon Li stuffing, the measured bulk ionic conductivity of the NASICON was enhanced by a factor of 3–30[143,36,144,145] with a reduction of the activation energy by 70–160 meV.[144,146] As a Li ion is stuffed into the pristine NASICON structure, both experimental and DFT results have indicated that the stuffed Li ion would reside in the tetrahedral 36f site and displace the face-sharing octahedral 6b Li ion to the opposite tetrahedral 36f site, leaving a distance of 3.25 Å between them (Figure 2.2D).[138,147,148] As reported by Lang et al.[138], the interstitial ion conduction involves a cooperative hopping of three nearby Li ions at the 36f, 36f, and 6b sites, as illustrated in Figure 2.2D and 2.2E. Specifically, in the NASICON network in Figure 2.2E, two Li ions in 36f sites in the green shaded area hop right to the octahedral 6b and tetrahedral 36f sites. In the meantime, the octahedral 6b Li ion originally in the center of the network is pushed to the tetrahedral 36f site on the right.[138] The low NEB barrier of 190 meV for this mechanism calculated by Lang et al.[138] is supported by our AIMD result of a very similar activation energy of 186 ± 47 meV (Figure 2.S3).

Notably, at the end of both cooperative motions in the garnet and NASICON networks, a new local environment containing an interstitial Li ion is created, as indicated by the green shaded areas in Figure 2.2C and 2.2F. Because both pristine networks have homogeneous local environments, the green shaded local environments in Figure 2.2C and 2.2F are also symmetrically equivalent to those in Figure 2.2B and 2.2E, respectively. The equivalence means that this green shaded local environment can continue to propagate in the network via the exact same cooperative hoppings we described, which eventually leads to percolation.

2.2.3 Screening strategies of lithium oxide SICs

There is a common pattern in the ion-conduction mechanisms of both the Li-stuffed garnet and NASICON frameworks, which we denote as the "activated diffusion network." In this pattern, all the local environments in the pristine network are quiescent for ionic conduction. Stuffing an excess Li ion into the pristine network creates a type of local environment where the migration barrier of Li ions is much lower via cooperative motion. We denote this type of local environment as the "activated local environment," or "activation" for short. The activated local environment can then propagate in the diffusion network, leading to percolation, as demonstrated in Figure 2.2. This pattern can also be applied to other Li-ion conductors with a cooperative motion or "kick-out" mechanism such as $Li_{1+2x}Zn_{1-x}PS_4$[132] or Li_3PO_4.[149] The pattern also suggests a physical picture where only the activated local environments contribute to the ionic conduction while the rest of the network remains quiescent, a mechanism that has also been suggested for ionic migration in glass systems.[150–152]

There are two essential steps required by this pattern: Step 1: initiation of the activation, meaning that the stuffed Li ion is able to create the first activated local environment in the network. Step 2: propagation of the activation, meaning that the activation is able to keep propagating in the network without dying out (i.e., the interstitial Li ion will not be trapped in a local environment where there is an energy basin) and will eventually percolate throughout the network.

It is important to consider why such a pattern works in garnet and NASICON frameworks. Thus, we examined their network features to determine how they are beneficial to the two steps mentioned above. First, both the garnet and NASICON frameworks have a 3D percolation network. The 3D diffusion channels allow the activation to propagate in the network in all three dimensions, and the crossing between these channels makes them unlikely to be blocked by point defects compared with the 1D case.[153] Therefore, the 3D feature is beneficial for the propagation of activation (step 2). Second, the pristine networks of both Li3 garnet and NASICON have homogenous local environments. This feature guarantees that once an activation is initiated in the network, it will not die out during the propagation, as any local environment to which the interstitial Li ion moves will be equivalent to the first activated local environment, as observed in Figure 2.2C and 2.2F. This feature is thus also beneficial for the propagation of activation (step 2). Third, the distances between all neighboring occupied Li sites are short in Li3 garnet. This feature is only present in the network of the Li3 garnet but not in that of the NASICON. Specifically, the cartesian distance between two neighboring occupied tetrahedral 24d sites is only 3.94 Å in Li3 garnet. After Li stuffing, the stuffed Li ion is inserted into the middle of two 24d Li ions, cutting the local Li^+–Li^+

distance by half to 1.97 Å before the structural relaxation and to 2.27 Å after the relaxation. Such a short Li^+–Li^+ distance can result in a strong coulombic interaction in the local environment and likely lead to a lowered Li hopping barrier,[64] that is, the initiation of activation (step 1). The same effect also applies to the propagation process, as any local environment to which the interstitial Li ion moves will also likely be activated owing to the short distance between occupied Li sites there. This feature is thus beneficial for both steps 1 and 2.

In comparison, the distance between occupied 6b sites in the NASICON network is much larger (6.02 Å). After Li stuffing, the shortest Li^+–Li^+ distance becomes 3.25 Å after relaxation, which is 1-Å larger than that in the Li-stuffed Li3 garnet (2.27 Å), corresponding to a much weaker coulombic force between nearest Li ions (49% according to Coulomb's law). Therefore, the initiation of the activation in the Li-stuffed NASICON network may not simply be caused by the local coulombic interactions and should also be attributed to the relatively flat energy landscape of the NASICON structure. Indeed, AIMD results reveal that Li ions in the Li3 garnet are much more localized in its equilibrium 24d sites than in the pristine NASICON, as indicated by their mean square displacements (Figure 2.S4). As a result, we ended up with two beneficial network features for the NASICON network: a 3D network and homogeneous local environments. For the Li3 garnet network, there is an additional feature: the short distances between occupied Li sites.

Inspired by the common ion-conduction pattern and network features in garnets and NASICONs, it was desirable to design new lithium SICs with the same ion-conduction pattern enabled by these features. To that end, we developed two strategies for identifying new garnet-like and NASICON-like Li oxide SICs using two different combinations of features.

Potential garnet-like SICs include compounds with 1) a 3D percolating lithium diffusion network and 2) a short distance of ≤ 4 Å between all neighboring occupied Li sites in the pristine network. The value of 4 Å is referenced to that in Li3 garnet (3.94 Å), such that after Li stuffing, the shortest Li^+–Li^+ distance will be halved to below 2 Å, creating a similar or even stronger local coulombic interaction than that in the Li-stuffed Li3 garnet. This combination of features will benefit both the initiation (step 1) and propagation (step 2) of the activation. Therefore, the "homogeneous local environments" feature is not a necessity, although it is also present in the Li3 garnet network.

Potential NASICON-like SICs include compounds with 1) a 3D percolating lithium diffusion network and 2) homogeneous local environments in the pristine network. This combination of features will only benefit the propagation of the activation (step 2). Whether this activation can be initiated upon Li stuffing (step 1) still depends on the specific framework.

For candidates identified using either strategy, a Li ion was stuffed into its supercell to initiate the first activation in the network. Before implementing a search using these two strategies, algorithms were needed to extract and quantify these network features for a given crystal structure, i.e., the lithium diffusion network and its dimensionality, the distances between occupied Li sites, and a metric identifying homogenous local environments of the network. In the next section, we describe how these features were defined and computed.

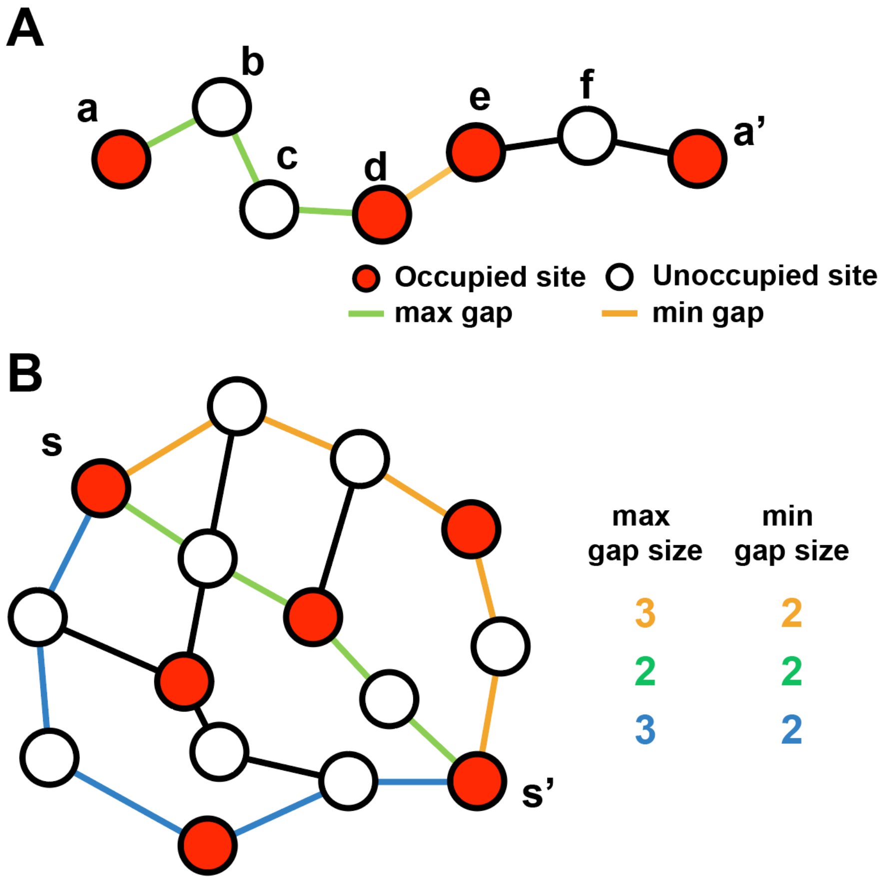

Figure 2.3 Schematics of percolation paths and the definition of “gap.”
(A) An example percolation path from a Li site **a** to its periodic image **a’** through face-sharing Li sites (circles). Each edge has a length of 1. The max gap consists of green edges between sites **a** and **d** with a gap size of 3. The min gap consists of the orange edge between sites **d** and **e** with a gap size of 1.
(B) An example Li diffusion network between a Li site **s** and its periodic image **s’**. Three example percolation paths from **s** to **s’** are colored in orange, green, and blue. Each edge has a length of 1. The max and min gap size for each percolation path are summarized in the inset table. The green path with the smallest max gap size is selected as the “representative percolation path” in the network.

2.2.4 Quantification of network features

Li diffusion network and percolation dimensionality. We performed Delaunay tetrahedralization[154,155] on the crystal framework to find all potential Li sites, which were represented as individual nodes in the Li diffusion network graph. Nodes that correspond to partially or fully occupied Li sites were denoted as “occupied nodes,” and the rest were denoted as “unoccupied nodes.” Edges were drawn between two nodes if their corresponding sites were face-sharing with each other. The dimensionality of the network was defined as the number of dimensions in which at least one occupied node that could percolate to its next periodic image exists. More details on the construction of the Li diffusion network and percolation analysis are provided in Supplementary Note in section 2.6.

Gap and gap size. We defined the "gap" as the pathway between two neighboring occupied Li sites connected by a series of face-sharing unoccupied Li sites. Therefore, the gap is a suitable representation of the local environment in the network. In the example percolation path in Figure 2.3A, there are three gaps 1) **a**–**b**–**c**–**d**, 2) **d**-**e**, and 3) **e**–**f**–**a'**. In this work, we used "gap size," which is the total length of the gap, to represent the distance between occupied Li sites. Assuming all the edges have a length of 1 in Figure 2.3A, the three gap sizes are 3, 1, and 2, respectively. The advantage of using gap size instead of cartesian distance will be explained later.

Maximum and minimum gap size. Each percolation path in the diffusion network is composed of multiple gaps, such as those in Figure 2.3A. Two key quantities are recorded: the maximum (max) and minimum (min) gap size. For example, for the percolation path in Figure 2.3A, the max gap size is 3 and the min gap size is 1. To find garnet-like SICs, we replaced the second requirement on the site distances with the new requirement of "max gap size of the **pristine network** ≤ 4 Å". It is easy to demonstrate the following property: for a pristine network meeting this requirement, the min gap size of the **Li-stuffed network** will be equal to or less than 2 Å (neglecting relaxation). Such a small min gap size upon Li stuffing suggests a strong coulombic interaction in the local environment, likely initiating the activation as in the Li3 garnet. We note that this convenient property of the gap size would not hold for cartesian distance because the stuffed Li ion may not be positioned precisely on the line segment between two occupied Li sites.

Homogenous local environments. In a strict sense, the condition "homogenous local environments" requires all gaps in the network to be symmetrically equivalent. In this work, we used a weaker condition of "the max gap size is equal to the min gap size in the pristine network". This weaker condition guarantees that all gaps in the network have the same size, which is a strong indication of the strict equivalence of all gaps. Using the max gap size in the pristine NASICON network (6.73 Å) as a reference, we focus on compounds with a max gap size ≤ 7 Å in this work.

Representative percolation path. Several percolation paths often exist in a Li diffusion network, some of which consist of high-energy sites that are not involved in Li-ion conduction. In this work, only the percolation path with the smallest max gap size was selected as the "representative percolation path" for the gap size analysis. For example, for the three percolation paths in Figure 2.3B between a node **s** and its periodic image node **s'**, the green path will be selected. With this assumption, the actual ion conduction paths for garnet and NASICON structures can be found in their networks. More details on the path selection are provided in Supplementary Note in section 2.6.

With the network features defined as computable quantities, we then formally translated the two strategies for finding garnet-like and NASICON-like SICs into two regimes. The requirements for the garnet regime were 1) percolation dimensionality = 3 and 2) max gap size ≤ 4 Å for the pristine Li diffusion network. The requirements for the NASICON regime were 1) percolation dimensionality = 3 and 2) 4 Å < min gap size = max gap size ≤ 7 Å for the pristine Li diffusion network. Note that we did not consider min gap size ≤ 4 Å in the NASICON regime as this would overlap with the garnet regime. We then performed a high-throughput screening of structures from the Inorganic Crystal Structure Database (ICSD)[156] to identify new lithium oxide SICs.

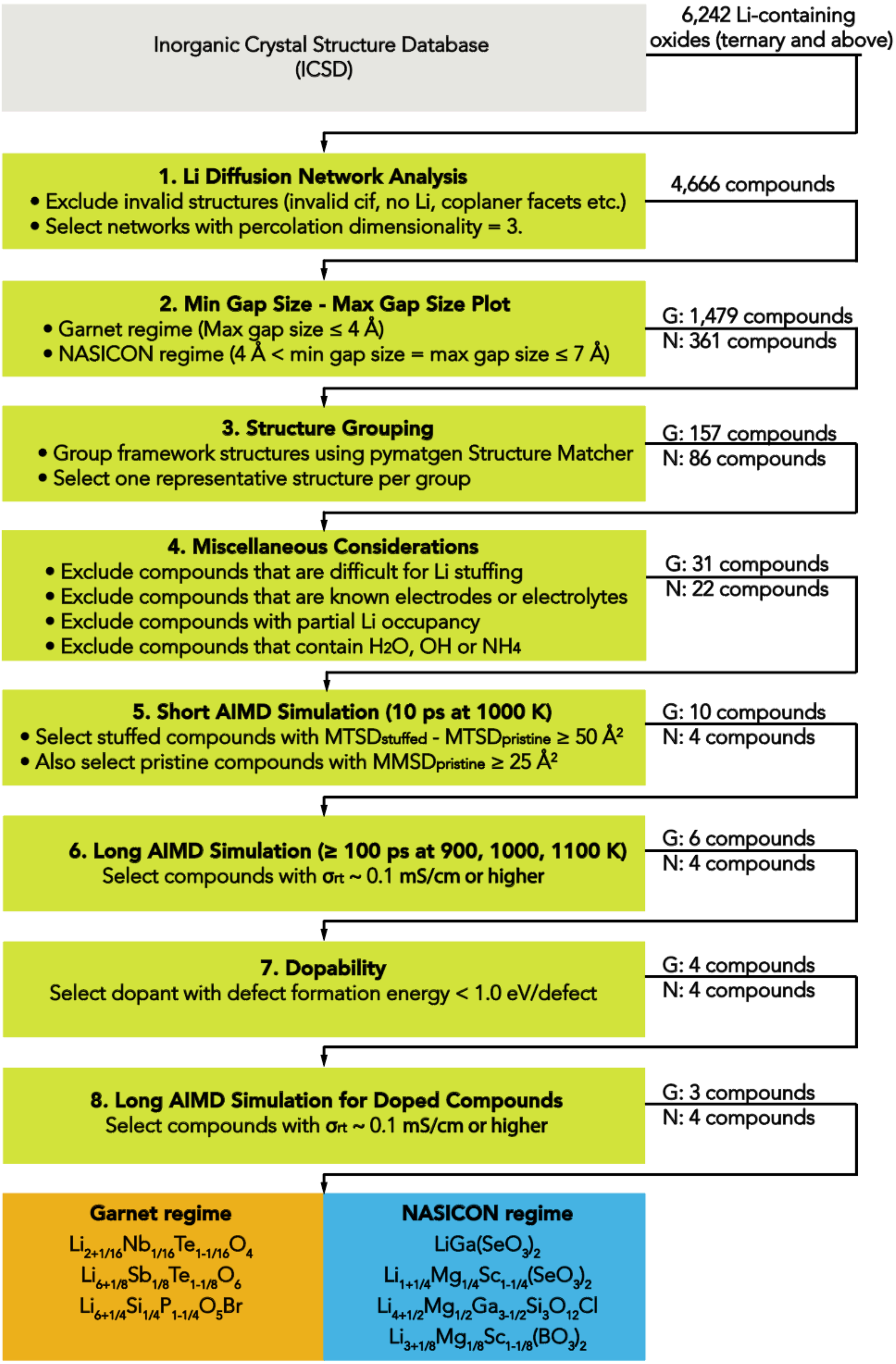
Inorganic Crystal Structure Database (ICSD)
6,242 Li-containing oxides (ternary and above)
1. Li Diffusion Network Analysis
• Exclude invalid structures (invalid cif, no Li, coplaner facets etc.)
• Select networks with percolation dimensionality = 3.
4,666 compounds
2. Min Gap Size - Max Gap Size Plot
• Garnet regime (Max gap size ≤ 4 Å)
• NASICON regime (4 Å < min gap size = max gap size ≤ 7 Å)
G: 1,479 compounds
N: 361 compounds
3. Structure Grouping
• Group framework structures using pymatgen Structure Matcher
• Select one representative structure per group
G: 157 compounds
N: 86 compounds
4. Miscellaneous Considerations
• Exclude compounds that are difficult for Li stuffing
• Exclude compounds that are known electrodes or electrolytes
• Exclude compounds with partial Li occupancy
• Exclude compounds that contain H_2O, OH or NH_4
G: 31 compounds
N: 22 compounds
5. Short AIMD Simulation (10 ps at 1000 K)
• Select stuffed compounds with $MTSD_{stuffed}$ - $MTSD_{pristine}$ ≥ 50 Å²
• Also select pristine compounds with $MMSD_{pristine}$ ≥ 25 Å²
G: 10 compounds
N: 4 compounds
6. Long AIMD Simulation (≥ 100 ps at 900, 1000, 1100 K)
Select compounds with σ_{rt} ~ 0.1 mS/cm or higher
G: 6 compounds
N: 4 compounds
7. Dopability
Select dopant with defect formation energy < 1.0 eV/defect
G: 4 compounds
N: 4 compounds
8. Long AIMD Simulation for Doped Compounds
Select compounds with σ_{rt} ~ 0.1 mS/cm or higher
G: 3 compounds
N: 4 compounds
Garnet regime
$Li_{2+1/16}Nb_{1/16}Te_{1-1/16}O_4$
$Li_{6+1/8}Sb_{1/8}Te_{1-1/8}O_6$
$Li_{6+1/4}Si_{1/4}P_{1-1/4}O_5Br$
NASICON regime
$LiGa(SeO_3)_2$
$Li_{1+1/4}Mg_{1/4}Sc_{1-1/4}(SeO_3)_2$
$Li_{4+1/2}Mg_{1/2}Ga_{3-1/2}Si_3O_{12}Cl$
$Li_{3+1/8}Mg_{1/8}Sc_{1-1/8}(BO_3)_2$

Figure 2.4 Flowchart describing the computational screening procedures for lithium oxide SICs.

MTSD is the maximum total square displacement, MMSD is the maximum mean square displacement, and σ_{rt} is the extrapolated room-temperature conductivity from AIMD simulations. G and N represent the garnet and NASICON regimes, respectively.

2.2.5 High-throughput screening

The screening procedures for lithium oxide SICs are described in Figure 2.4. We started with 6,242 Li-containing oxides with at least three elements from the ICSD database.[156] For each compound, we constructed its Li diffusion network and analyzed its percolation dimensionality, as described earlier. At this step, invalid structures (e.g., invalid cif files, missing Li, unfit for Delaunay tetrahedralization, etc.) were excluded, and only Li diffusion networks with percolation dimensionality of 3 were selected. After this round, 4,666 oxides were passed to the next filter.

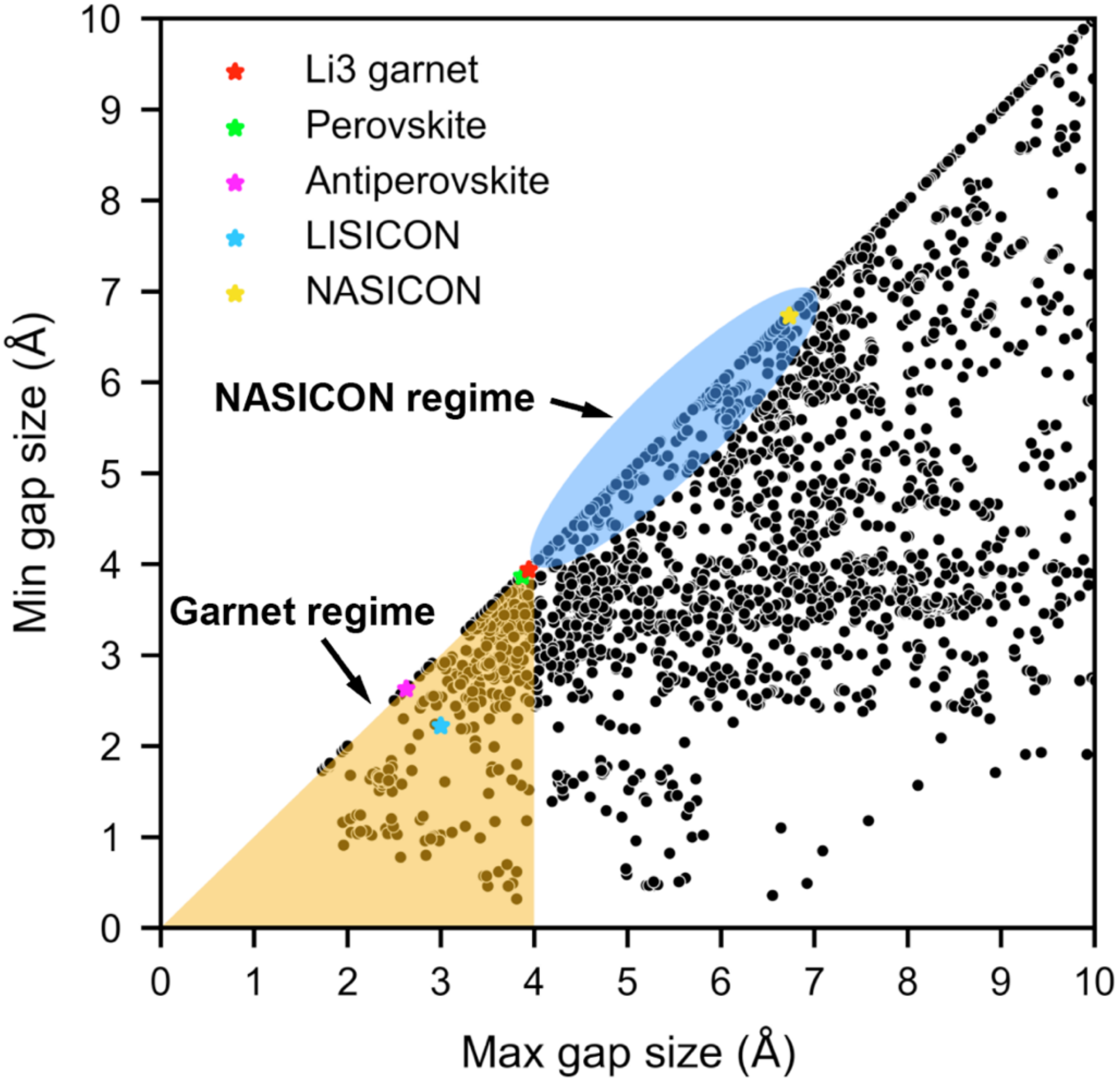

Figure 2.5 Classification of Li diffusion networks using the min and max gap size analysis.

Plot of min gap size vs. max gap size for 4,666 lithium oxides from the Li diffusion network analysis (filter 1). The garnet regime (max gap size ≤ 4 Å) is shaded orange, and the NASICON regime (4 Å < min gap size = max gap size ≤ 7 Å) is shaded blue. Note that the ellipse shown for the NASICON regime is only provided as a visual aid; the actual NASICON regime is only the segment along the diagonal. Red star: Li3 garnet ($Li_3La_3(TeO_6)_2$), green star: perovskite ($Li_{0.33}La_{0.557}TiO_3$), pink star: antiperovskite (LiH_2ClO), blue star: LISICON ($Li_{14}Zn(GeO_4)_4$), yellow star: NASICON ($LiTi_2(PO_4)_3$). See Table 2.S1 for the max and min gap size values of the stars.

Next, we computed the min and max gap sizes of the representative percolation path for each of the remaining 4,666 Li diffusion networks and plotted (max gap size, min gap size) pairs, as shown in Figure 2.5. This min–max gap size plot provides direct visualization of the garnet regime (orange shaded triangle) and the NASICON regime (blue shaded ellipse). There were 1,479 oxides in the garnet regime and 361 oxides in the NASICON regime for a total of 1,840 oxides.

Intriguingly, although the garnet and NASICON regimes were defined using features from the Li3 garnet (red star) and NASICON (yellow star) networks, another three lithium oxide SICs fell into these two regimes, namely, perovskite (green star), antiperovskite (pink star), and LISICON (blue star), as shown in Figure 2.5. Of the five oxide SICs, four have a max gap size ≤ 4 Å, four have homogeneous local environments (the diagonal line), and all of them have a 3D diffusion network. This result is encouraging, as it suggests that the three beneficial features we captured from garnet and NASICON networks are likely shared by a large portion of lithium oxide SICs.

The 1,840 compounds passing the min–max gap size analysis were further grouped into 243 groups (157 for the garnet regime and 86 for the NASICON regime) based on the similarity of their framework structures using the Structure Matcher in the pymatgen software package.[157] Thus, compounds within the same structural group should in principle have similar Li diffusion networks. We only selected one structure from each group (preferably with a composition excluding toxic or radioactive elements) for the subsequent screening procedures, assuming that the non-Li cation chemistry only has a secondary effect on the Li-ion conductivity. This is a reasonable assumption for many lithium SICs where the non-Li cations can be selected from a wide range of elements, such as the garnet[29,54], NASICON,[30,126] and (thio)-LISICON families.[126,158]

Next, we filtered out the following compounds: 1) Compounds for which Li stuffing is difficult. In these compounds, all available vacant sites face-share with multiple cations, likely preventing Li stuffing of the structure. For typical vacant tetrahedral and octahedral sites, we limited the maximum number of face-sharing cations to 2 and 4, respectively (half the number of their polyhedron faces). For example, $LiInO_2$ (ICSD: 44522) has an fcc anion framework where all octahedral sites are occupied by cations. This compound was excluded as every vacant tetrahedral site face-shares with four other cations. 2) Compounds already investigated for lithium electrode or electrolyte applications, including lithium garnets, NASICONs, perovskites, antiperovskites, and electrode materials with redox elements such as Li_2VPO_4F (ICSD: 183877). 3) Compounds with disordered Li sites. These compounds often require computationally expensive ordering of Li configurations. Moreover, when non-Li cations mix with Li ions in the same sites, they may block the Li percolation paths. We note that if the compound has been ordered in the Materials Project database,[159] the ordered structure was still included for later analysis. 4) Compounds with H_2O, NH_4, and OH motifs. Cif files of these compounds often have missing proton coordinates, and they may also lose H_2O and NH_3 during the high-temperature processing.

After this step, 31 compounds remained in the garnet regime and 22 compounds remained in the NASICON regime. Their specific compositions and ICSD IDs are listed in Table 2.S2 and 2.S3, respectively.

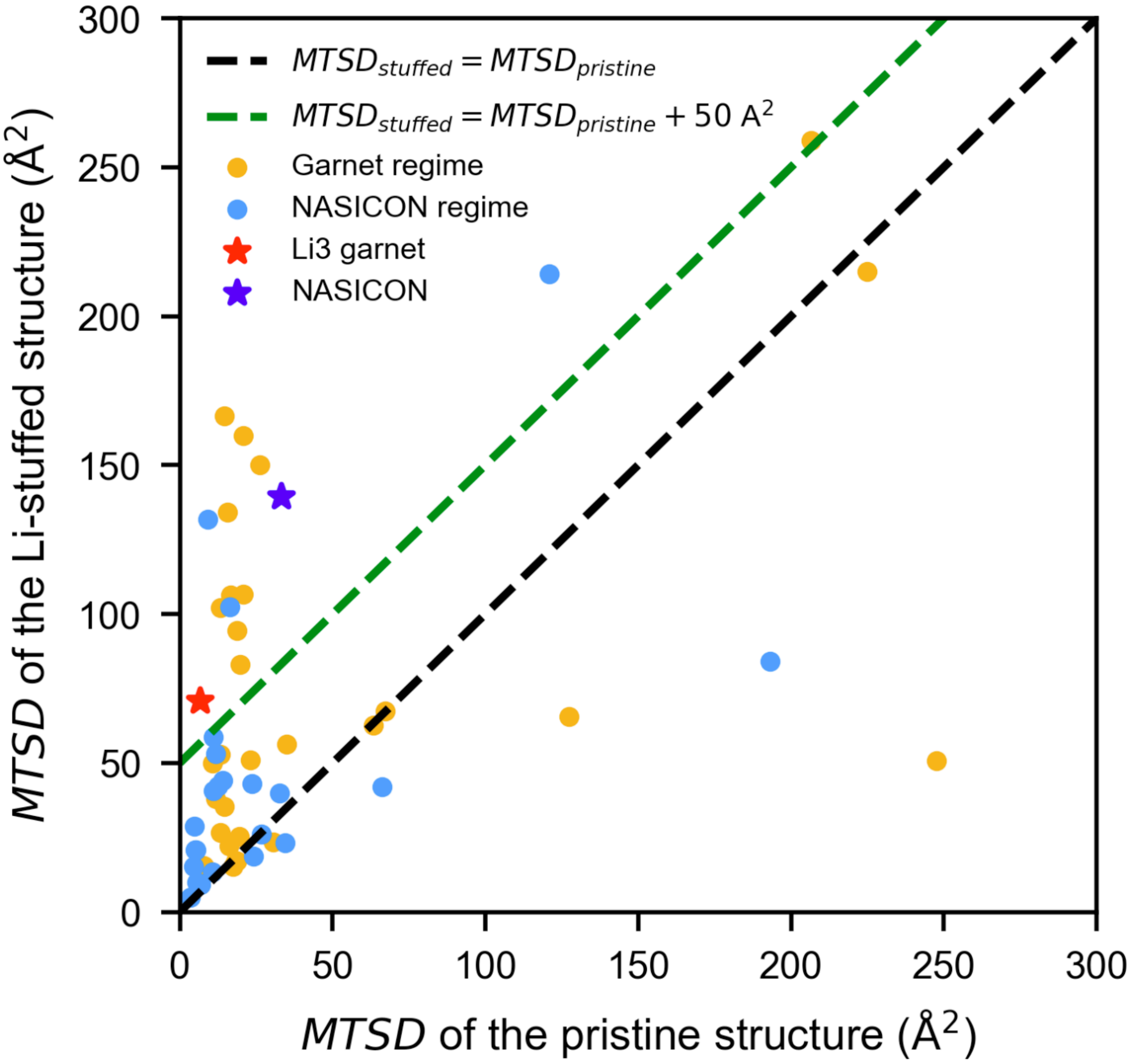

Figure 2.6 Short AIMD simulation results for 53 compounds.
MTSD of the stuffed compound ($MTSD_{stuffed}$) vs. MTSD of the pristine compound ($MTSD_{pristine}$) for 53 compounds over 10-ps short AIMD simulation (Filter 5). The orange and blue points represent compounds from the garnet and NASICON regimes, respectively. Red star: Li3 garnet ($Li_3La_3Te_2O_{12}$), blue star: NASICON ($LiTi_2(PO_4)_3$). Black dashed line: $MTSD_{stuffed} = MTSD_{pristine}$, green dashed line: $MTSD_{stuffed} = MTSD_{pristine}$+ 50 Å^2. Points above the green dashed line were passed to filter 6 for long AIMD simulations.

For these 53 compounds, we evaluated their ionic conductivity before and after Li stuffing using AIMD simulations. However, performing AIMD simulations for all 53 compounds at multiple temperatures and for a long simulation time (≥ 100 ps) would be computationally very expensive.

Instead, for each structure, we performed short AIMD simulations for 10 ps at 1000 K for both the pristine and Li-stuffed compositions to detect signs of drastically improved conductivity upon Li stuffing. If a local environment in the pristine structure could indeed be activated by the stuffed Li ion, a drastic increase was expected in the maximum total square displacement (MTSD) of Li ions obtained from the short AIMD simulation after Li stuffing, which is defined as

$$\mathrm{MTSD} = \max_{0\ \mathrm{ps} \le t \le 10\mathrm{ps}} \sum_{i=1}^{N} |\mathbf{r}_i(t)|^2.$$

Here, N is the number of Li ions, t is a variable between 0 and 10 ps, i is the index of the Li ion, and $\mathbf{r}_i(t)$ is the displacement vector of Li ion i at time t with respect to its initial position $\mathbf{r}_i(t=0)$. We further define the maximum mean square displacement (MMSD) as MTSD / N.

As noted earlier, the "activated diffusion network" model assumes that only the activated local environment contributes to the Li-ion diffusion and that the rest of the networks remain quiescent; therefore, the difference between the MTSD of the stuffed and pristine material ($\mathrm{MTSD}_{\mathrm{stuffed}} - \mathrm{MTSD}_{\mathrm{pristine}}$) reflects only the contribution of the activated local environment to the MTSD. As a reference, $\mathrm{MTSD}_{\mathrm{stuffed}} - \mathrm{MTSD}_{\mathrm{pristine}}$ is 64 Å^2 for Li3 garnet and 106 Å^2 for NASICON over the 10-ps AIMD simulation. We set the threshold for $\mathrm{MTSD}_{\mathrm{stuffed}} - \mathrm{MTSD}_{\mathrm{pristine}}$ at 50 Å^2, above which we considered that the stuffed Li could initiate the activation (step 1). Conceptually, this threshold value is roughly equivalent to one Li ion migrating over 7 Å or two Li ions each migrating over 5 Å within 10 ps. Figure 2.6 plots the MTSD of the Li-stuffed structure ($\mathrm{MTSD}_{\mathrm{stuffed}}$) vs. that of the pristine structure ($\mathrm{MTSD}_{\mathrm{pristine}}$) for the 53 compounds from filter 4. The $\mathrm{MTSD}_{\mathrm{stuffed}} - \mathrm{MTSD}_{\mathrm{pristine}}$ = 50 Å^2 contour line is highlighted in green. There were 10 stuffed compounds in the garnet regime and 3 stuffed compounds in the NASICON regime above the green line; these compounds thus passed the short AIMD filter. Table 2.1 summarizes their compositions, ICSD IDs, and Li-stuffed degrees (number of stuffed Li ions / number of existing Li ions).

In addition to compounds showing signs of improved ionic conductivity only after Li stuffing, the short AIMD simulation also identified the compound $\mathrm{LiGa(SeO_3)_2}$ from the NASICON regime with a high MMSD ≥ 25 Å^2 already in the pristine composition, which is equivalent to every Li ion in the supercell migrating over 5 Å within 10 ps. This compound may already exhibit high ionic conductivity in its pristine form and was thus also included as a candidate for lithium SICs in Table 2.1. In total, 10 compounds in the garnet regime and 4 compounds in the NASICON regime passed the short-AIMD filter. The MTSD and MMSD values of all 53 compounds from the short AIMD simulations are also provided in Table 2.S2 and 2.S3.

In the next filter (Filter 6), we ran long AIMD simulations for at least 100 ps and at least three temperatures (900 K, 1000 K, and 1100 K) for the 14 compounds. Their extrapolated room-temperature conductivities ($\sigma_{\mathrm{rt,stuffed}}$) and activation energies ($E_{\mathrm{a,stuffed}}$) are summarized in Table 2.1. Four compounds in the garnet regime with $\sigma_{\mathrm{rt,stuffed}}$ lower than 0.1 mS/cm were filtered out at this step. As a result, 9 Li-stuffed compounds (6 for the garnet regime and 3 for the NASICON regime) were passed to the next filter for dopability estimation. The compound $\mathrm{LiGa(SeO_3)_2}$ with σ_{rt} of 0.21 mS/cm was added directly to the final list of lithium SIC candidates as no further doping was needed.

In reality, the Li-stuffed compounds require subvalent doping for charge compensation. However, both stuffing Li ions into high-energy sites and substituting elements in the pristine composition may destabilize the structure, as indicated by the positive defect formation energies (E_{defect}) for doping in known SICs.[160,161] For example, we calculated the defect formation energy for the substitution of a Zn^{2+} ion by two Li^+ ions in $LiZnPS_4$ to be 0.46 eV/defect and that for the substitution of Ti^{4+} by Al^{3+} and Li^+ in $LiTi(PO_4)_3$ NASICON to be 0.39 eV/defect. Because a large E_{defect} value suggests poor dopability of the pristine compound and thus poor synthesizability of the stuffed composition, it is important to select a dopant with a low defect formation energy. For each of the 9 compounds that required Li stuffing, we tested dopant ions with a high ion-pair correlation (> 1)[162] or a small Shannon radius difference (< 0.15 Å) with the ion to be doped, and list the dopant with the lowest defect formation energy in Table 2.1. The energy above the hull (E_{above_hull}) values for the doped structures are also listed for readers' reference. We set the criterion for good dopability to be $E_{defect} < 1$ eV/defect, a threshold much higher than that of Al-doped $LiTi_2(PO_4)_3$ (0.39 eV/defect) and Li-doped $LiZnPS_4$ (0.46 eV/defect). This criterion filtered out Li_4SiO_4 and Li_2MgPO_4F from the garnet regime with defect formation energies of 1.52 and 1.33 eV/defect, respectively. Intriguingly, although most of the compounds in Table 2.1 have varying E_{defect} from 0.5 to 0.8 eV/defect, the compound $LiSc(SeO_3)_2$ has an E_{defect} of 0 eV/defect by doping Sc with Mg, indicating that this material is thermodynamically stable even after Li-stuffing.

For the last filter (Filter 8), we ran long AIMD simulations for at least five temperatures between 800 K and 1200 K for the 7 doped structures (4 in the garnet regime and 3 in the NASICON regime). Their extrapolated room-temperature ionic conductivities ($\sigma_{rt,doped}$) and activation energies ($E_{a,doped}$) are provided in the last two columns in Table 2.1. Comparing the activation energy of the doped structure ($E_{a,doped}$) with that of the Li-stuffed structure in filter 6 ($E_{a,stuffed}$), it is clear that subvalent doping increases the activation energy by 0–80 meV, slightly decreasing σ_{rt} by less than one order of magnitude. As a result, all 7 doped compounds still exhibited $\sigma_{rt,doped}$ of approximately 0.1 mS/cm or higher except for the Mg-doped $LiAlO_2$ ($Li_{1+1/32}Mg_{1/32}Al_{1-1/32}O_2$) with $\sigma_{rt,doped}$ of 0.02 mS/cm. Note that although the compound $Li_{3+1/8}Mg_{1/8}Sc_{1-1/8}(BO_3)_2$ in the NASICON regime only exhibited $\sigma_{rt,doped}$ of 0.07 mS/cm, a previous computational study showed that its conductivity can reach 0.1 mS/cm when the Li-stuffed degree is tripled.[66]

Finally, the 6 Li-stuffed compounds passing the last filter were combined with the pristine compound $LiGa(SeO_3)_2$ into a final list of lithium oxide SIC candidates (Table 2.2). Their Arrhenius plots and Li-ion probability densities obtained from AIMD simulations are provided in Figure 2.S5–S11. Based on their Li-ion probability densities, all the candidates indeed have the intended 3D diffusion pathways. For each candidate, information on other compounds in the same structural group is also provided in Table 2.S4–S9. It should be noted that the two candidates $LiGa(SeO_3)_2$ and Mg-doped $LiSc(SeO_3)_2$ actually have the same framework except that Sc cations in $LiSc(SeO_3)_2$ are partially disordered at room temperature, which caused them to be classified into different structural groups in filter 3.

Table 2.1 Summary of properties calculated for filter 6–8 in the high-throughput screening process.
$\sigma_{rt,stuffed}$ and $E_{a,stuffed}$ are the extrapolated room-temperature conductivity and fitted activation energy for the structure with the stuffed Li ion, respectively. Similarly, $\sigma_{rt,doped}$ and $E_{a,doped}$ are those for the doped structure with the stuffed Li ion, respectively. E_{defect} and E_{above_hull} are the defect formation energy and energy above the hull of the doped structure, respectively. Li-stuffed degree = the number of stuffed Li ions / total number of existing Li ions in the supercell. Values not passing the corresponding screening criteria are highlighted in red.

Regime	Pristine composition	ICSD ID	Li-stuffed degree	Filter 6		Filter 7		Filter 8	
				$\sigma_{rt,stuffed}$ and range (mS/cm)	$E_{a,stuffed}$ (meV)	E_{defect} (eV/defect) (doping strategy)	E_{above_hull} (meV/atom)	$\sigma_{rt,doped}$ and range (mS/cm)	$E_{a,doped}$ (meV)
Garnet	Li_4GeO_4	18096	1/64	0.002 [10^{-6}, 2.12]	466 ± 172	--*	--	--	--
	Li_4SiO_4	238603	1/112	10^{-8} [10^{-11}, 10^{-6}]	920 ± 139	--	--	--	--
	Li_3PO_4	257439	1/48	0.02 [10^{-4}, 0.89]	368 ± 100	--	--	--	--
	Li_4SeO_5	92395	1/64	10^{-5} [10^{-11}, 197]	549 ± 374	--	--	--	--
	Li_4SiO_4	98615	1/64	1.19 [0.05, 29]	219 ± 79	1.52 (Al dopes Si)	10.5	--	--
	Li_2MgPO_4F	426198	1/32	4.84 [0.24, 99]	175 ± 75	1.33 (Li dopes Mg)	20.4	--	--
	$LiAlO_2$	430185	1/32	0.08 [10^{-6}, 10^{3}]	315 ± 277	0.76 (Mg dopes Al)	5.9	0.02 [10^{-4}, 2]	333 ± 112
	Li_2TeO_4	1485	1/32	6.2 [0.41, 93]	194 ± 67	0.54 (Nb dopes Te)	4.8	2.72 [0.25, 30]	214 ± 59
	Li_6TeO_6	26297	1/48	0.98 [0.07, 14]	248 ± 65	0.58 (Sb dopes Te)	5.5	0.56 [0.05, 6]	262 ± 59
	Li_6PBrO_5	421480	1/24	8.5 [0.004, 10^{4}]	196 ± 192	0.73 (Si dopes P)	13.9	3.2 [0.17, 60]	199 ± 73
NASICON	$LiGa(SeO_3)_2$	250868	0	0.21 [0.01, 3.6]	316 ± 70	N/A	0	0.21 [0.01, 3.6]	316 ± 70
	$LiSc(SeO_3)_2$	239794	1/4	3.2 [0.08, 122]	216 ± 90	0 (Mg dopes Sc)	0	1 [0.05, 22]	245 ± 77
	$Li_4Ga_3Si_3O_{12}Cl$	87987	1/8	4.6 [0.14, 145]	198 ± 85	0.79 (Mg dopes Ga)	16.8	0.72 [0.04, 12]	271 ± 70
	$Li_3Sc(BO_3)_2$	241234	1/24	0.47 [10^{-5}, 10^{4}]	254 ± 265	0.72 (Mg dopes Sc)	7.4	0.07 [0.002, 2.2]	326 ± 88

Filter 6: Long AIMD simulation of stuffed compounds; Filter 7: Dopability; Filter 8: Long AIMD simulation of doped compounds.

Table 2.2 Final list of Li oxide SIC candidates from high-throughput screening.
σ_{rt} and E_a are the extrapolated room-temperature conductivity and activation energy, respectively. E_{defect} and E_{above_hull} are the defect formation energy and energy above the hull, respectively.

Regime	Final composition	Source ICSD ID	σ_{rt} and range (mS/cm)	E_a (meV)	E_{defect} (eV/defect)	E_{above_hull} (meV/atom)
Garnet	$Li_{2+1/16}Nb_{1/16}Te_{1-1/16}O_4$	1485	2.72 [0.25, 30]	214 ± 59	0.54	4.8
	$Li_{6+1/8}Sb_{1/8}Te_{1-1/8}O_6$	26297	0.56 [0.05, 6.1]	262 ± 59	0.58	5.5
	$Li_{6+1/4}Si_{1/4}P_{1-1/4}O_5Br$	421480	3.2 [0.17, 60]	199 ± 73	0.73	13.9
NA-SICON	$LiGa(SeO_3)_2$	250868	0.21 [0.01, 3.6]	316 ± 70	N/A	0
	$Li_{1+1/4}Mg_{1/4}Sc_{1-1/4}(SeO_3)_2$	239794	1 [0.05, 22]	245 ± 77	0	0
	$Li_{4+1/2}Mg_{1/2}Ga_{3-1/2}Si_3O_{12}Cl$	87987	0.72 [0.04, 12]	271 ± 70	0.79	16.8
	$Li_{3+1/8}Mg_{1/8}Sc_{1-1/8}(BO_3)_2$	241234	0.07 [0.002, 2.2]	326 ± 88	0.72	7.4

2.3 Discussion

2.3.1 Frameworks of final candidates

In a previous study of lithium sulfide SICs, it was demonstrated that the bcc S^{2-} anion framework is better for Li-ion conduction than fcc and hcp frameworks because all tetrahedral Li sites in the bcc framework are energetically close to equivalent and form a –tet–tet–tet– percolating network.[62] When switching to oxides, the O^{2-} anions are less polarizable than S^{2-} anions and therefore the O^{2-} anion framework has less shielding effect. As a result, the Li site energies in oxides are more affected by the Li^+–Li^+ and Li^+–non-Li cation interactions, likely breaking the site energy equivalence in the bcc anion framework. Indeed, among known lithium oxide SICs, the bcc anion framework has only been observed in Li_3OCl antiperovskites where there are no non-Li cations and not in other SICs such as garnets, NASICONs, LISICONs, and perovskites.

Consistent with this observation, none of our final candidates in Table 2.2 can be mapped to a bcc anion framework. Instead, the candidate Nb-doped Li_2TeO_4 (σ_{rt} = 2.7 mS/cm) in the garnet regime has a tetragonally distorted inverse spinel structure with an fcc-like anion framework,[163] as shown in Figure 2.7A and 2.7B for its pristine and doped structures. A Li-based spinel framework features a 3D –tet (8a)–oct (16c)–tet (8a)– Li diffusion network[164], which is topologically equivalent to that of the garnet framework. Furthermore, in both the normal (LiM_2O_4) and inverse ($Li(LiM)O_4$) spinel structures, the tetrahedral 8a sites are fully occupied by Li ions while the octahedral 16c sites are vacant, showing the same site occupancy as that in the Li3 garnet network (Figure 2.1B).[63] These topological similarities between the spinel and garnet frameworks suggest that they may share the same ion-conduction mechanism. Indeed, the pristine Li_2TeO_4 has an activation energy of 1.13 eV,[163] similar to that in the Li3 garnet.[29] Upon Li stuffing, the stuffed Li ion (Li4) is inserted into the octahedral 16c site and displaces a neighboring tetrahedral 8a Li ion (Li2) to another octahedral 16c site, as illustrated in Figure 2.7A and 2.7B, creating two face-sharing tet–oct Li-ion pairs (Li1–Li4 and Li2–Li3). Similar face-sharing tet–oct Li-ion configurations have been observed in lithium garnets as we discussed and also in the high-rate spinel $Li_{4+x}Ti_5O_{12}$ electrode along the $Li_4Ti_5O_{12}$/$Li_7Ti_5O_{12}$ phase boundaries,[165] giving rise to their high ionic conductivities.[63,165–167] The same mechanism is likely also present in the Li-stuffed Li_2TeO_4 to account for its high conductivity of 2.7 mS/cm (Table 2.2). Given these similarities between the spinel and garnet frameworks, we believe that the spinel framework is promising for lithium SIC application. Indeed, a lithium halide spinel $Li_2Sc_{2/3}Cl_4$ was recently reported with a high measured ionic conductivity of 1.5 mS/cm.[49]

The candidate $Li_{6+1/4}Si_{1/4}P_{1-1/4}O_5Br$ has the highest ionic conductivity of 3.2 mS/cm in Table 2.2. Its pristine structure Li_6PO_5Br is the oxide version of the sulfide argyrodite Li_6PS_5X (X=Cl, Br, I) but with a 20% smaller lattice constant.[168] Moreover, Li ions in Li_6PO_5Br reside in the triangular planar center (24g), which also differs from the tetrahedral 48h site occupancy in Li_6PS_5Br.[22] These chemical and structural differences make Li_6PO_5Br a poor ionic conductor with an activation energy that is 330-meV higher than its sulfide counterpart.[168] As shown in Figure 2.7C, upon Li stuffing into Li_6PO_5Br, the stuffed Li ion (Li3) resides in the interstitial tetrahedral 16e site and face-shares with two 24g Li ions (Li1 and Li2), likely facilitating the rate-limiting inter-cage diffusion.[169] The same occupancy of the stuffed Li ion has been recently observed in the Li-stuffed argyrodites $Li_{4.1}Al_{0.1}Si_{0.9}S_4$[129] and $Li_{6.15}Al_{0.15}Si_{1.35}S_{5.4}O_{0.6}$.[170] Therefore, our result demonstrates that the oxy-argyrodite framework can allow fast Li-ion conduction once an excess amount of Li is stuffed into the structure.

The candidate $Li_{4+1/2}Mg_{1/2}Ga_{3-1/2}Si_3O_{12}Cl$ (σ_{rt} = 0.72 mS/cm) is Mg-doped from $Li_4Ga_3Si_3O_{12}Cl$ with the sodalite structure.[171,172] Similar to the argyrodite framework, the sodalite framework also features space-filling cages.[173] Each sodalite cage has a Cl^- ion in its center tetrahedrally coordinated by 4 tetrahedral Li ions, forming a Li_4Cl cluster.[172] In the pristine composition, the activation energy of Li sodalites ranges from 0.83 to 0.95 eV.[174] Upon Li stuffing, as illustrated in Figure 2.7D, the stuffed Li ion (Li9) is inserted into an unoccupied tetrahedral site in a sodalite cage, forming a local Li_5Cl cluster and face-sharing with another tetrahedral Li ion (Li5) in a neighboring cage. The face-sharing tet–tet Li-ion configuration is likely the key factor promoting inter-cage diffusion, as for the $Li_{6+1/4}Si_{1/4}P_{1-1/4}O_5Br$ argyrodite, which drastically reduces the activation energy to only 271 meV (Table 2.2). However, the face-sharing tet–tet Li-ion pairs have rarely been reported in the literature[175] likely due to the strong coulombic repulsion between them, which may explain the relatively large defect formation energy of 0.79 eV/defect for the Mg-doped structure (Table 2.2). We note that the sodalite framework is a robust framework that can accommodate a wide range of cation and anion combinations. For example, ten ICSD compositions for Li oxide sodalites are listed in Table 2.S8. The large chemical space in the sodalite framework creates new possibilities to further optimize its ionic conductivity and dopability, making this framework attractive for further exploration.

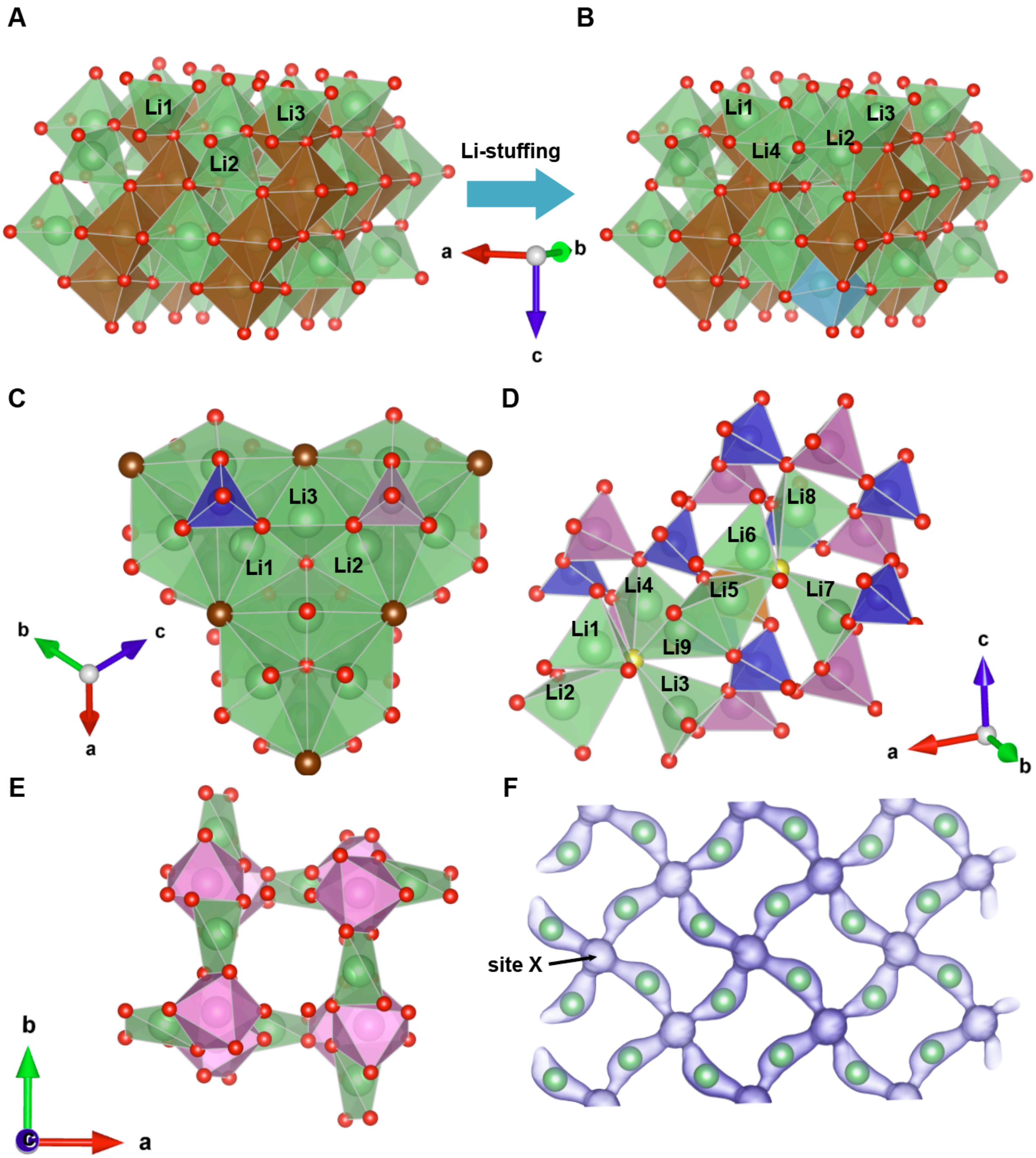

Figure 2.7 Examples of lithium oxide SIC candidates.
(A–B) Crystal structure of Li_2TeO_4 before (A) and after (B) Li stuffing via Nb doping. Li1–3: Li ions in the pristine compound. Li4: the stuffed Li ion.
(C) Crystal structure of $Li_{6+1/4}Si_{1/4}P_{1-1/4}O_5Br$. Li1–2: Li ions in the pristine compound. Li3: the stuffed Li ion.
(D) Crystal structure of $Li_{4+1/2}Mg_{1/2}Ga_{3-1/2}Si_3O_{12}Cl$. Li1–8: Li ions in the pristine compound. Li9: the stuffed Li ion.

(E-F) Crystal structure of $LiGa(SeO_3)_2$ (E) and the isosurface of Li-ion probability density from AIMD simulation at 1000 K (F). Isovalue $P = P_{max} / 50$, where P_{max} is the maximum value of the density. Site X is the intermediate vacant site between neighboring occupied Li sites.
Green polyhedrons: LiO_x, brown octahedrons: TeO_6, light blue polyhedrons: NbO_8, dark blue tetrahedrons: SiO_4, orange octahedrons: MgO_4, purple polyhedrons: PO_4, pink polyhedrons: GaO_x. SeO_3 groups are omitted for clarity. Green spheres: Li ions, yellow spheres: Cl^- anions, brown spheres: Br^- anions, red spheres: O^{2-} anions.

$LiM(SeO_3)_2$ (M = Ga,[176] Sc,[177] Fe[178]) in the NASICON regime presents an intriguing new framework where both the pristine composition $LiGa(SeO_3)_2$ and the Li-stuffed composition $Li_{1+1/4}Mg_{1/4}Sc_{1-1/4}(SeO_3)_2$ were predicted to have high ionic conductivity above 0.1 mS/cm (Table 2.2). The crystal structure of $LiGa(SeO_3)_2$ and Li-ion probability density from AIMD simulation are shown in Figure 2.7E and 2.7F, respectively. There are several interesting features of the framework that can indeed be compared with those in the NASICON framework. First, Li ions in the pristine $LiM(SeO_3)_2$ reside in highly distorted tetrahedral sites (Figure 2.7E),[176,178] similar to the distorted 6b Li sites in the pristine NASICON. The distortion of Li sites has been considered beneficial for frustrating the energy landscape for Li-ion conduction.[179] Second, it has the intended 3D homogenous local environments, as indicated by the equivalent gap sizes in all three dimensions (Table 2.S7). Third, the $LiM(SeO_3)_2$ framework has intermediate low-energy vacant sites ("site X" in Figure 2.7F with high Li-ion density) between occupied Li sites, which is similar to the unoccupied M2 (18e) sites between occupied M1 (6b) sites in the NASICON framework.[138,180] These low-energy vacant sites can bridge the large gap between neighboring Li ions and facilitate Li-ion conduction. These similarities between the $LiM(SeO_3)_2$ and NASICON frameworks make $LiM(SeO_3)_2$ an intriguing candidate for SIC application. Furthermore, DFT results show that upon Li stuffing, the stuffed Li ion is inserted into the low-energy site X (Figure 2.S9A), explaining the excellent dopability ($E_{defect} = 0$ eV/defect) of the $LiM(SeO_3)_2$ framework.

2.3.2 Effect of Li-stuffed amount

In our "activated diffusion network" model, a single stuffed Li ion should in principle be sufficient to activate one quiescent local environment and create a steep increase in ionic conductivity. Therefore, for simplicity, we only stuffed one Li ion into a supercell during the high-throughput screening. As a result, the Li-stuffed degree was generally low in these Li-stuffed materials, especially for those in the garnet regime where the Li-stuffed degree is typically below 5% (Table 2.1). Therefore, there is still considerable room to increase the Li-stuffed degree to optimize the ionic conductivity. For example, in the candidate $Li_{3+x}Mg_xSc_{1-x}(BO_3)_2$, when x is increased from 1/8 to 3/8, the ionic conductivity increases from 0.07 to 0.1 mS/cm.[66] However, the metastability of the compound measured by E_{above_hull} is also tripled from 7.4 to 21 meV/atom.[66] This is because as the Li-stuffed degree increases, the number of activated local environments increases, providing more carriers for ionic conduction but also making the structure less stable. Therefore, the often observed trade-off between the ionic conductivity and stability in SIC development[127] should be considered when tuning the Li-stuffed degree.

As the Li-stuffed degree increases beyond the dilute limit, its effect becomes difficult to be predicted by our model. For example, as the Li concentration in garnet increases toward Li7, the dominant Li-ion triplet arrangement changes from the tet–oct–tet type to the oct–tet–oct type, leading to a different ion-conduction mechanism than that in the Li3+δ garnet.[63,135,166] Eventually, the ionic conductivity is expected to decrease with the Li-stuffed degree once the low vacancy concentration becomes a limiting factor for Li-ion conduction.

2.3.3 Limitations and new possibilities

Earlier works using Li diffusion network analysis focused on determining potential mobile ion sites, migration channel size, and conduction dimensionality.[181–184] A recent work by He et al. considered the presence of “enlarged Li sites” in the network as a key feature for lithium SICs and used it as a screening criterion for finding new SICs.[66] In the present work, we demonstrated two new network features for lithium oxide SICs, i.e., a small max gap size and homogeneous local environments. Successes in predicting new lithium SICs based on these network features highlight the usefulness of geometrical–topological analysis in the study of SICs.

However, several limitations of this work arise from assumptions made to simplify the network analysis and first-principles calculations. First, the representative percolation path is assumed to be the one with the smallest max gap size, and the stuffed Li ion is assumed to be inserted into this path. In reality, the failure of either assumption will make the min–max gap size analysis (filter 2) irrelevant. Second, results from the 10-ps short AIMD simulation (filter 5) suffer from high statistical variance, which may lead to false negatives in the screening process that cannot be detected downstream. Third, we only selected one composition from each structural group in filter 3 and only selected one doped structure for AIMD simulation in filter 8, it is possible that the selected chemistries were not optimal for ionic conductivity or dopability. Future work will be devoted to exploring the chemical space, especially in promising frameworks including the spinel, oxy-argyrodite, sodalite, and $LiM(SeO_3)_2$ frameworks.

Finally, our approach for finding new lithium oxide SICs is in principle applicable to other ionic conductors (e.g., Na^+ and Ca^{2+} mobile ions) and other anion chemistries (e.g., sulfides, nitrides, and chlorides). However, the strength of coulombic interactions between mobile ions in those systems may vary depending on the specific cation and anion chemistries. For example, the coulombic force between two Ca^{2+} ions will be four times stronger than that for Li ions at the same separation. In contrast, for lithium sulfides, because of its large lattice constant and the large anion polarizability of S^{2-} anions,[62] the coulombic interaction between Li ions in sulfides would be weaker than that in oxides. These differences may affect the effectiveness of ion stuffing in activating the diffusion network.

2.4 Conclusions

In summary, by exploring the Li-ion conduction mechanisms in Li-stuffed Li3 garnet and NASICON viewing from their Li diffusion networks, a common pattern of “activated diffusion network” was identified. Three network features were observed to be beneficial for enabling this pattern: a 3D percolation Li diffusion network, a small gap size between occupied Li sites, and homogenous local environments. We then performed a high-throughput screening for garnet-like and NASICON-like compounds sharing these features and used Li stuffing to activate the intended ion conduction mechanism. First-principles calculations were used to evaluate the room-temperature ionic conductivity and dopability of the candidate structures. Finally, we propose 7 compounds as promising lithium oxide SIC candidates. Moreover, several intriguing frameworks emerged for the future development of lithium oxide SICs, including the spinel, oxy-argyrodite, sodalite, and $LiM(SeO_3)_2$ frameworks.

2.5 Methods

Structure grouping

Structure grouping was performed using the Structure Matcher in the pymatgen software package.[157] The structure from the ICSD was preprocessed sequentially by 1) replacing the disordered sites with the species having the highest site occupancy, 2) replacing non-Li cations with a dummy cation, 3) replacing all anions with O^{2-}, and 4) removing all Li sites. Two structures are in the same group if their unit cells or primitive cells could be matched with distortions smaller than the default thresholds.

First-principles calculations

All the DFT calculations were performed within the projector augmented wave (PAW) formalism[185] as implemented in the Vienna ab initio simulation package (VASP).[186] For the exchange-correlational functional, a mixed scheme of the generalized gradient approximation (GGA)[187] and GGA with the rotationally invariant Hubbard (+U) correction[188,189] was employed, as described in the work by Jain et al.[190]

NEB method

We performed NEB calculations[191] in DFT for the Li-stuffed garnet $Li_{3+1/8}La_3Te_2O_{12}$ with the initial and final Li-ion configurations shown in Figure 2.2B and 2.2C, respectively. The charge of the stuffed Li ion was compensated by a uniform background charge to retain the oxidation state for all ions. An energy cut-off of 400 eV, a gamma-point-only sampling of k-space, and 5 intermediate images were used. The NEB calculation was performed at constant volume and was non-spin-polarized.

AIMD simulations

We performed AIMD simulations in VASP at five or more temperatures between 800 K and 1200 K. A timestep of 2 fs was selected. At the beginning of the simulation, the temperature was set at 100 K according to a Boltzmann distribution. Next, the temperature was ramped up to the target temperature in 2 ps by velocity scaling, and then the supercell was equilibrated at the target temperature for 5 ps in the NVT ensemble with a Nosé–Hoover thermostat.[192,193] After equilibrium, AIMD simulations were continued in the NVT ensemble at the target temperature for another 10 ps for short AIMD simulations (filter 5) or at least 100 ps for long AIMD simulations (filter 6 and filter 8). An energy cut-off of 400 eV and a gamma-point-only sampling of k-space were used. All the calculations were performed at constant volume and were non-spin-polarized. The analyses of AIMD results used the scheme proposed by He et al.[194] The Li-ion probability density calculation was performed using the scheme proposed by Wang et al.[62] For all the analyses above, we excluded the data point if melting was observed.

Site for the stuffed Li ion

For a given crystal structure, the candidate sites for Li stuffing were the 20 symmetrically distinct Voronoi sites with the lowest energies modeled by the Buckingham potential.[195] DFT calculations were performed on the 20 supercells, each with a stuffed Li ion in a candidate site and with a uniform background charge. The candidate site associated with the lowest DFT energy was selected as the site for the stuffed Li ion. An energy cut-off of 400 eV and a k-point grid of at least 1000/(number of atoms) were used. All the calculations were performed at constant volume and were non-spin-polarized.

Dopability

The defect formation energy (E_{defect}) was calculated as

$$E_{defect} = E_{doped} - E_{pristine} + \sum_i \Delta n_i \mu_i.$$

Here, E_{doped} and $E_{pristine}$ are the bulk energies of the doped and pristine structures, respectively. Δn_i is the number of atoms of element i being added to or removed from the supercell during the doping, and μ_i is the chemical potential of element i at the pristine composition. For the bulk energy calculations of pristine and doped compounds, an energy cut-off of 520 eV and a k-point grid of at least 1000/(number of atoms) were used.

To calculate the energy above the hull (E_{above_hull}) of the doped structure, we constructed the lower energy convex hull using all ground-state phases (including the doped structure) in the chemical space defined by elements in the doped composition using the pymatgen software package.[157] E_{above_hull} was defined as the energy of the doped structure above the lower convex hull. An E_{above_hull} value of 0 eV/atom means that the doped structure is precisely on the hull and therefore thermodynamically stable.

2.6 Supporting information

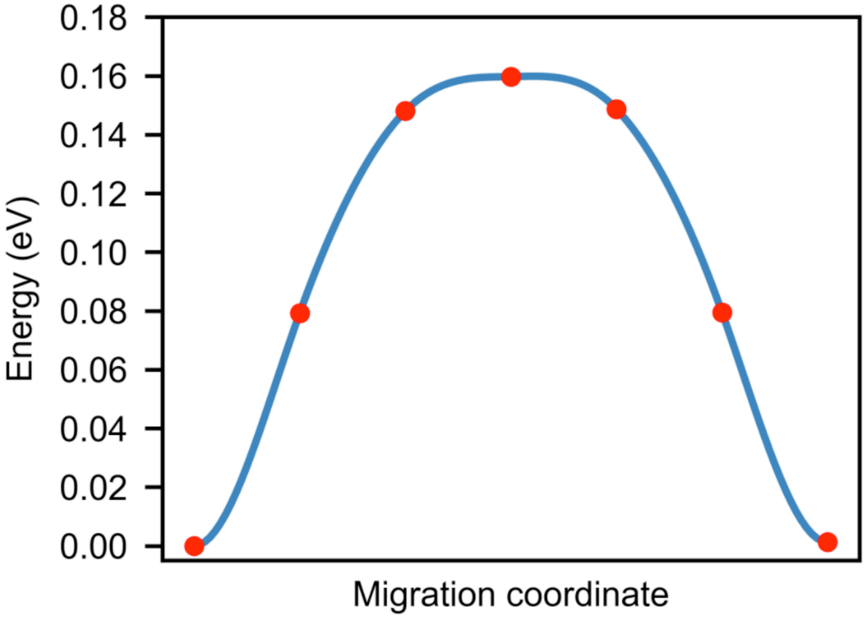

Figure 2.S1 Energy landscape along the minimum energy path for the cooperative motion mechanism in the Li-stuffed garnet $Li_{3+1/8}La_3Te_2O_{12}$.

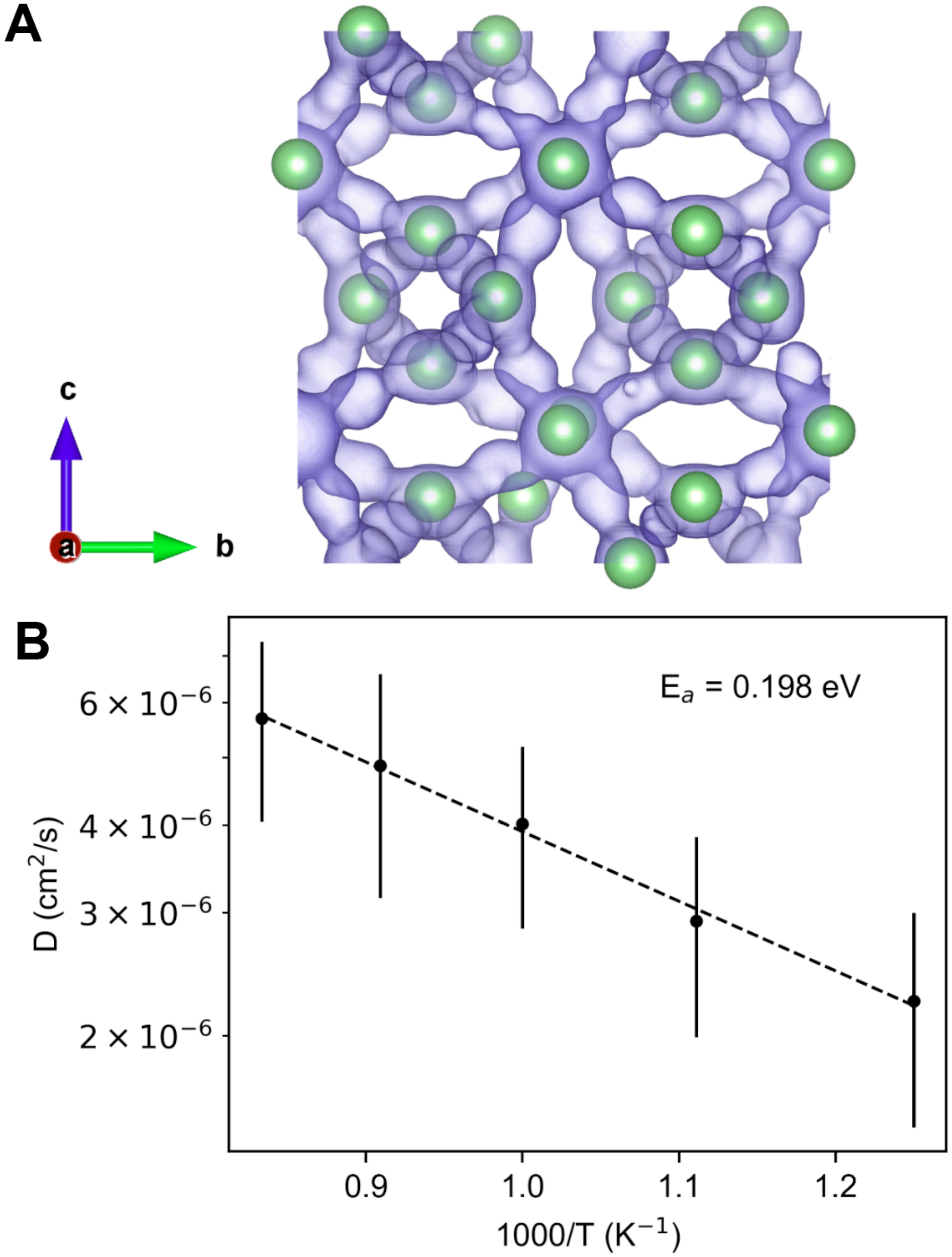

Figure 2.S2 AIMD simulation result of the Li-stuffed garnet $Li_{3+1/8}La_3Te_2O_{12}$.
(A) Isosurface of Li-ion probability density from AIMD simulation at 1000 K, showing the 3D diffusion network. Isovalue $P = P_{max} / 1000$, where P_{max} is the maximum value of the density. Green spheres: Li ions at 0 K.
(B) Arrhenius plot of Li-ion diffusivity with a fitted activation energy of 198 ± 84 meV.

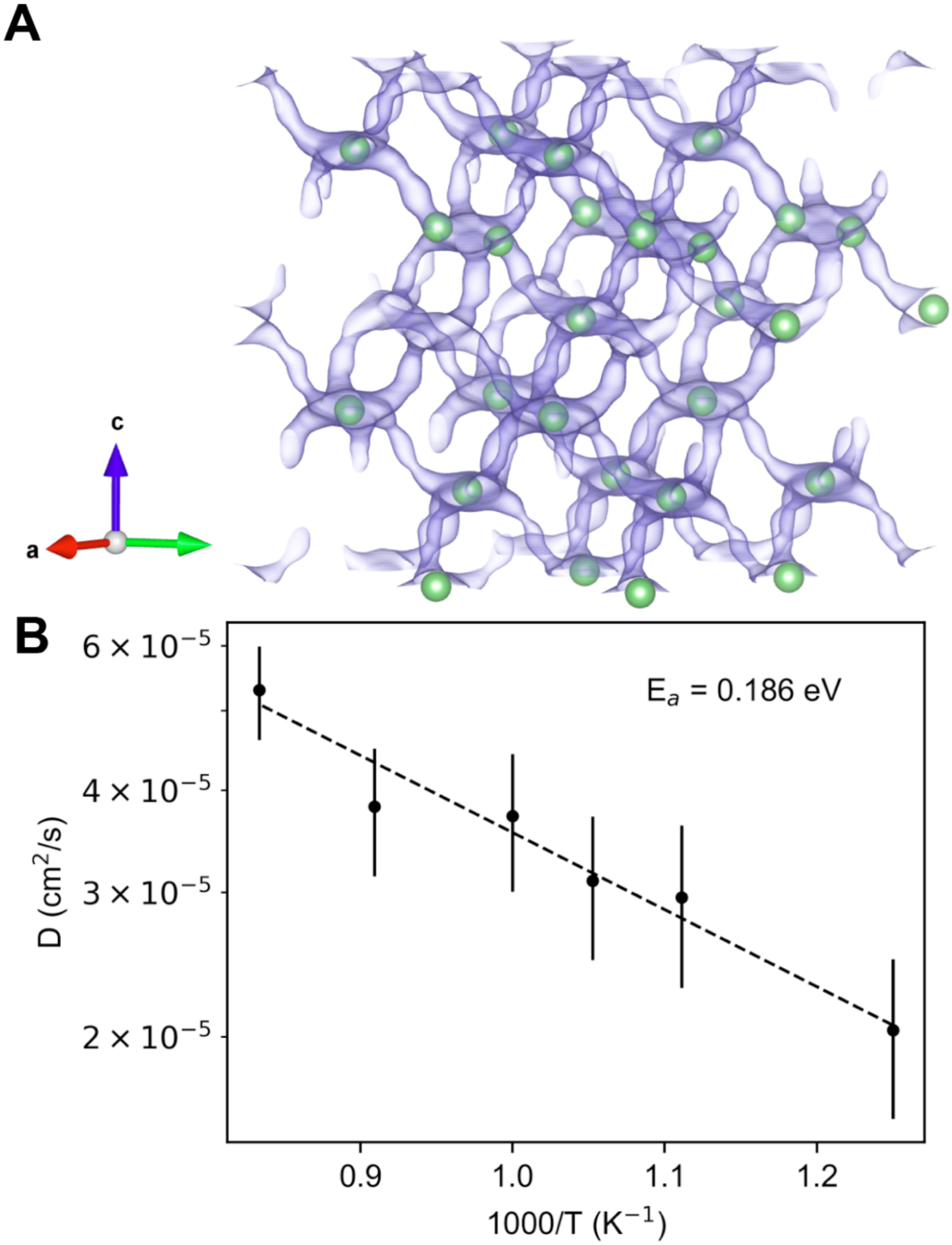

Figure 2.S3 AIMD simulation result of the Li-stuffed NASICON $Li_{1+1/6}Ti_2(PO_4)_3$.
(A) Isosurface of Li-ion probability density from AIMD simulation at 1000 K, showing the 3D diffusion network. Isovalue $P = P_{max} / 50$, where P_{max} is the maximum value of the density. Green spheres: Li ions at 0 K.
(B) Arrhenius plot of Li-ion diffusivity with a fitted activation energy of 186 ± 47 meV.

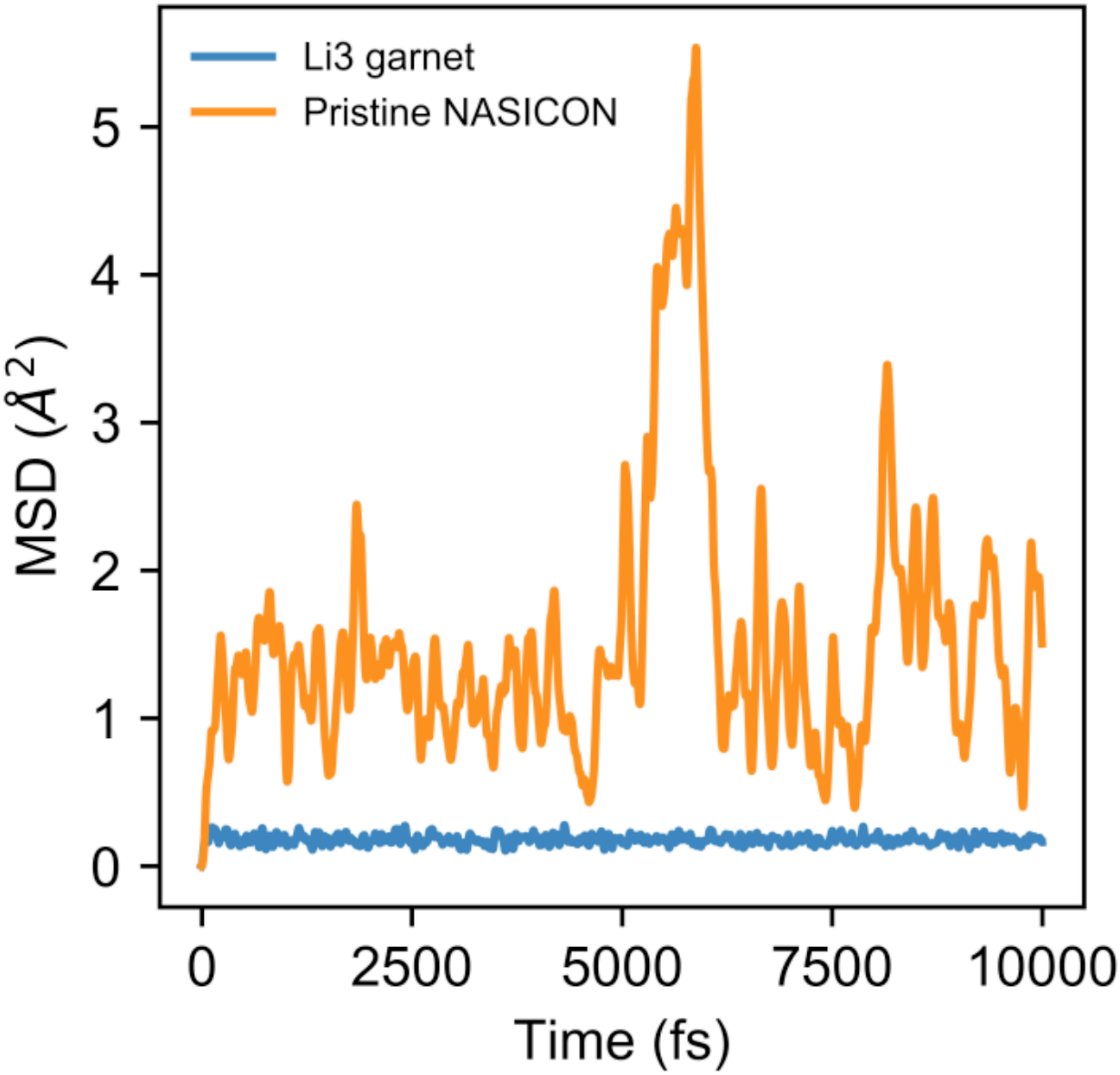

Figure 2.S4 Mean square displacement (MSD) vs. time for 10-ps AIMD simulations of Li3 garnet and pristine NASICON structures at 1000 K.

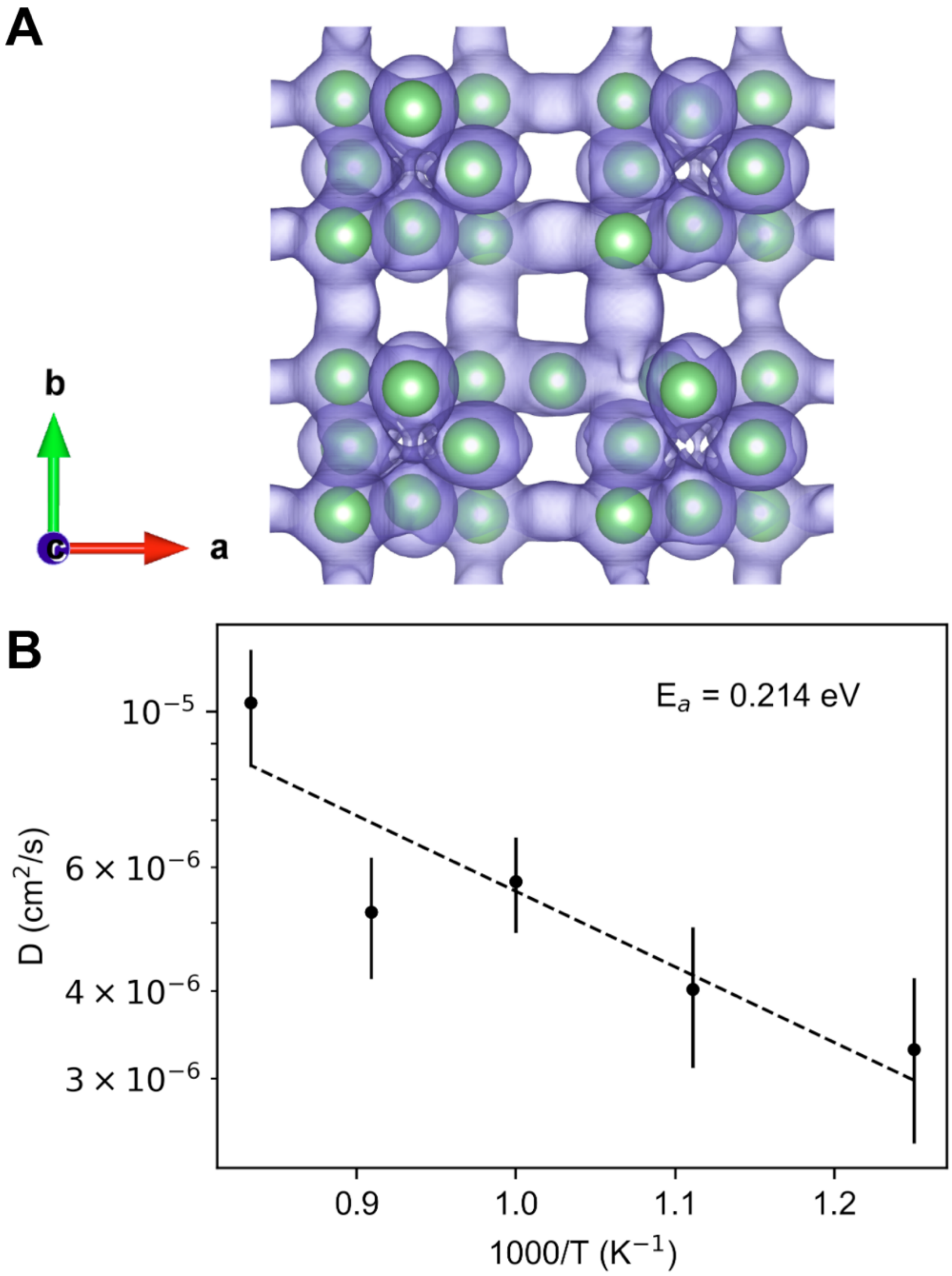

Figure 2.S5 AIMD simulation result of $Li_{2+1/16}Nb_{1/16}Te_{1-1/16}O_4$.
(A) Isosurface of Li-ion probability density from AIMD simulation at 1000 K, showing the 3D diffusion network. Isovalue $P = P_{max} / 1000$, where P_{max} is the maximum value of the density. Green spheres: Li ions at 0 K.
(B) Arrhenius plot of Li-ion diffusivity with a fitted activation energy of 214 ± 59 meV.

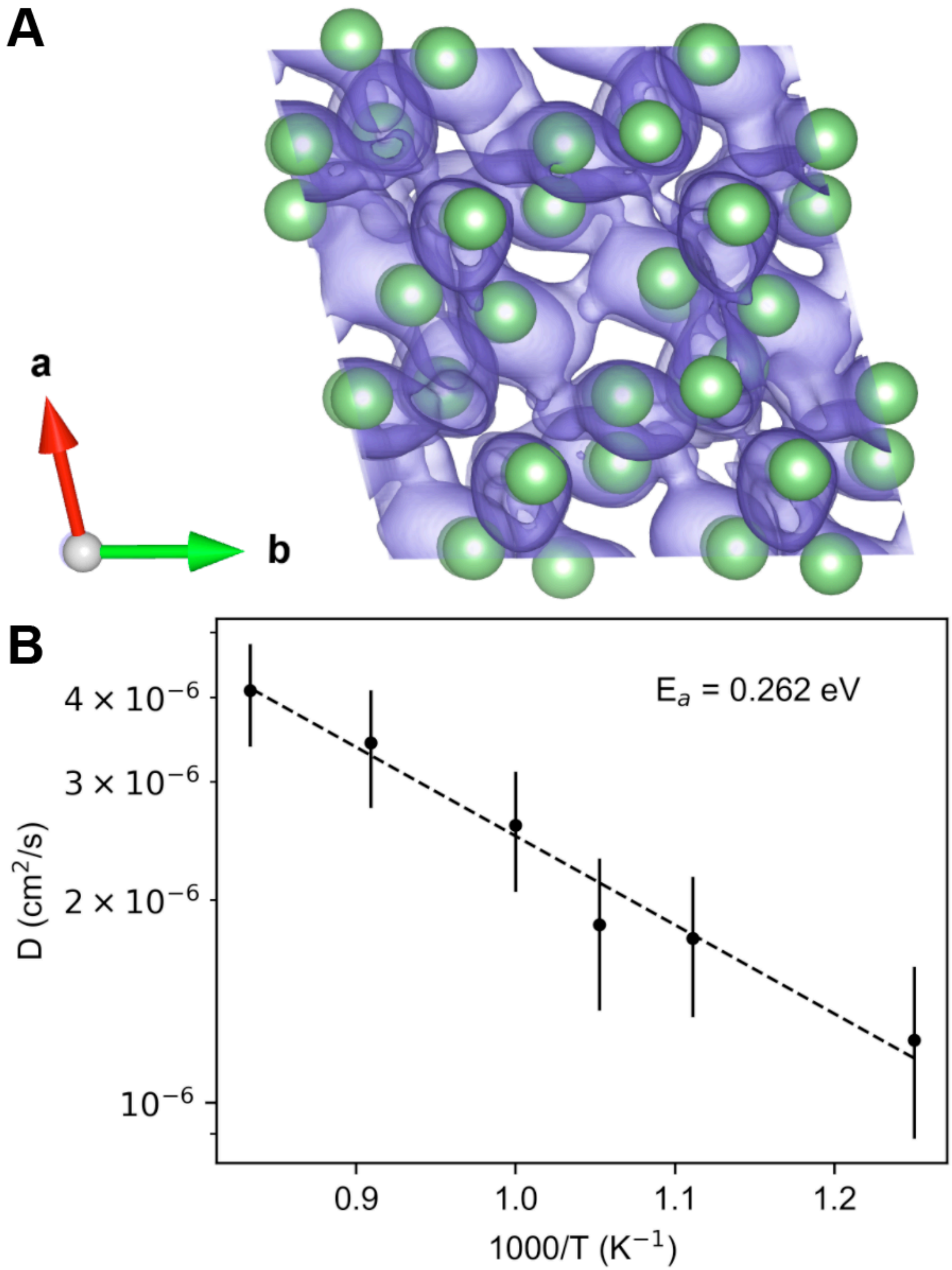

Figure 2.S6 AIMD simulation result of $Li_{6+1/8}Sb_{1/8}Te_{1-1/8}O_6$.
(A) Isosurface of Li-ion probability density from AIMD simulation at 1000 K, showing the 3D diffusion network. Isovalue $P = P_{max} / 1000$, where P_{max} is the maximum value of the density. Green spheres: Li ions at 0 K.
(B) Arrhenius plot of Li-ion diffusivity with a fitted activation energy of 262 ± 59 meV.

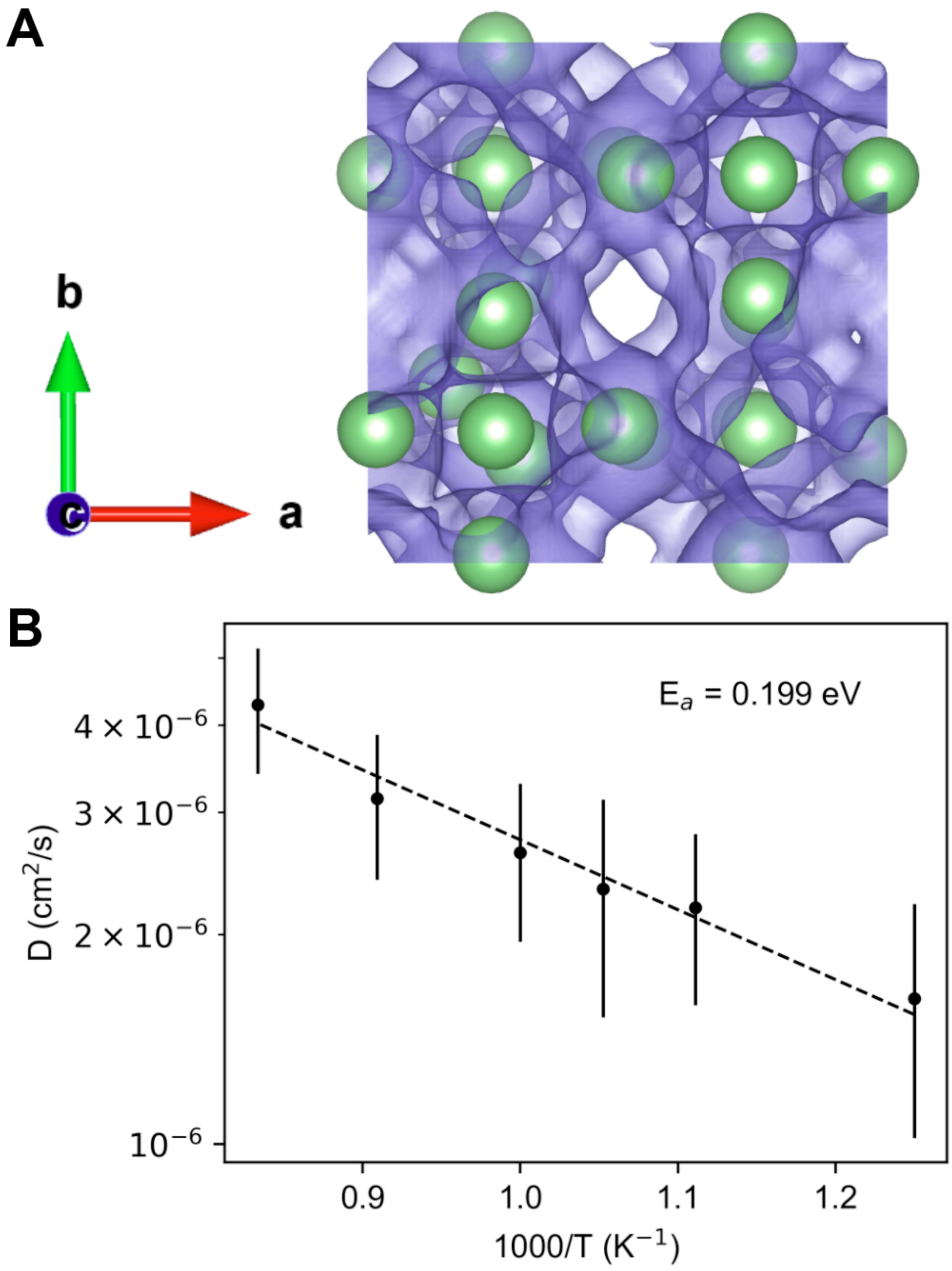

Figure 2.S7 AIMD simulation result of $Li_{6+1/4}Si_{1/4}P_{1-1/4}O_5Br$.
(A) Isosurface of Li-ion probability density from AIMD simulation at 1000 K, showing the 3D diffusion network. Isovalue $P = P_{max} / 1000$, where P_{max} is the maximum value of the density. Green spheres: Li ions at 0 K.
(B) Arrhenius plot of Li-ion diffusivity with a fitted activation energy of 199 ± 73 meV.

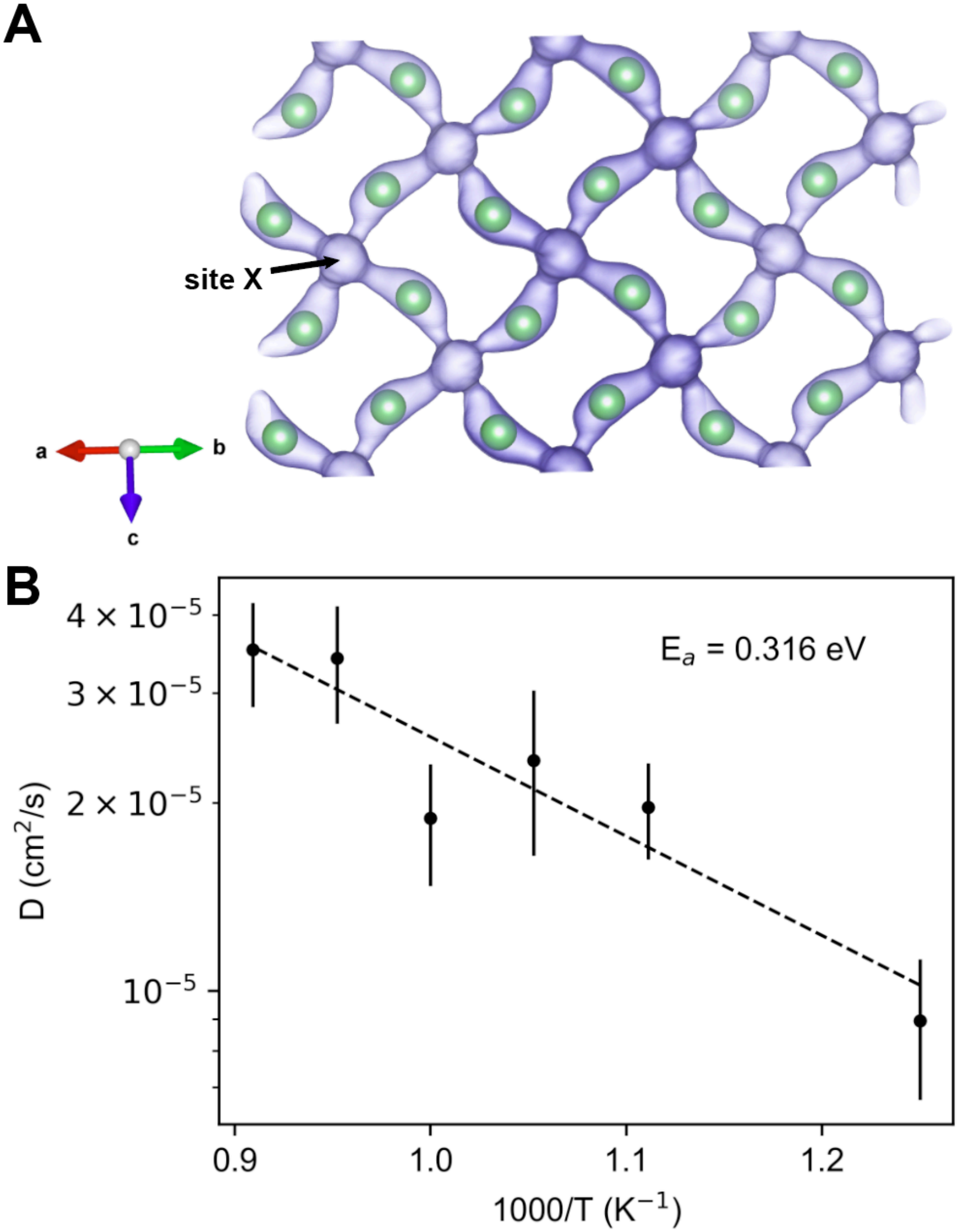

Figure 2.S8 AIMD simulation result of LiGa(SeO_3)$_2$.
(A) Isosurface of Li-ion probability density from AIMD simulation at 1000 K, showing the 3D diffusion network. Isovalue $P = P_{max} / 50$, where P_{max} is the maximum value of the density. Green spheres: Li ions at 0 K. Site X is the vacant intermediate site between neighboring occupied Li sites at 0 K.
(B) Arrhenius plot of Li-ion diffusivity with a fitted activation energy of 316 ± 70 meV.

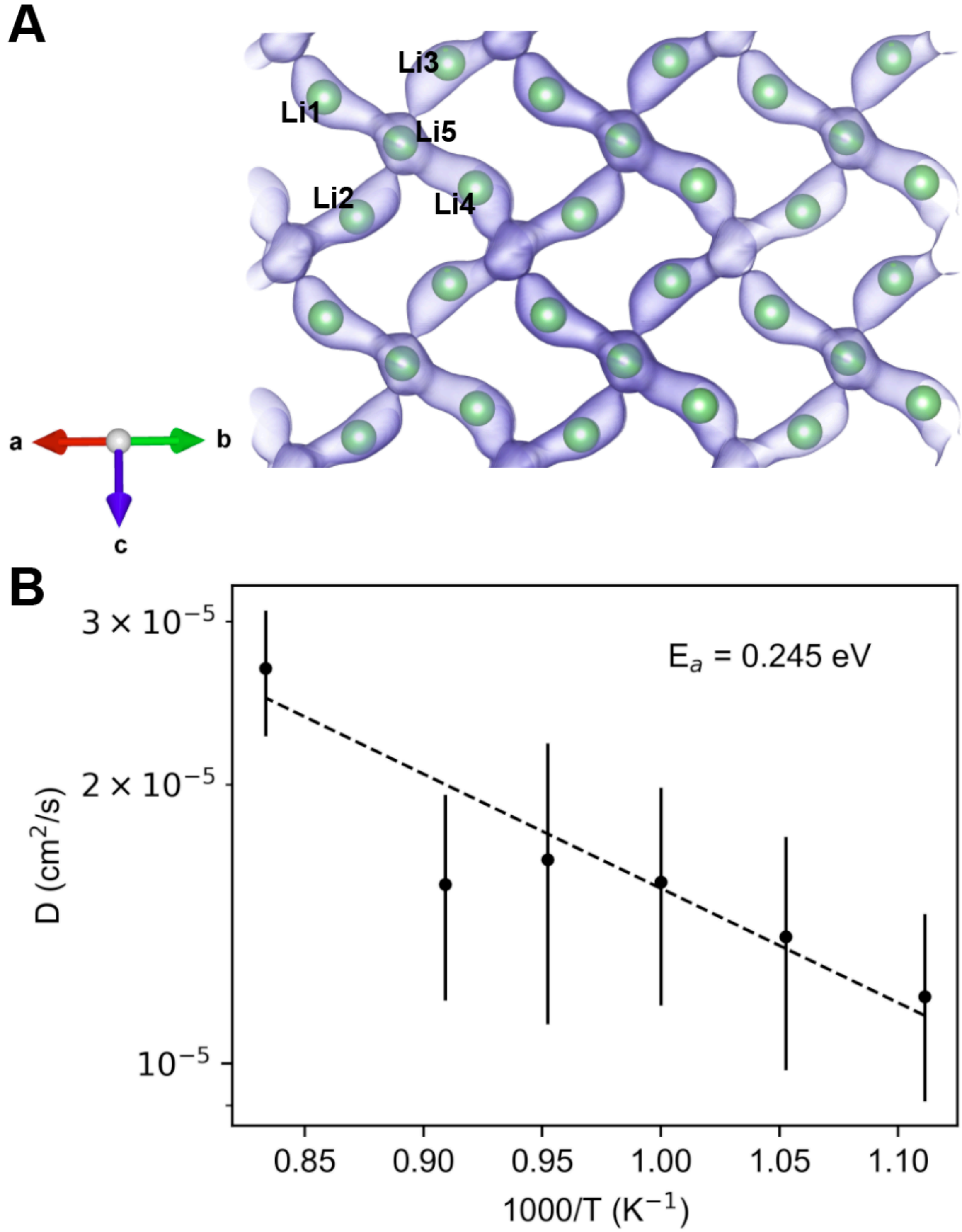

Figure 2.S9 AIMD simulation result of $Li_{1+1/4}Mg_{1/4}Sc_{1-1/4}(SeO_3)_2$.
(A) Isosurface of Li-ion probability density from AIMD simulation at 1000 K, showing the 3D diffusion network. Isovalue $P = P_{max} / 100$, where P_{max} is the maximum value of the density. Green spheres: Li ions at 0 K. Li1–Li4: Li ions in the pristine structure. Li5: stuffed Li ion.
(B) Arrhenius plot of Li-ion diffusivity with a fitted activation energy of 245 ± 77 meV.

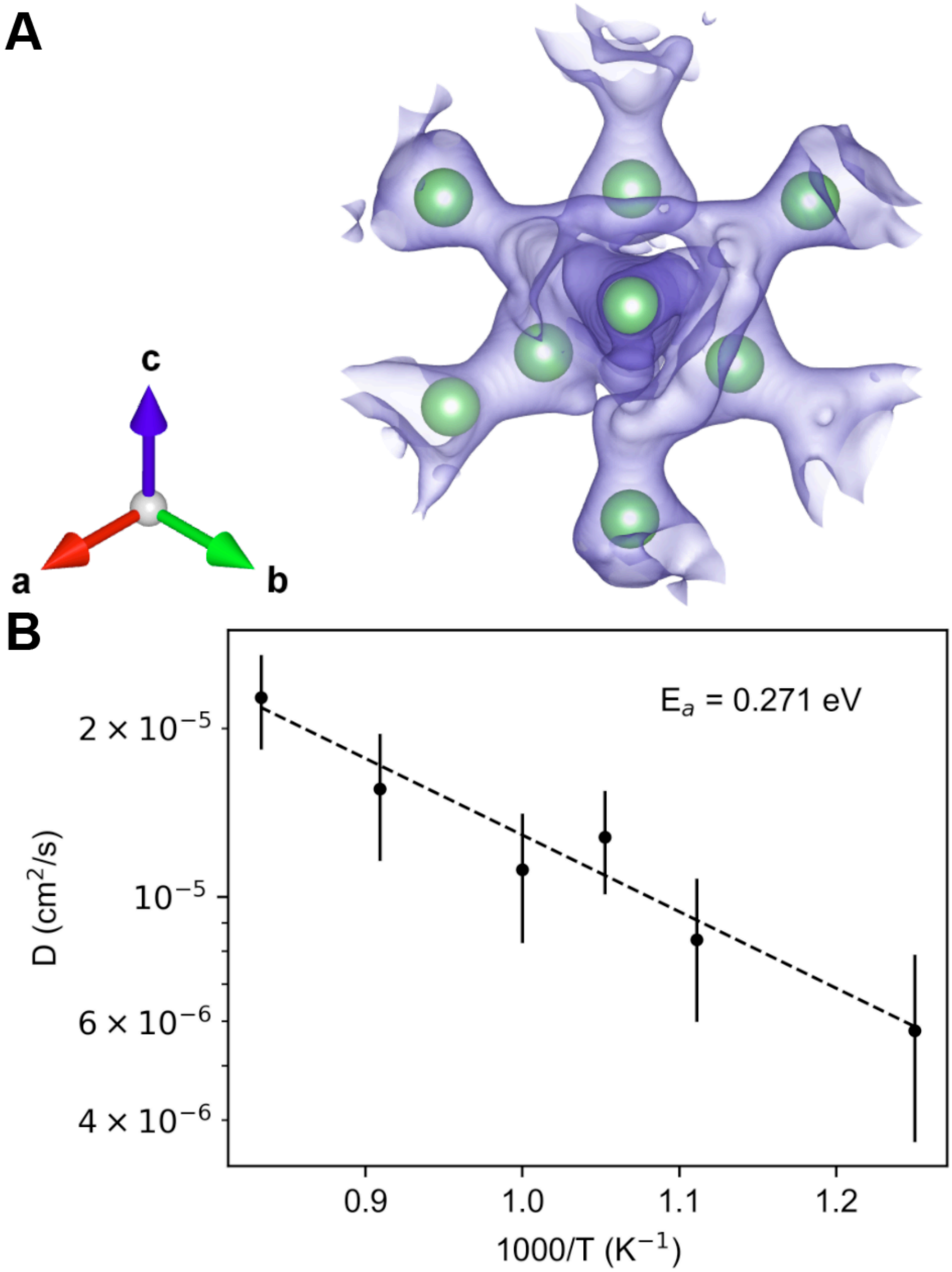

Figure 2.S10 AIMD simulation result of Li$_{4+1/2}$Mg$_{1/2}$Ga$_{3-1/2}$Si$_3$O$_{12}$Cl.
(A) Isosurface of Li-ion probability density from AIMD simulation at 1000 K, showing the 3D diffusion network. Isovalue $P = P_{max} / 1000$, where P_{max} is the maximum value of the density. Green spheres: Li ions at 0 K.
(B) Arrhenius plot of Li-ion diffusivity with a fitted activation energy of 271 ± 70 meV.

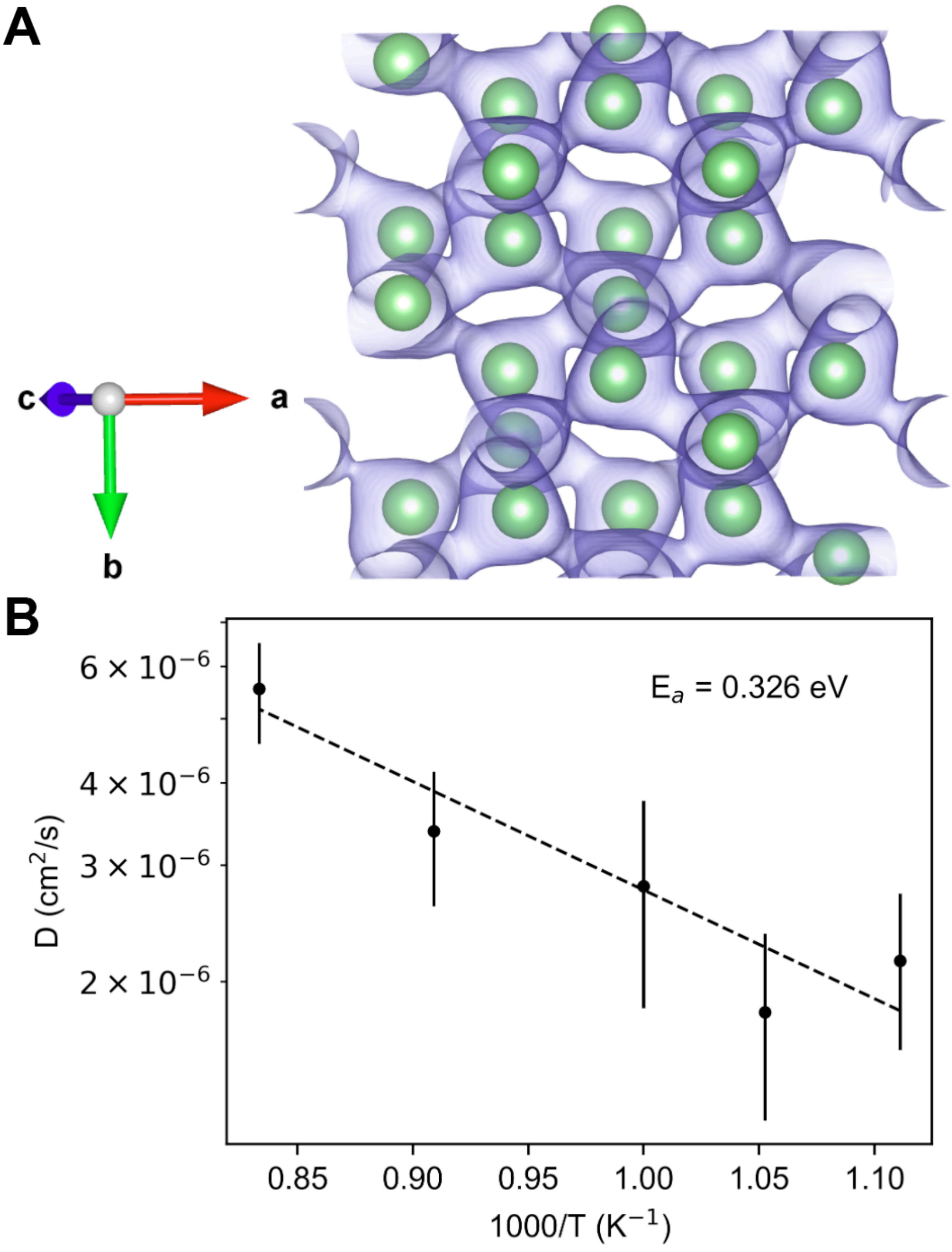

Figure 2.S11 AIMD simulation result of $Li_{3+1/8}Mg_{1/8}Sc_{1-1/8}(BO_3)_2$.
(A) Isosurface of Li-ion probability density from AIMD simulation at 1000 K, showing the 3D diffusion network. Isovalue $P = P_{max} / 1000$, where P_{max} is the maximum value of the density. Green spheres: Li ions at 0 K.
(B) Arrhenius plot of Li-ion diffusivity with a fitted activation energy of 326 ± 88 meV.

Table 2.S1 Maximum and minimum gap sizes in typical Li oxide SIC structures.

Material	**Composition**	**ICSD**	**Max gap size (Å)**	**Min gap size (Å)**
Garnet	$Li_3La_3(TeO_6)_2$	Modified from 68252	3.94	3.94
Perovskite	$Li_{0.33}La_{0.557}TiO_3$	82671	3.87	3.87
Antiperovskite	LiH_2ClO	23748	2.63	2.63
LISICON	$Li_{14}Zn(GeO_4)_4$	100169	3.00	2.22
NASICON	$LiTi_2(PO4)_3$	183669	6.73	6.73

Table 2.S2 Diffusion data from the short AIMD simulations (Filter 5) for the 31 compounds in the garnet regime.

$MTSD_{pristine}$ and $MTSD_{stuffed}$ are the maximum total square displacement of the pristine structure and Li-stuffed structure in 10 ps, respectively. $MMSD_{pristine}$ is the maximum mean square displacement of the pristine structure in 10 ps. MMSD values higher than 25 $Å^2$ and $MTSD_{stuffed}$–$MTSD_{pristine}$ values higher than 50 $Å^2$ are highlighted in red.

Composition	**Source ICSD ID**	**$MTSD_{pristine}$ ($Å^2$)**	**$MTSD_{stuffed}$ ($Å^2$)**	**$MMSD_{pristine}$ ($Å^2$)**	**$MTSD_{stuffed}$–$MTSD_{pristine}$ ($Å^2$)**
$Li_4B_7ClO_{12}$	1125	67.3	67.4	8.4	0.1
Li_4GeO_4	18096	26.1	150.1	0.4	123.9
Li_2TeO_4	1485	15.6	134.1	0.5	118.5
$Li_6Y(BO_3)_3$	68653	224.8	215.0	4.7	-9.8
$LiNbO_3$	5309	17.5	15.4	0.7	-2.1
Li_4SiO_4	238603	206.6	258.9	1.8	52.3
Li_3BO_3	9105	14.7	35.4	0.4	20.7
$LiTaO_3$	239377	30.6	23.4	1.3	-7.2
Li_3PO_4	257439	16.5	106.3	0.3	89.8
Li_2GeO_3	100403	13.4	26.6	0.4	13.2
$LiIO_3$	20032	16.1	22.2	1.0	6.1
Li_6TeO_6	26297	20.8	159.8	0.4	139.0
$Li_6Si_2O_7$	25752	63.3	62.6	2.6	-0.8
Li_2BeSiO_4	28307	8.9	14.2	0.3	5.3
$Li_6Ge_2O_7$	31050	127.4	65.6	2.7	-61.7
Li_3KGeO_4	38324	23.1	51.0	0.5	27.9
$Li_{14}Be_5B_{10}O_{27}$	67991	18.1	16.7	0.6	-1.4
$Li_4Ge_5O_{12}$	68463	247.6	50.7	melted	-197.0
Li_4SeO_5	92395	19.7	83.0	0.3	63.3
$LiZnBO_3$	260590	10.7	49.8	0.7	39.1
Li_4SiO_4	98615	18.8	94.6	0.3	75.8
Li_2MgPO_4F	426198	20.7	106.6	0.6	85.9
Li_3NaSiO_4	202115	11.8	38.1	0.5	26.3
Li_2MgSiO_4	250003	7.9	15.4	0.5	7.6
$Li_7Te_3O_9F$	254737	13.2	52.9	0.5	39.7
$Li_3Al(MoO_4)_3$	262791	18.6	17.1	0.8	-1.5

Li_5OCl_3	419852	2036.9	1974.7	melted	-62.1
Li_6PO_5Br	421480	14.5	166.5	0.6	152.0
$Li_9Mg_3P_4O_{16}F_3$	426103	19.6	25.4	0.5	5.8
$Li_6B_4O_9$	427421	35.0	56.4	0.5	21.4
Li_2AlO_2	430185	13.3	102.2	0.4	88.9

Table 2.S3 Diffusion data from the short AIMD simulations (Filter 5) for the 22 compounds in the NASICON regime.

$MTSD_{pristine}$ and $MTSD_{stuffed}$ are the maximum total square displacement of the pristine structure and Li-stuffed structure in 10 ps, respectively. $MMSD_{pristine}$ is the maximum mean square displacement of the pristine structure in 10 ps. MMSD values higher than 25 $Å^2$ and $MTSD_{stuffed}–MTSD_{pristine}$ values higher than 50 $Å^2$ are highlighted in red.

Composition	**Source ICSD ID**	**$MTSD_{pristine}$ ($Å^2$)**	**$MTSD_{stuffed}$ ($Å^2$)**	**$MMSD_{pristine}$ ($Å^2$)**	**$MTSD_{stuffed}–MTSD_{pristine}$ ($Å^2$)**
$Li_2Cd(PO_3)_4$	636	11.0	40.8	1.4	29.8
Li_2NbOF_5	4409	66.2	42.1	4.1	-24.1
$LiNaSO_4$	67702	34.4	23.1	5.7	-11.2
Li_2CaGeO_4	19024	5.2	20.8	0.3	15.6
$Li_2Mn_3ZnO_8$	26995	4.6	15.3	0.6	10.7
LiB_3O_5	415201	14.1	44.1	0.9	30.0
LiW_3O_9F	38310	12.5	42.2	1.6	29.7
$LiIO_3$	40365	10.6	13.3	0.7	2.6
$Li_4Ga_3Si_3O_{12}Cl$	87987	9.0	131.8	1.1	122.7
$LiIO_3$	201817	11.7	53.1	0.7	41.5
$LiKSO_4$	62982	24.1	18.7	3.0	-5.4
$LiCsSO_4$	63181	26.6	26.1	3.3	-0.5
$LiSiBO_4$	67536	4.7	28.7	0.6	24.0
$LiNO_3$	67981	10.9	58.6	0.7	47.7
$LiGa(SeO_3)_2$	250868	193.1	84.2	48.3	-108.9
$Li_6Ca_{12}Mo_4O_3N_{16}$	83865	5.4	10.0	0.5	4.6
$LiKSO_4$	88832	32.6	39.9	4.1	7.4
$LiSc(SeO_3)_2$	239794	121.0	214.2	15.1	93.1
$Li_3Sc(BO_3)_2$	241234	16.4	102.3	0.7	85.9
$Li_3Rb(Ge_4O_9)_2$	241866	6.8	9.1	1.1	2.3
$Li_2NaB_5O_8F_2$	244622	5.1	20.8	0.6	15.7
$Li_2Be_4BaO_6$	256228	3.4	4.9	0.4	1.5
$LiKMo_3O_{10}$	431337	23.7	43.1	3.0	19.3

Table 2.S4 Max and min gap size data for structures in the same structural group as $Li_{2+1/16}Nb_{1/16}Te_{1-1/16}O_4$

The bolded values are the max and min gap sizes of the representative path.

Composition	**ICSD ID**	**[Max gap size, Min gap size] (Å)**		
		x	**y**	**z**
Li_2TeO_4	1485	**[3.86, 3.39]**	[3.86, 3.39]	[3.39, 3.39]

Table 2.S5 Max and min gap size data for structures in the same structural group as $Li_{6+1/8}Sb_{1/8}Te_{1-1/8}O_6$

The bolded values are the max and min gap sizes of the representative path.

Composition	ICSD ID	[Max gap size, Min gap size] (Å)		
		x	y	z
Li_6TeO_6	26297 40247	**[3.10, 2.94]**	[3.10, 2.94]	[3.10, 2.94]
Li_6UO_6	25350 48209	[3.60, 3.05]	[3.60, 3.05]	**[3.65, 3.05]**

Table 2.S6 Max and min gap size data for structures in the same structural group as $Li_{6+1/4}Si_{1/4}P_{1-1/4}BrO_5$

The bolded values are the max and min gap sizes of the representative path.

Composition	ICSD ID	[Max gap size, Min gap size] (Å)		
		x	y	z
Li_6PBrO_5	421480 421481	**[3.64, 3.20]**	[3.64, 3.20]	[3.64, 3.20]
Li_6PClO_5	421479	**[3.57, 3.18]**	[3.57, 3.18]	[3.57, 3.18]

Table 2.S7 Max and min gap size data for structures in the same structural group as $LiGa(SeO_3)_2$

The bolded values are the max and min gap sizes of the representative path.

Composition	ICSD ID	[Max gap size, Min gap size] (Å)		
		x	y	z
$LiGa(SeO_3)_2$	250868	**[5.97, 5.97]**	[5.97, 5.97]	[5.97, 5.97]
$LiSc(SeO_3)_2$	239794	**[6.21, 6.21]**	[6.21, 6.21]	[6.21, 6.21]
$LiFe(SeO_3)_2$	75554	**[6.04, 6.04]**	[6.04, 6.04]	[6.04, 6.04]

Table 2.S8 Max and min gap size data for structures in the same structural group as $Li_{2+1/2}Mg_{1/2}Ga_{3-1/2}Si_3ClO_{12}$

The bolded values are the max and min gap sizes of the representative path.

Composition	ICSD ID	[Max gap size, Min gap size] (Å)		
		x	y	z
$Li_4Ga_3Si_3O_{12}Cl$	87987	**[6.89, 6.89]**	[6.89, 6.89]	[6.89, 6.89]
$Li_4Ga_3Si_3O_{12}Br$	87988	**[6.85, 6.85]**	[6.85, 6.85]	[6.85, 6.85]
$Li_4Ga_3Si_3O_{12}I$	87989	**[6.86, 6.86]**	[6.86, 6.86]	[6.86, 6.86]
$Li_4Al_3Si_3O_{12}Cl$	68427 41186	**[6.87, 6.87]**	[6.87, 6.87]	[6.87, 6.87]
$Li_4Al_3Ge_3O_{12}Cl$	87990	**[6.93, 6.93]**	[6.93, 6.93]	[6.93, 6.93]
$Li_4Al_3Ge_3O_{12}Br$	87991	**[6.93, 6.93]**	[6.93, 6.93]	[6.93, 6.93]
$Li_4Al_3Ge_3O_{12}I$	87992	**[6.99, 6.99]**	[6.99, 6.99]	[6.99, 6.99]
$Li_4Be_3P_3CO_{12}I$	74525	**[5.28, 5.28]**	[5.28, 5.28]	[5.28, 5.28]
$Li_4Be_3P_3O_{12}Br$	80472	**[5.27, 5.27]**	[5.27, 5.27]	[5.27, 5.27]
$Li_4Be_3As_3O_{12}Cl$	74526	**[6.65, 6.65]**	[6.65, 6.65]	[6.65, 6.65]

Table 2.S9 Max and min gap size data for structures in the same structural group as $Li_{3+1/8}Mg_{1/8}Sc_{1-1/8}(BO_3)_2$

The bolded values are the max and min gap sizes of the representative path.

Composition	ICSD ID	[Max gap size, Min gap size] (Å)		
		x	y	z
$Li_3Sc(BO_3)_2$	241234	[4.58, 2.85]	**[4.89, 4.89]**	[4.89, 2.85]

Supplementary Note

Li sites and Li diffusion network

The algorithm to identify occupied and unoccupied Li sites in a crystal structure is described in Figure 2.S12. As shown in Figure 2.S12, the crystal structure of a Li oxide contains three types of ions: Li ions, non-Li (denoted as "M") cations, and O^{2-} anions. Note that non-Li cations that share the same sites with Li ions were replaced by Li ions. Delaunay tetrahedralization[154,155] was performed on the O^{2-} anion sublattice to generate "**T** tetrahedral sites" (**T** sites). We also constructed "Li polyhedral sites" (**L** site) for each existing Li ion by finding its coordinating anions (bonding distance ≤ 3 Å), and similarly "M polyhedral sites" (**M** sites) for each M cation. Two sites were considered to be in conflict if their center distance ≤ 1 Å. Then, any **T** sites that were in conflict with any **M** sites were removed, and the remaining **T** sites were recursively merged if they were both distorted (Robert/Roux factor[196] ≤ 0.94) and too close to one another (center distance ≤ 1.1 Å). This step produced "**P** polyhedral sites" (**P** sites) which consisted of the unmerged **T** sites and the new sites from merging. Next, we designated any **P** sites in conflict with any **L** sites as the occupied Li sites, and the remaining **P** sites as the unoccupied Li sites. All numerical values were selected to reproduce the known Li sites in the benchmark Li oxide frameworks, including garnet, NASICON, layered $LiCoO_2$, and spinel $LiMn_2O_4$.

To construct the Li diffusion network, we represented all the occupied and unoccupied Li sites as individual nodes in the graph and drew edges between two nodes if the corresponding sites are face-sharing with each other.

Percolation analysis and representative percolation path selection

For each occupied node in the diffusion network and a given direction, we performed the modified Dijkstra's algorithm[197] to find the percolation path with the smallest max gap size to its nearest periodic image in that direction. This step generated multiple percolation paths starting from different occupied nodes in different percolation directions. To select one "representative percolation path" among them for the gap analysis, we made two assumptions: 1) for each percolation direction in the diffusion network, we selected the path with the smallest max gap size, and 2) among the three selected percolation paths for the x, y, and z directions, we further selected the path with the largest max gap size. Assumption 1 was used to exclude tortuous paths consisting mostly of unoccupied sites, and assumption 2 was used to consider only the "worst" direction of the three directions, given that the goal of this work was to find a 3D ionic conductor. With these two assumptions, the representative percolation paths found for garnet and NASICON structures matched the actual conduction paths.

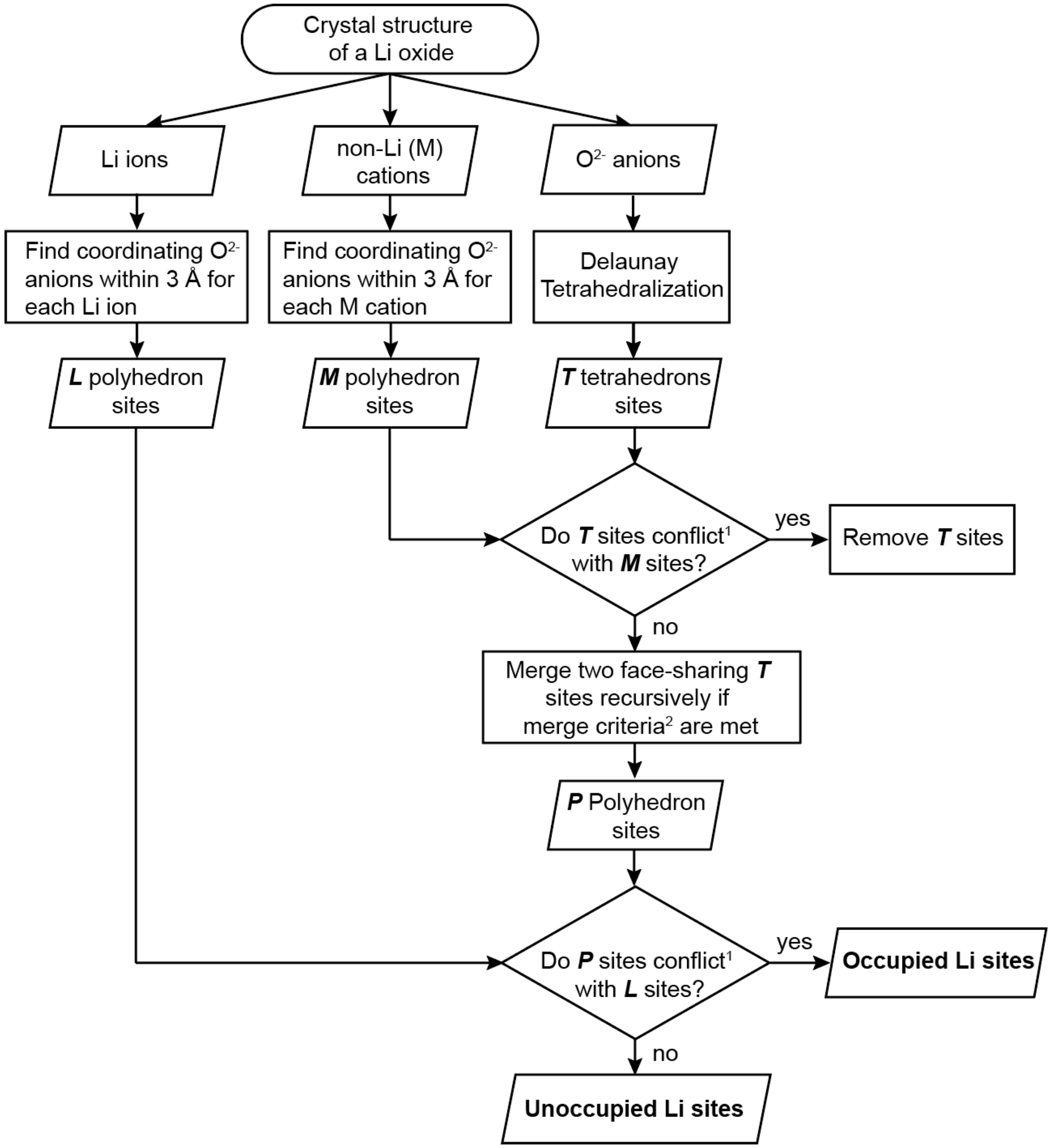

[1] Two sites are in conflict if their center distance ≤ 1 Å.

[2] Merge criteria for face-sharing ***T*** sites: 1) both sites are "distorted" with Robert/Roux factor ≤ 0.94, and 2) their center distance ≤ 1.1 Å.

Figure 2.S12 Flowchart describing the algorithm to identify occupied and unoccupied Li sites in the crystal structure of a Li oxide.

Chapter 3: Computational screening of cathode coatings for solid-state batteries

Part of this chapter has been published in:
Xiao, Y., Miara, L. J., Wang, Y., & Ceder, G. (2019). Computational screening of cathode coatings for solid-state batteries. Joule, 3(5), 1252–1275.

3.1 Introduction

We have shown in Chapter 1 that even with highly conductive SSEs, the cell performance of SSBs is still limited by the high interface resistance at unstable interfaces. Among various interfaces, the cathode/SSE interface is critical as good ion transport across this interface must be maintained for battery cycling. In this chapter, we focused on engineering the cathode/SSE interface by searching for optimal cathode coating materials that can mitigate the high interface resistance.

To date, several oxides used to coat conventional cathode materials have shown varying degrees of effectiveness in SSBs.[61] They include, among others, Li_3PO_4,[117] $LiAlO_2/Al_2O_3$,[118] $LiTaO_3$,[119] $LiNbO_3$,[73,120,121] $Li_4Ti_5O_{12}$,[115,122] Li_2SiO_3,[76] Li_3BO_3,[123] and Li_2ZrO_3,[124] most of which are metal oxides. Cathode coatings are used to isolate the SSEs from the low lithium chemical potentials exerted by the cathode in its highly charged state, thereby preventing their electrochemical self-decomposition. Indeed, most SSEs are not thermodynamically stable at the voltage of many charged cathodes.[77,81,82] In terms of chemical stability, energy dispersive X-ray (EDX) spectroscopy mapping has shown that cathode coatings can also prevent direct contact between the electrode and the SSE, thus suppressing elemental diffusion and interfacial chemical reactions.[76,121] Recently, computational results have shown that these oxide materials are effective because of their widened electrochemical windows and excellent chemical stability against oxide cathodes compared with those of SSEs.[77,81,82] Summarizing insights drawn from experimental and computational studies, an ideal cathode coating material should exhibit the following properties:

1. A wide electrochemical window that spans the cathode operating voltage and overlaps with the electrochemical window of the electrolyte (electrochemical stability)
2. Limited chemical reactivity with both the electrolyte and the cathode (chemical stability)
3. Reasonable lithium-ion mobility
4. Low electronic conductivity (when paired with electrolytes that are unstable at high voltage)

Whereas the experimental approach to finding new coating materials is time-consuming and low throughput, computational evaluation of potential coatings based on properties 1–4 can be more efficient. Using a computational approach developed in the previous works[160,198,199] to predict the electrochemical stability and the chemical stability of different interface systems, Zhu et al. proposed several new oxides as potential cathode coatings that are chemically similar to the aforementioned oxide coatings, e.g., Li_4TiO_4, Li_2TiO_3, Li_8SiO_6, Li_4SiO_4, Li_5TaO_5, and Li_3TaO_4.[77] In a similar spirit, Aykol et al. performed high-throughput screening of cathode coatings for Li-ion batteries using liquid electrolytes by considering their thermodynamic stability, electrochemical stability, and HF reactivity.[200] For SSBs, it is also desirable to consider the chemical compatibility of the coating with both the cathode and the SSE. In addition, the ionic conductivity, an important criterion for coating performance,[123,201] has often been neglected in the computational search for new coatings, presumably because of the high computational cost of ion conductivity predictions with ab initio techniques and the difficulty in integrating them with a high-throughput environment.[202,203]

In this chapter, we conducted a high-throughput search for suitable materials for cathode coatings spanning a very wide range of chemistries. We systematically considered the following aspects of these coating compounds: phase stability, electrochemical stability, chemical stability (with both cathodes and SSEs), and ionic and electronic conductivity. We demonstrated that polyanionic oxide compounds offer the best combination of excellent electrochemical stability and chemical stability without sacrificing the ionic conductivity. The highly covalent bonds between M and oxygen in the many MO_x (M = non-metal elements) polyhedral units lowers the energy of the oxygen orbitals, thereby protecting them from oxidation. This effect increases the oxidation stability while also decreasing the chemical reactivity of the polyanionic compounds. Among the polyanionic oxide compounds identified in the high-throughput screening, we specifically highlighted three compounds LiH_2PO_4, $LiTi_2(PO_4)_3$, and $LiPO_3$ as cathode coatings that show great potential for improved performance relative to that of state-of-the-art coatings.

3.2 Results

We performed sequential high-throughput screening for coating materials following the flowchart presented in Figure 3.1. The database used in this study is an internal database of DFT-computed bulk energies of compounds with crystal structures obtained from the ICSD database[156] as well as those generated by applying data-mined chemical substitutions.[204] This database contains both energetic information, such as the formation energy, and electronic data, such as the Kohn–Sham band gap. As a prerequisite for achieving reasonable Li ionic conductivity, we only considered the 104,082 Li-containing materials in the dataset as potential coating candidates.

3.2.1 Initial screening

We began the screening by excluding compounds containing radioactive elements. In addition, cathode coatings designed to stabilize SSEs with low oxidation limits must be electronically insulating (Property 4); otherwise, the SSE at the SSE/coating interface will still subject to the high voltage of the cathode. We used Kohn–Sham band gaps (E_g) determined from DFT calculations as a first-order screening criterion for electronic conductivity for materials. While a low band gap almost certainly leads to some electronic conductivity,[205] even wide-band-gap materials can exhibit electronic transport when point defects in the material create carriers in the valence or conduction bands.[206] As such, electronic conductivity may depend on synthesis/processing conditions and the susceptibility of the compound to create carrier-generating point defects.[206] While the energy of these defects depends to some extent on the band gap, as it contains the energy to create an electron (hole) in the conduction (valence) band, it is certainly possible that wide-band-gap materials become electronically active under certain synthesis and processing conditions. Such an analysis would require calculations of all possible point defects as a function of Fermi level, as is sometimes done for oxides and chalcogenides,[206,207] but would be fairly expensive in this high-throughput screening, and be further complicated by the amorphous nature of some coating materials.[119]

Thus, to the first-order approximation, materials that are potentially electronically conducting such as metals and alloys were also excluded by limiting the Kohn–Sham band gap to be larger than 0.5 eV. The more than 62,000 compounds that meet these initial screening criteria were then evaluated for their phase stability.

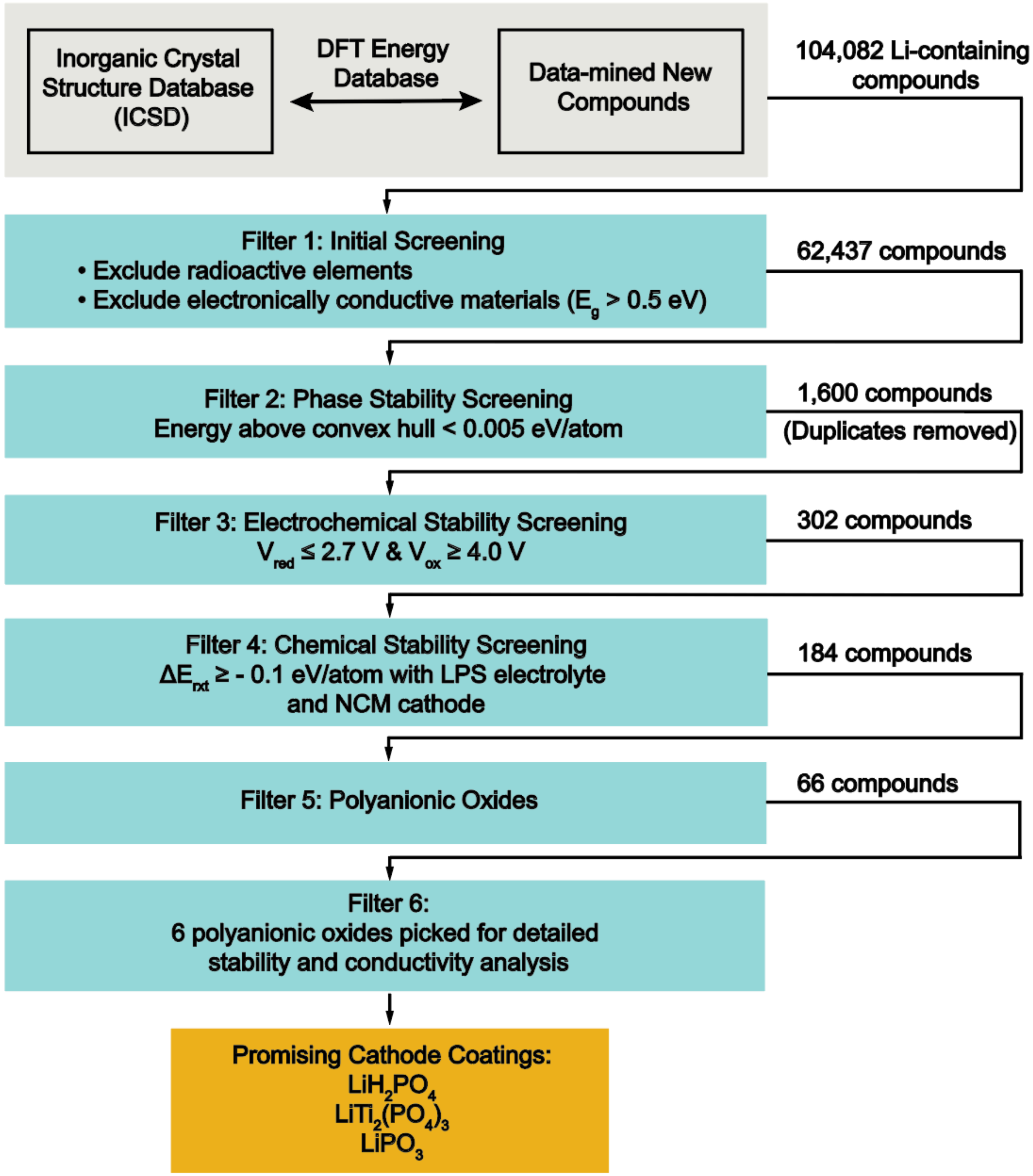

Figure 3.1 Flowchart describing the computational screening of cathode coating materials. Following the initial screening, phase stability, electrochemical stability, and chemical stability were used as sequential filters for the high-throughput screening. E_g is the DFT-calculated Kohn–Sham band gap; V_{red} and V_{ox} are the reduction and oxidation limits of the electrochemical stability window in V vs. Li metal, respectively; ΔE_{rxt} is the reaction energy of the material with the cathode or electrolyte in eV/atom; LPS denotes the SSE material Li_3PS_4; and NCM denotes the fully lithiated cathode material $LiNi_{1/3}Co_{1/3}Mn_{1/3}O_2$.

3.2.2 Phase stability screening

A good cathode coating is expected to maintain its structural and chemical integrity during the shelf life and the operation of the battery. The phase stability of a material determines both its long-term stability and synthesizability. In this study, we only considered Li-containing materials that are thermodynamically stable (or stable within the DFT or temperature error) against decomposition into other phases. We evaluated the phase stability of a material by building the energy convex hull in the chemical space that includes this material and calculating its energy above this hull (see section 3.5).[81,200] Only materials whose energies are < 0.005 eV/atom above the convex hull or exactly on the hull were considered thermodynamically stable (or stable within DFT or temperature error). This phase stability filter returned 1,600 compounds with unique compositions for further consideration of the electrochemical stability.

To better understand the composition–property relationship, we categorized materials according to their anion chemistry: fluorides, chlorides, oxyfluorides, oxides, and others (sulfides, nitrides, bromides, iodides, phosphides, etc.) We additionally divided the oxides into polyanionic oxides and non-polyanionic oxides. In this study, polyanionic oxides refer to oxides with nonmetal-oxygen cluster anion groups, including PO_x^{y-}, SO_4^{2-}, BO_x^{y-}, CO_3^{2-}, AsO_4^{3-}, SeO_4^{2-}, NO_3^{-}, SiO_3^{2-}, ClO_x^{y-}, BrO_3^{-}, and IO_x^{y-}. Using this definition, the conventional ternary metal oxide coatings (e.g., $LiAlO_2$, $LiTaO_3$, $LiNbO_3$, $Li_4Ti_5O_{12}$, and Li_2ZrO_3) belong to the non-polyanionic oxides category. Figure 3.2 and Table 3.1 summarize the numbers and percentages of compounds for each category of materials that pass the phase stability filter (filter 2), electrochemical stability filter (filter 3), and chemical stability filter (filter 4). As observed in Table 3.1, more than 50% of the 1,600 phase stable materials that pass filter 2 are oxides, implying that oxides have a rich chemical space for property optimization. Note that within the oxide category, there are approximately equal numbers of non-polyanionic oxides (397) and polyanionic oxides (411).

3.2.3 Electrochemical stability screening

The lithium electrochemical stability window of a material is the voltage range (vs. Li metal) in which the material is stable against decomposition by either lithium consumption or release. Specifically, the oxidation and reduction limits of the stability window are defined as the voltage limits at which the material begins to be oxidized via Li extraction or reduced via Li insertion, respectively. Thermodynamically, the voltages are obtained from the limits of the lithium chemical potential that keeps the grand potential of the material on the convex energy hull.[81,89,199] For example, at the lower chemical potential value of this range (corresponding to higher voltage), the compound will decompose into one or more phases with an overall reduced Li content. Since a significant driving force may be required to form new phases from the compound, some kinetic stabilization beyond the predicted voltage limits may be expected. For example, the overpotential for the oxidation of LLZO has been shown to be more than 1 V.[104] The methodology for the electrochemical stability window calculation is described in section 3.5.

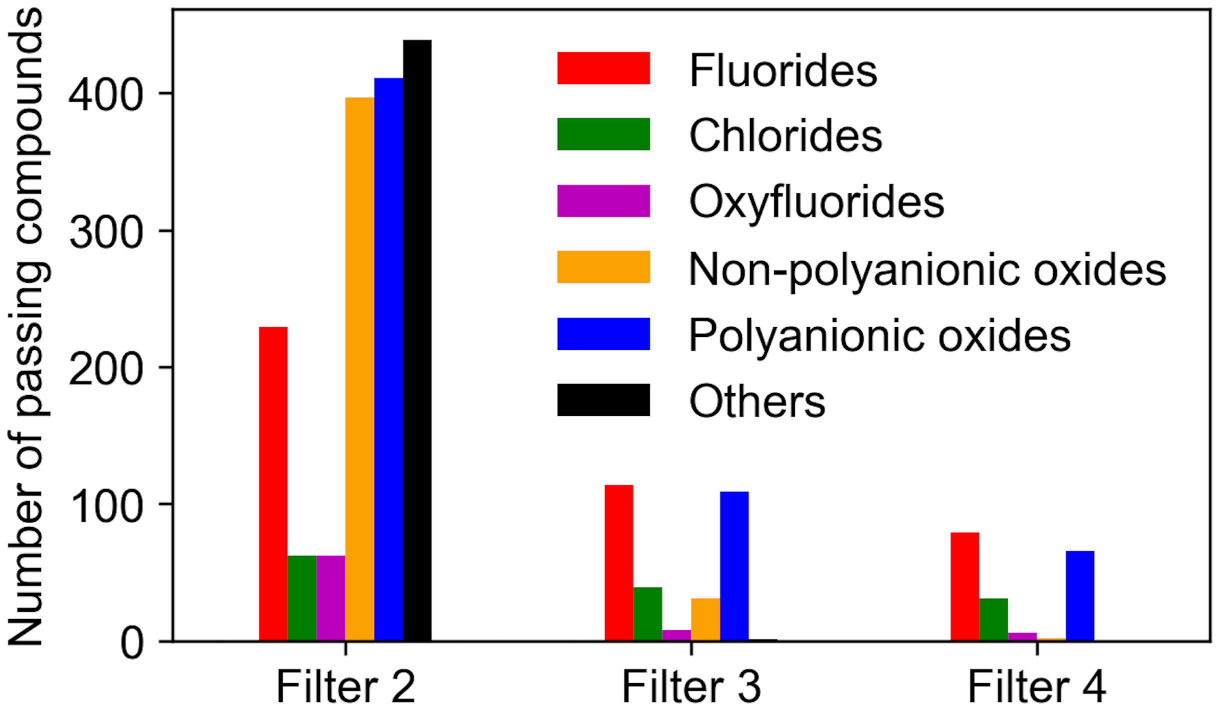

Figure 3.2 Histogram of numbers of compounds for each category that pass each filter in the high-throughput screening.
Red: fluorides; green: chlorides; purple: oxyfluorides; orange: non-polyanionic oxides; blue: polyanionic oxides; black: others. Filter 2: phase stability screening; Filter 3: electrochemical stability screening; Filter 4: chemical stability screening.

Table 3.1 Numbers and percentages of compounds for each category that pass each filter in high-throughput screening

Filter	**Fluorides**	**Chlorides**	**Oxyfluorides**	**Non-polyanionic oxides**	**Polyanionic oxides**	**Others**	**Total**
Filter 2[a]	229 (14.3%)	62 (3.9%)	62 (3.9%)	397 (24.8%)	411 (25.7%)	439 (27.4%)	1600
Filter 3[b]	114 (37.7%)	39 (12.9%)	8 (2.6%)	31 (10.3%)	109 (36.1%)	1 (0.3%)	302
Filter 4[c]	79 (42.9%)	31 (16.8%)	6 (3.3%)	2 (1.1%)	66 (35.9%)	0 (0.0%)	184

[a]Phase stability screening, [b]Electrochemical stability screening, [c]Chemical stability screening

The operating voltage of modern cathode materials can vary widely from 2.5 to 4.5 V during charge and discharge cycles. For a cathode coating to be effective, the oxidation limits should be high enough for it to be stable at the top of charge. To allow for some potential kinetic stabilization, we set the criterion for the oxidation limit to be 4.0 V. For the reduction limit, the coating can only be stable with the electrolyte if its electrochemical window overlaps with that of the electrolyte to ensure that there is no driving force for Li transfer between the coating and the electrolyte. Given that the calculated oxidation limits of sulfide electrolytes are typically in the range of 2.2–2.7 V,[81] we set the reduction limit of coatings to be 2.7 V. Therefore, the final stability window criterion used for the electrochemical stability screening was an oxidation limit of $V_{ox} \geq 4.0$ V and a reduction limit of $V_{red} \leq 2.7$ V.

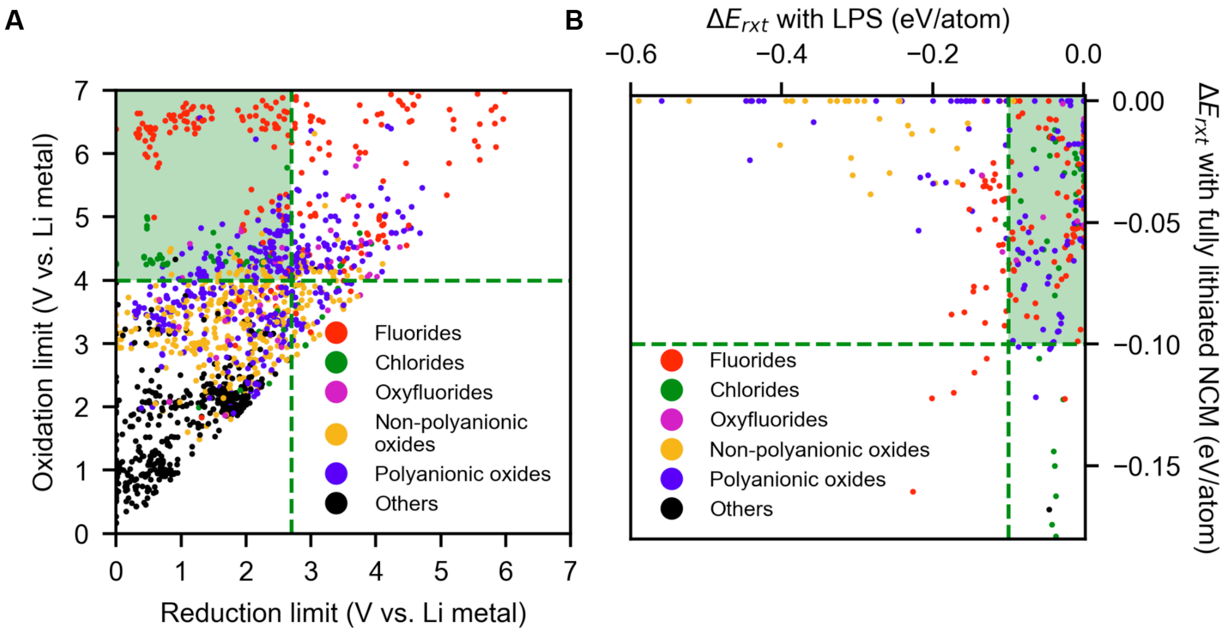

Figure 3.3 Electrochemical and chemical stability screening results.
Each material is represented by a dot in the graphs. Red: fluorides; green: chlorides; purple: oxyfluorides; orange: non-polyanionic oxides; blue: polyanionic oxides; black: others. (A) Electrochemical stability windows of 1,600 phase-stable materials. (B) Chemical reaction energy ΔE_{rxt} with Li_3PS_4 (LPS) and fully lithiated $LiNi_{1/3}Co_{1/3}Mn_{1/3}O_2$ (NCM) for the 302 screened materials enclosed in the green box in Figure 3.3A.

Figure 3.3A plots the electrochemical stability windows of all 1,600 compounds that pass the phase stability screening. As noted by Richards et al., the oxidation limit of a material is primarily determined by the anion chemistry.[81] Separation of the oxidation limits of materials with different anions is also evident in Figure 3.3A. Fluorides typically have the highest oxidation limits, followed by chlorides, polyanionic oxides, and non-polyanionic oxides. Compounds in the "Others" category generally have the lowest oxidation limits, below 2.5 V. In Figure 3.3A, the horizontal dashed line at 4.0 V denotes the oxidation limit minimum in the electrochemical stability window criterion, and the vertical dashed line at 2.7 V denotes the reduction limit maximum. The region shaded in green in the top left corner therefore represents the stability window of interest, which contains 302 compounds. Figure 3.2 and Table 3.1 show that almost all the compounds in the "Others" category are eliminated during this round of screening because of their low oxidation limits, consistent with previously findings for sulfides, nitrides, and phosphides.[81] Table 3.1 also shows that approximately half of the phase-stable fluorides and chlorides meet the electrochemical criterion, which is the highest percentage among all the chemistries. Notably, after this round of screening, the polyanionic oxides (109) outnumber the non-polyanionic oxides (31) because of their higher pass rates (26.5% for polyanionic oxides vs. 7.8% for non-polyanionic oxides). It is worth noting that several polyanionic oxide coatings that have been used in cells with liquid electrolyte have oxidation limits exceeding our threshold (e.g., $LiCoPO_4$ (4.19 eV)[208,209], $LiNiPO_4$ (4.22 eV)[210],

$LiTi_2(PO_4)_3$ (4.59 eV)[211]), explaining their reported good performance. The pass rate is 12.9% for oxyfluorides which is in between of the numbers for polyanionic oxides and non-polyanionic oxides. This is because in these compounds with mixed anions, the oxidation limit is determined by the anion with the lowest oxidation limit. Since oxides have lower oxidation limits than those of fluorides, it is expected that the oxidation limits and pass rate of oxyfluorides are similar to those of oxides.

3.2.4 Chemical stability screening

Next, we considered the chemical stability requirements for cathode coatings. In the absence of a coating, chemical reactions at the interface between the cathode and the SSE have been observed to occur and are accompanied by the interdiffusion of atoms and the formation of ionically insulating phases.[76,108] When a cathode is coated, the cathode/SSE interface is replaced by two new interfaces: the cathode/coating interface and the coating/SSE interface. For a coating to function as designed, it should not only act as a physical barrier that prevents interdiffusion between the SSE and the cathode but should also provide two new interfaces that are more stable than the original cathode/SSE interface. For each interface system, we determined the chemical mixing reaction with the most negative reaction energy (ΔE_{rxt}) using DFT-computed energies of the reactants and possible products. The magnitude $|\Delta E_{rxt}|$ was used as an indicator of the chemical reactivity of that interface, with a high $|\Delta E_{rxt}|$ indicating a reactive interfacial system. The methodology used for the chemical mixing energy calculation is described in section 3.5.[81]

As an example, Figure 3.3B plots the reaction energy of possible coating materials with Li_3PS_4 (LPS) as the SSE and the reaction energy with fully lithiated $LiNi_{1/3}Co_{1/3}Mn_{1/3}O_2$ (NCM) as the cathode for all 302 materials that pass the electrochemical stability filter (filter 3). This plot is relevant for a coating that would be used to protect LPS from NCM. As observed in Figure 3.3B, all of the non-polyanionic oxides exhibit limited reactivity ($|\Delta E_{rxt}| < 50$ meV/atom or 4.8 kJ/mol) with NCM; however, over three quarters of them exhibit large reactivity ($|\Delta E_{rxt}| \geq 200$ meV/atom or 19.3 kJ/mol) with LPS. More than 60% of the polyanionic oxides, however, exhibit limited reactivity ($|\Delta E_{rxt}| \leq 100$ meV/atom or 9.6 kJ/mol) with both LPS and NCM. To identify cathode coatings that are chemically compatible with both the electrolyte and the cathode, we set the criterion for chemical reactivity (defined as $|\Delta E_{rxt}|$) of the material to be smaller than 100 meV/atom with both LPS and fully lithiated NCM. This reactivity criterion was used to define the green shaded region in Figure 3.3B. This region contains 184 compounds, 106 of which were obtained from the ICSD database. We provide their compositions, electrochemical windows, and reactivity (with NCM and LPS) in Table 3.S1 for the reader's reference. In Table 3.1, we see the even stronger preference for polyanionic oxides over non-polyanionic oxides than that observed in the electrochemical stability screening round. Concretely, the pass rates are 60.6% for polyanionic oxides vs. 6.5% for non-polyanionic oxides. After this round of screening, only two non-polyanionic oxides remains. Interestingly, $LiCoPO_4$ and $LiNiPO_4$ coatings used in cells with organic liquid electrolytes were filtered out because of their high reactivity (~150 meV/atom) with LPS to form transition metal sulfides and lithium phosphates, indicating that they may not be suitable for use in SSBs with sulfide electrolytes.

3.2.5 Down-selection to polyanionic oxides

Fluorides and chlorides are two classes of materials that exhibit exceptional electrochemical stability and chemical stability. As observed in Table 3.1, together they account for nearly 60% of the 184 compounds passing filter 4. In particular, LiF, LiCl, $LiRbCl_2$, $LiCsCl_2$, and $LiRb_2Cl_3$ have zero reactivity with both fully lithiated NCM and LPS. However, the halides have less been explored than polyanionic oxides in terms of ionic conductivity. Except for one recent report on Li_3YCl_6 with $\sigma_{RT} = \sim 10^{-4}$ S/cm at room temperature,[47] there have only been limited reports on lithium chlorides, with the best room-temperature ionic conductivity reported being approximately 10^{-6} S/cm,[212–214] and no inorganic fluorides as Li ion conductors were reported to the best of our knowledge. In comparison, numerous polyanionic oxides have been reported to exhibit reasonably high room-temperature ionic conductivity such as NASICON-type phosphates ($\sigma_{RT} = \sim 10^{-4}$ S/cm),[146,215–217] LISICON-type phosphates ($\sigma_{RT} = \sim 10^{-4}$ S/cm),[218] and LiPON ($\sigma_{RT} = \sim 10^{-6}$ S/cm).[10,219] We decided to focus on polyanionic oxides for further analysis given that 1) some of them are known good Li ion conductors, and 2) there are well-known methods to synthesize and apply them as coatings. However, we want to emphasize that halides also have the potential to exhibit comparable stability and ionic conductivity as shown recently by Li_3YCl_6.[47] Table 3.S1 provides a thorough list of the coating candidates that pass the chemical stability filter that includes a wide range of chemistries, including fluorides and chlorides.

Even though we greatly narrowed down the compounds of interest to 66 polyanionic oxides, it remains computationally expensive to study all of these candidates using ab initio techniques, especially for dynamic properties such as the lithium ion mobility. We therefore selected six representative compounds from the 66 polyanionic oxides to assess their potential as cathode coatings in detail. These six compounds included the ortho-phosphates LiH_2PO_4 and $LiTi_2(PO_4)_3$, meta-phosphates $LiPO_3$, $LiLa(PO_3)_4$, and $LiCs(PO_3)_2$, and borate $LiBa(B_3O_5)_3$. These candidates are among the polyanionic oxides with the highest oxidation limits (≥ 4.5 V) in Table 3.S1.

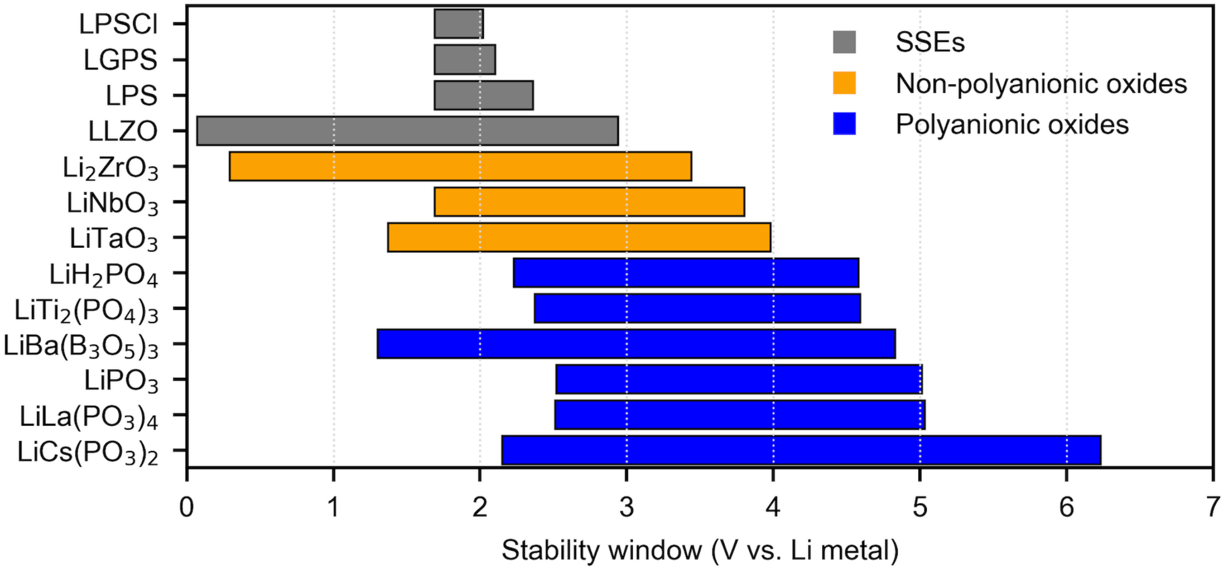

Figure 3.4 Electrochemical stability windows of common thiophosphate and oxide solid-state electrolytes (grey), non-polyanionic oxide coatings (orange), and polyanionic oxides (blue).

3.2.6 Stability of six polyanionic oxides

The electrochemical stability windows for the six polyanionic oxides are plotted as a bar graph in Figure 3.4. For comparison, we also plotted the electrochemical stability windows of common thiophosphate electrolytes: argyrodite Li_6PS_5Cl (LPSCl), LGPS, the glass ceramic Li_3PS_4 (LPS), and garnet-type LLZO and the ternary non-polyanionic coatings Li_2ZrO_3,[124] $LiNbO_3$,[73] and $LiTaO_3$.[119] Consistent with the poor electrochemical stability of sulfides in general, the three thiophosphates exhibit low oxidation limits < 2.5 V.[84] The oxide LLZO has a wider stability window with an oxidation limit of 2.9 V, which is still too low to be paired with high-voltage cathodes. Indeed, a recent experimental study showed that the apparent oxidation limit of LLZO is approximately 4.0 V,[104] indicating that slow oxidation kinetics may protect the material somewhat above its thermodynamic limit, but not enough to function in battery systems for which the voltage is above 4.0 V. Thus, protection of LLZO at high voltage remains necessary. The three ternary metal oxide coating materials listed in Figure 3.4 exhibit improved oxidation stability (3.4–4.0 V) as compared to both thiophosphate and oxide electrolytes, which explains their previously reported good performance.[73,119–121,124] In comparison, the polyanionic oxides listed in Figure 3.4 offer substantially higher oxidation limits (≥ 4.5 V) than those of non-polyanionic oxide coatings. For example, the ortho-phosphate $LiTi_2(PO_4)_3$ exhibits an oxidation limit of 4.6 V and all three metaphosphates are stable at 5 V or higher, making it possible to pair them with extremely high-voltage cathodes such as $LiNi_{0.5}Mn_{1.5}O_4$ (~4.7 V).[106,107]

To examine the chemical reactivity of the down-selected coatings with cathodes and electrolytes, we use the color-mapped cells representing the reaction energies ΔE_{rxt} in Figure 3.5 for the various interfaces: fully lithiated cathode/coating, fully lithiated cathode/SSE, and SSE/coating. The SSEs and coatings are the same as those in Figure 3.4, and the cathodes evaluated are the commonly used oxide cathodes NCM, $LiCoO_2$ (LCO), $LiMn_2O_4$ (LMO), and $LiFePO_4$ (LFPO). The exact reaction energies and products are listed in Table 3.S2, 3.S4, and 3.S5, respectively. To determine the compatibility of the interfaces involving cathodes at different states of charge, we repeated the procedure for half-lithiated cathodes, and the reaction energies and products for the most favorable reactions are tabulated in Table 3.S3 and 3.S4, respectively.

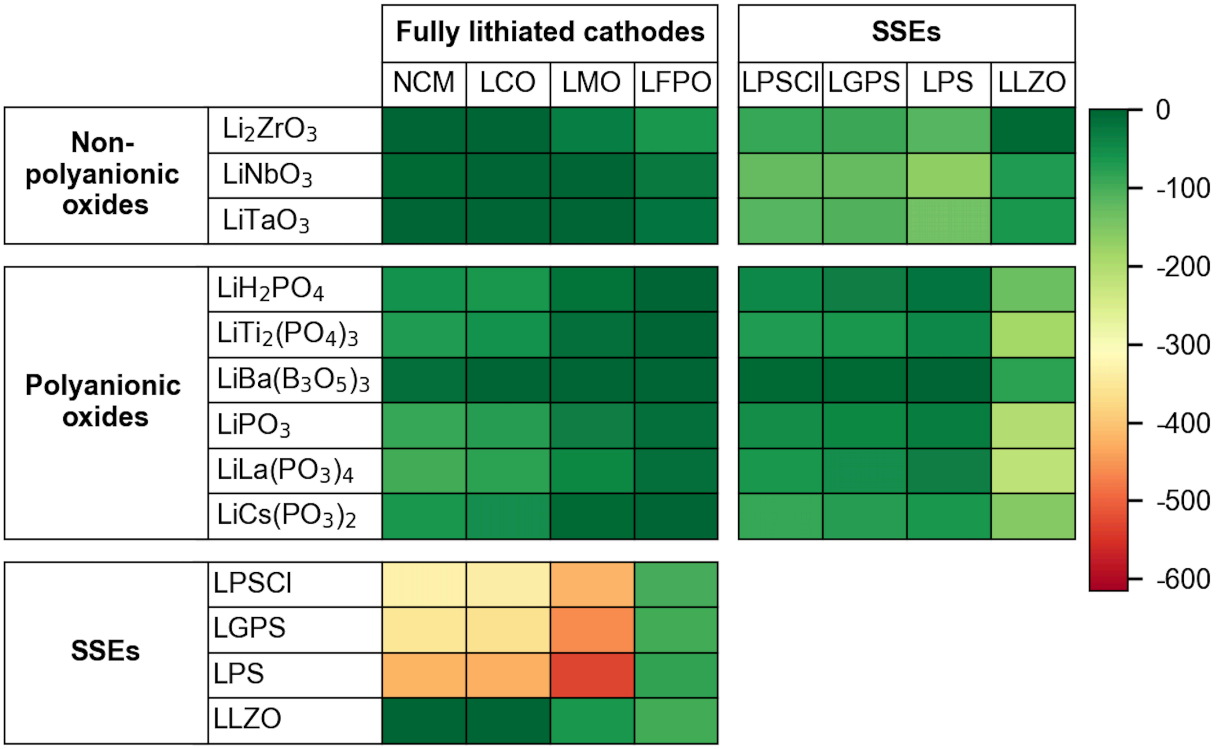

Figure 3.5 Reaction energies ΔE_{rxt} at fully lithiated cathode/SSE, fully lithiated cathode/coating, and coating/SSE interfaces in meV/atom.
The specific values for ΔE_{rxt} are provided in Table 3.S2. Each cell is mapped to a color from green to red according to the color bar on the right, with the dark green color denoting low chemical reactivity and the dark red color denoting high chemical reactivity.

As observed in Figure 3.5, all the thiophosphate electrolytes (LPSCl, LGPS, LPS) react strongly with all the cathodes except for LFPO, as indicated by the red colors and very negative reaction energies in Table 3.S2. Specifically, the LPS/NCM interface of interest has a reactivity $|\Delta E_{rxt}|$ as high as 422 meV/atom (40.7 kJ/mol). This high reactivity is even more pronounced at the half-lithiated cathode/SSE interface (Table 3.S3). As noted in previous studies,[81,220] the high reactivity between the oxide cathode and thiophosphates originates in part from the strong tendency to exchange O and S between the SSE and cathode and form PO_4^{3-} groups (as in Li_3PO_4) and transition-metal sulfides, and the formation of P-O_x species was indeed detected experimentally at the NCM/LPS interface.[83] The exchange of O-S is energetically favorable because the bond dissociation energy is much larger for a P-O bond (597 kJ/mol) than for a P-S bond (346 kJ/mol), while the bond dissociation energy difference is small for transition metal-O (e.g., Co-O: 368 kJ/mol) and transition metal-S bonds (e.g., Co-S: 343 kJ/mol).[221] However, in the LFPO cathode, phosphorus is already fully bonded with O atoms, leading to a lower reactivity of LFPO with thiophosphates. Although some modeling results have been used to argue that the reduction of phosphorus to phosphides is kinetically preferred over PO_4^{3-}, this unexpected result requires some experimental confirmation.[220]

The garnet-type oxide electrolyte LLZO has a higher chemical compatibility with oxide cathodes unlike thiophosphate electrolytes. In particular, the reaction energies of LLZO with fully lithiated NCM and $LiCoO_2$ are effectively zero, but reactions between LLZO and half-lithiated cathodes are still thermodynamically favorable during charging (Table 3.S3). Despite the predicted low reactivity at 0 K, chemical reactivity at the $LiCoO_2$/LLZO interface to form La_2CoO_4 has been observed at 973 K.[108] The high temperature reactivity and reduction of Co from 3+ to 2+ can be understood by considering oxygen loss and the associated reduction of the transition metal at high temperature as in the study of LLZO/spinel cathode interface.[99] Also, the migration of larger cations is promoted at elevated temperatures, causing the interdiffusion of Co, La and Zr.[108] Therefore, a thermally stable coating is still needed at the $LiCoO_2$/LLZO interface to suppress the interdiffusion of elements at high temperature during sintering.

Ternary metal oxide coatings and polyanionic coatings generally provide a much more stable interface with oxide cathodes than sulfide electrolytes, as indicated by their small reactivity in Figure 3.5. In fact, some ternary metal oxide coatings have no driving force to react with oxide cathodes in both fully lithiated and half-lithiated states (e.g., $LiTaO_3$/NCM, $LiNbO_3$/LCO). Indeed, $LiNbO_3$-coated $LiCoO_2$ and $LiMn_2O_4$ have been used effectively in SSBs with a sulfide SSE.[73,120] In contrast, phosphates-based coatings are predicted to exhibit higher reactivity with oxide cathodes (except for LFPO) than oxide coatings, which is largely driven by the tendency to form Li_3PO_4 (Table 3.S4). Specifically, meta-phosphates containing the PO_3^- group want to obtain O from oxide cathodes to form the PO_4^{3-} group. Even for the ortho-phosphate $LiTi_2(PO_4)_3$, which already contains the PO_4^{3-} group, it is energetically favorable to give up transition-metal elements and obtain Li from the cathode to form the Li_3PO_4 phase. However, the formation of Li_3PO_4 may not always be detrimental, as it has been used as a cathode coating and thin-film solid electrolyte.[117,222,223] Crystalline Li_3PO_4 possesses a reasonably high oxidation limit (4.22 V) and chemical stability, as shown in Table 3.S1, and in partially crystalline form its ionic conductivity ($\sigma_{RT} = \sim 10^{-7}$ S/cm) is only slightly lower than that of LiPON.[223] Hence, Li_3PO_4 could function as a passivation layer, restricting further reactivity. Not surprisingly, phosphate oxides are quite stable with LFPO, which can be attributed to their high similarity in P–O bonding. In fact, when phosphates were recently applied for all the components in a solid-state Li-ion battery, improved interfacial stability and cyclability was observed,[224] consistent with our computational results.

The interface between an oxide coating and a thiophosphate SSE behaves similar to an oxide cathode/SSE interface with reactivity that is often larger than 100 meV/atom, driven by the formation of Li_3PO_4 and transition metal sulfides. In contrast, many polyanionic coatings provide greatly improved compatibility with thiophosphate electrolytes ($|\Delta E_{rxt}| < 100$ meV/atom), a result we observed in the high-throughput chemical reactivity screening. Interestingly, the trend is reversed at the coating/LLZO interface. Oxide coatings show low reactivity with LLZO, while the phosphates are predicted to have a non-trivial ($|\Delta E_{rxt}| > 100$ meV/atom) reactivity with LLZO, driven by the formation of Li_3PO_4. Some polyanionic oxides other than phosphates such as $LiBa(B_3O_5)_3$ show extremely high chemical compatibility with both cathodes and thiophosphate electrolytes, indicating that all the interfaces in the cathode/coating/SSE configuration can remain intact. Other lithium borates in Table 3.S1 such as $LiSr(B_3O_5)_3$, $LiH_2B_5O_9$, $LiCs(B_3O_5)_2$, LiB_3O_5, $Li_3B_7O_{12}$, $Li_2Al(BO_2)_5$ and $Li_4B_7O_{12}Cl$ exhibit similar low chemical reactivity. Their excellent chemical stability in addition to their good electrochemical stability make borates very promising cathode coatings. There are other polyanionic compounds with zero chemical reactivity with NCM and LPS: $LiAlSiO_4$, and Li_3PO_4, although their oxidation limits (4.09 and 4.22 V) are slightly lower than that of $LiBa(B_3O_5)_3$.

3.2.7 Ionic and electronic conductivity considerations

The ionic conductivity of a coating has been less emphasized than its stability in previous studies. However, Sakuda et al. studied the electrochemical performance of SSBs using SiO_2-coated and Li_2O–SiO_2-coated cathodes and attributed the better rate capacity of the Li_2O–SiO_2-coated cathode to the higher lithium ion conductivity of its coating.[201] Also, a recent report has shown that solid-state batteries with Li_3BO_3-Li_2CO_3 (LBCO) cathode coating exhibit better cell performance than with Li_3BO_3 (LBO) coating, which is explained by the lithium ionic conductivity of LBCO which is two orders of magnitude higher than for LBO.[123] To evaluate and understand the ionic conductivity of the polyanionic coating candidate, we performed NEB calculations for the single Li vacancy migration barrier. The interstitial mechanism was not considered as interstitial Li atoms are not likely to survive at high voltage. We also did not include the vacancy formation energy in the migration barrier, as we expect that a coating layer of nanometer thickness prepared using common coating methods would be highly defective and contain intrinsic vacancies. In each structure, there are multiple possible vacancy hopping pathways. The lowest migration barrier, E_m, for a pathway that percolates the supercell is provided in the third column in Table 3.2, with the migration pathways shown in Figure 3.S1. The NEB migration energies for individual hopping events are also listed in Table 3.S6. As a reference, the migration for a reported ternary metal oxide coating material, Li_2ZrO_3, was also calculated. Li_2ZrO_3 has a calculated migration barrier of 0.48 eV for Li vacancy migration, which is smaller than the 0.56 eV found for LiPON.[10,219] Among the six polyanionic oxides considered in the current study, the calculated migration barriers in LiH_2PO_4 (0.33 eV), $LiTi_2(PO_4)$ (0.42 eV), and $LiPO_3$ (0.40 eV) are similar to or less than those of LiPON and Li_2ZrO_3, indicating that fairly good ionic conductivity can be expected in these materials. However, the compounds with the highest oxidation limits have vacancy migration barriers larger than 1 eV, such as 1.39 eV for $LiLa(PO_3)_4$ and 1.27 eV for $LiCs(PO_3)_2$, implying low room-temperature Li ion conductivity. We also list the experimental activation energies (E_a) and ionic conductivity for Li conduction in Table 3.2 for reference. As observed in Table 3.2, the calculated migration barriers for Li_2ZrO_3, $LiTi_2(PO_4)_3$, and $LiCs(PO_3)_2$ agree fairly well with the experimentally determined activation energy for the same crystal structures.[225–228] In contrast, the experimentally determined activation energy for $LiLa(PO_3)_4$ is 0.92 eV,[229] which is considerably lower than the calculated vacancy migration energy, which may indicate that a different migration mechanism controls the measured conductivity. Although this measured activation energy for $LiLa(PO_3)_4$ is lower than the calculated migration energy it remains prohibitively high for Li ion migration. $LiPO_3$ is experimentally reported to have an activation energy of 1.40 eV,[230] which is 1 eV higher than the calculated migration energy. This large difference may originate from a large vacancy formation energy, a different migration mechanism, or another rate limiting step in experiment. However, the conductivity of $LiPO_3$ has also been shown to be enhanced by four orders of magnitude in its glass form (50 Li_2O–50 P_2O_5), with a reduced activation energy of 0.72 eV.[230] Therefore, LiH_2PO_4, $LiTi_2(PO_4)$, and $LiPO_3$ may exhibit satisfactory ionic conductivity for coating application.

As seen in the crystalline $LiLa(PO_3)_4$ and $LiPO_3$, the calculated migration energies are not always consistent with the experimentally measured values. The mismatch is expected as we made several assumptions in our calculations: 1) the carrier formation energy is not included, 2) a vacancy migration mechanism is assumed, 3) the migration in grain boundaries is not considered. In experiments, the measured activation energies are complicated by the factors that were neglected in the assumptions 1-3 and thus deviate from the predicted values. Additionally, the coating may be amorphous, possibly resulting in a different ionic conductivity and activation energy compared to those in the crystalline form, as is observed in $LiPO_3$. Nonetheless, our predicted migration energies can give guidance on how the compounds may perform in crystalline form.

Table 3.2 Computed Li vacancy migration barrier, electronic band gap and experimental conductivity data for Li_2ZrO_3 and the six polyanionic oxides

Coatings	ICSD #	Calculated migration barrier (eV)	Experimental activation energy (eV)	Experimental ionic conductivity (S/cm)	Kohn–Sham band gap (eV)	Experimental electronic conductivity at R.T. (S/cm)
Li_2ZrO_3	31941	0.48	0.5[225], 0.68[226]	~10^{-4} (598 K)[226]	3.99	--
LiH_2PO_4	100200	0.33	--[a]	--	6.30	--
$LiTi_2(PO_4)_3$	95979	0.42	0.47[227]	~10^{-6} (333 K)[227]	2.26	(~10^{-9})[233]
$LiBa(B_3O_5)_3$	93013	1.96	--	--	6.20	--
$LiPO_3$	51630	0.40	1.40[230]	2.5×10^{-8} (553 K)[230]	5.60	--
$LiLa(PO_3)_4$	416877	1.39	0.92[b,229]	6.35×10^{-8} (553 K)[229]	5.22	--
$LiCs(PO_3)_2$	62514	1.27	1.31[228]	~10^{-8} (573 K)[228]	5.65	--

[a] "--" means no experimental data found in the literature for the ICSD crystal structure. [b] The experimental activation energy for $LiLa(PO_3)_4$ was re-calculated from the Arrhenius plot in ref[229], as the value deduced in the original paper is not consistent with its Arrhenius plot.

In terms of electronic conductivity, we use the Kohn–Sham band gaps determined from DFT calculations as a rough indicator in Table 3.2. This is approximate, but true electronic polaron calculations[231] are extremely time consuming and their quantitative accuracy can be debated. Because the band gap calculated using LDA/GGA is underestimated,[232] we used the calculated band gap values as the lower bounds for the real band gap. As observed in the sixth column in Table 3.2, all the coatings have relatively large band gaps above 2.2 eV, indicating low expected electronic conductivity. As a reference, the calculated band gap for a fully lithiated NCM cathode is 1.5 eV. To improve the electrochemical stability at the coating/SSE interface, the coating must have an electronic conductivity that is at least lower than that of NCM. Thus, from the band gap indicator results, all these coatings should meet this requirement. The experimentally measured electronic conductivity of $LiTi_2(PO_4)$ is approximately 10^{-9} S/cm,[233] which is much lower than that of NCM (10^{-2}–10^{-7} S/cm).[234] This result is consistent with the electronic conductivity assessment based on the DFT-calculated band gap. Therefore, all the coatings listed in Table 3.2 have the potential to have low electronic conductivity and meet Property 4. However, as stated in the Initial Screening, when the coating contains point defects that create carriers in the valence or conduction band[206] or is in amorphous form, both of which are likely to happen during the synthesis and coating processes, it is possible that the actual electronic conductivity of these polyanionic coatings are non-negligible despite their computed wide Kohn-Sham band gaps.

3.3 Discussion

Interface compatibility has been a well-known issue in the development of SSBs. For some SSEs such as LiPON, decomposition at high voltage leads to the formation of an SEI layer through a self-limiting reaction.[235] The phases in these SEI layers typically have extended oxidation stability and also conduct Li ions but prohibit electron transport, passivating the cathode/SSE interface.[81,82] For other SSEs, such as sulfides, the interfacial resistance continues to grow upon cycling, causing rapid capacity fade.[83] Coating these non-passivating systems can be viewed as creating an artificial SEI. The advantage of coating is the control over the thickness and composition of the coating. While a non-artificial SEI layer results from reacting an arbitrary amount of cathode and SSE, and interdiffusion of elements can extend as far as 50 nm from the interface, impeding ion transport through the thick SEI layer.[76] In contrast, a coating layer can have a well-controlled chemistry, composition, and thickness of approximately 1–10 nm.[76,115,121,236]

3.3.1 Strong bonding with O improves coating stability

Polyanionic oxide coatings appear promising due to their generally high oxidation stability and smaller chemical reactivity with thiophosphate solid electrolytes. For example, in the case of phosphates the latter is due to the fact that no O-S exchange occurs between the SSE and the coating as all phosphorus in the coating is already bonded with oxygen. On the other hand, any phosphate in contact with a readily available source of Li (such as a discharged cathode or an SSE) will still have a tendency to react, driven by the very favorable formation of Li_3PO_4.

Table 3.3 Oxidation limits and decomposition products for non-polyanionic oxides and polyanionic oxides with similar cation chemistry

Non-polyanionic oxides	Oxidation limit (V)	Decomposition products at oxidation limit	Polyanionic oxides	Oxidation limit (V)	Decomposition products at oxidation limit
Li_2ZrO_3	3.44	ZrO_2, O_2	$LiZr_2(PO_4)_3$	4.52	$Zr_2P_2O_9$, ZrP_2O_7, O_2
$LiTa_3O_8$	4.09	Ta_2O_5, O_2	$Li_2Ta_2(P_2O_7)_3$	5.44	P_2O_5, $TaPO_5$, O_2
$LiCr_3O_8$	4.26	Cr_5O_{12}, O_2	$LiCrP_2O_7$	4.61	$Cr(PO_3)_3$, $CrPO_4$, O_2

Polyanionic oxides have a higher oxidation limit due to the covalency of oxygen with the nonmetal cation in the polyanion. The breakdown of a coating at the oxidation limit likely starts by extraction of an electron and a Li ion. Because the O^{2-} states are the highest occupied state in these coating oxides, they set the oxidation limit, and electron removal from them leads to the formation of peroxides, superoxides, or possibly even O_2 gas. Strong hybridization (covalency) of these oxygen states with a main group cation pushes them down in energy and effectively protects them from oxidation. This is similar to the understanding of anion oxidation in cathode materials.[237] Table 3.3 demonstrates this effect by comparing the oxidation limits and decomposition products for six non-polyanionic oxides and polyanionic oxides with similar cation chemistry. It can be observed that oxygen anions are oxidized at high voltage to form O_2 gas, similar to the O_2 loss observed at the surface of the cathode upon the first charge.[238,239] Polyanionic oxides, however, exhibit significantly higher oxidation limits than their non-polyanionic oxide counterparts.

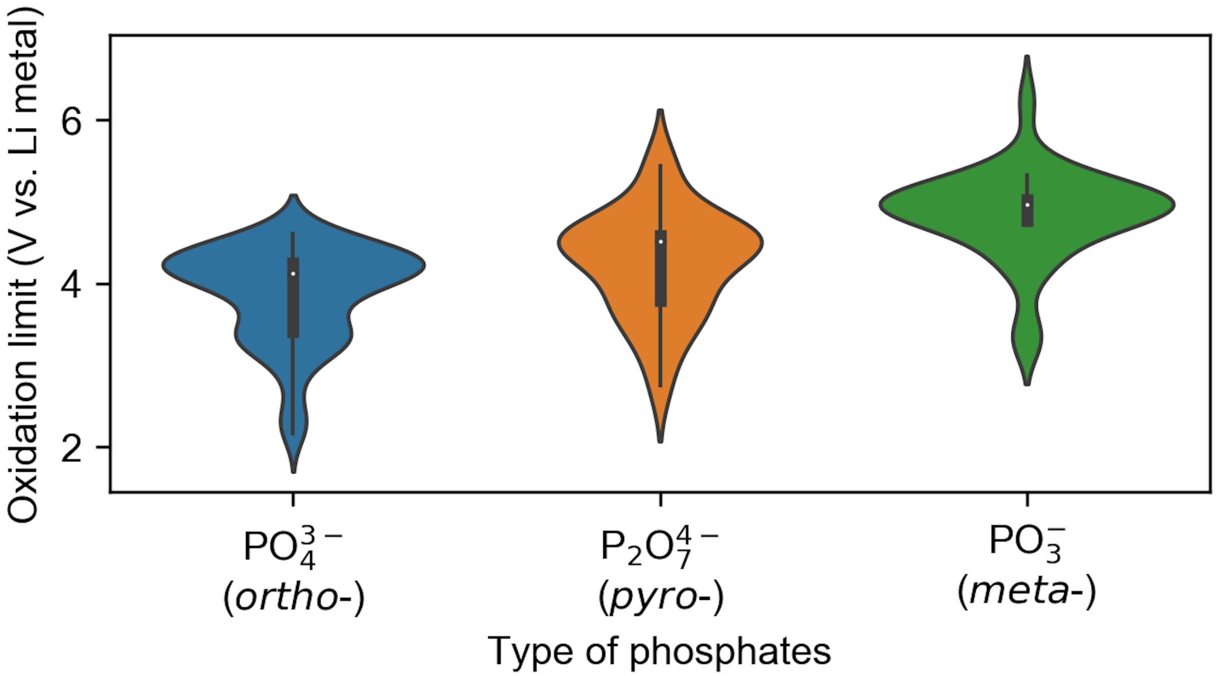

Figure 3.6 Distribution of oxidation limit for ortho-phosphates (PO_4^{3-}), pyro-phosphates ($P_2O_7^{4-}$), and meta-phosphates (PO_3^-) that pass the phase stability filter (filter 2). The violin plot shows the kernel density estimation of the distribution, and the inner box spans the interquartile range (IQR) of the distribution, with the whiskers extending the box by 1.5×IQR on both sides. The white dot inside the box denotes the median.

We further explored the class of phosphate compounds to determine the correlation between the nature of bonding and oxidation limits. Figure 3.6 presents a violin plot of the distribution of the oxidation limit for the 150 phosphates that pass the phase stability filter (filter 2). They can be categorized into ortho-phosphates (31), pyro-phosphates (23), and meta-phosphates (96). In general, the PO_3^- group in the meta-phosphates exhibits the highest oxidation limits, followed by the pyro-phosphates with the $P_2O_7^{4-}$ group. Ortho-phosphates with the PO_4^{3-} group possess the lowest median oxidation limit among all the phosphates. Condensation of the polyhedral units decreases the O/P ratio in the sequence PO_4^{3-}, $P_2O_7^{4-}$, PO_3^- and enhances the hybridization of each O with P, thereby increasing the oxidation limit. This phenomenon is reminiscent of the increase of intercalation voltage in phosphate cathodes with decreasing O/P ratio due to the inductive effect.[240] In fact, both the increase of oxidation limit and the intercalation voltage can be attributed to the enhanced covalency in P-O bonding during phosphate condensation.[241]

This hybridization protection of oxygen can to some extent also be observed in the high oxidation limits of $LiNbO_3$ and $LiTaO_3$ oxide coatings. As 4d and 5d early transition metals, Nb and Ta have less contracted d orbitals than later TM or 3d metals, providing good hybridization for the oxygen states in these materials. While these oxides do not have as high an oxidation limit as some of the phosphate coatings, they have the benefit of very low reactivity with many oxide cathodes as no Li_3PO_4 formation is possible. As such, they may be an excellent compromise when high temperature operations are needed to create the coated cathode materials or to process them in a device. Unfortunately, with thiophosphate SSEs there will be some driving force to for $LiNbO_3$ and $LiTaO_3$ to exchange S and O and produce PO_4 groups. But they are expected to be ideal as a buffer layer between LLZO and oxide cathodes if they can be kinetically stabilized at high voltage (Figure 3.5).

Lithium borates form an interesting, and fairly unexplored alternative to phosphate coatings. The recent application of Li_3BO_3 and Li_3BO_3-Li_2CO_3 as cathode coatings have shown their potential for interfacial protection.[123] Similar to phosphorus, boron provides oxygen with substantial oxidation protection through strong hybridization. Therefore, the borate in our down-selected list has very low reactivity with both cathodes and SSEs likely due to the even stronger B-O bonds than P-O bonds, as indicated by their bond dissociation energies (597 kJ/mol for P-O bond vs. 806 kJ/mol for B-O bond).[221]

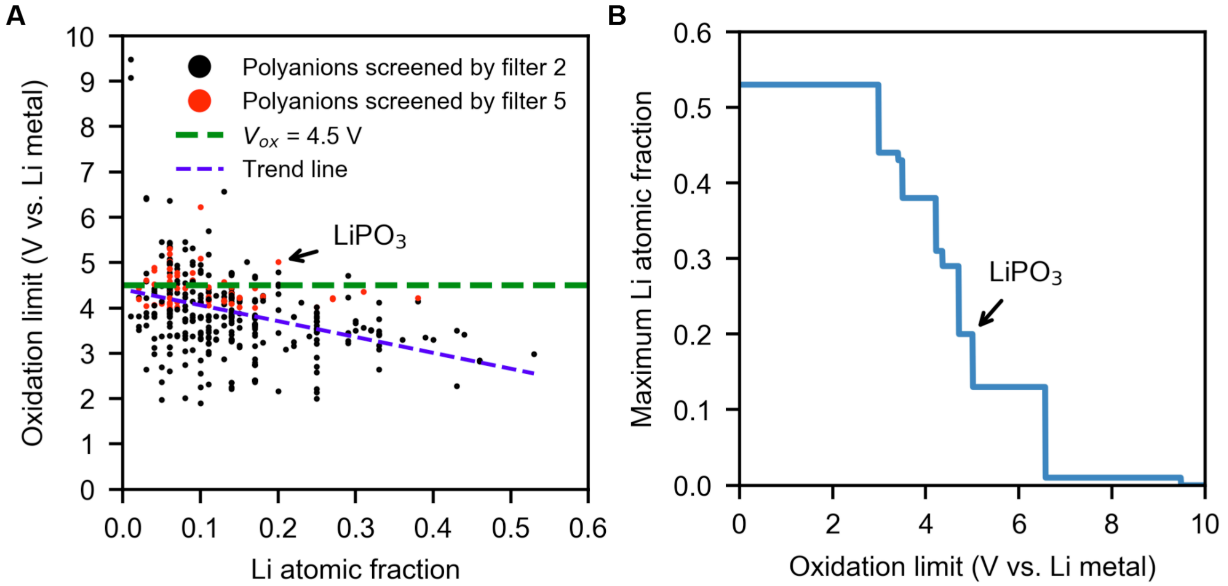

Figure 3.7 Correlation between oxidation limit and Li atomic fraction in polyanionic oxides (A) Oxidation limit vs. Li atomic fraction for the 411 polyanionic oxides (polyanions) that pass the phase stability screening (filter 2). The red dots denote the 66 polyanionic oxides that pass chemical stability screening (filter 5). The green dashed horizontal line marks the oxidation limit = 4.5 V vs. Li metal. The blue dashed line is the linear trend line. (B) Maximum Li atomic fraction vs. oxidation limit for the 411 polyanionic oxides that pass the phase stability screening (filter 2). A point (x, y) in the profile means that all polyanionic oxides with an oxidation limit of x or higher have a maximum Li atomic fraction of y. $LiPO_3$ is marked by the black arrows.

3.3.2 Trade-offs

Despite the high electrochemical stability of polyanionic oxides, we note that there is a trade-off between a high ionic conductivity and a high oxidation limit in these materials. For example, $LiCs(PO_3)_2$ exhibits an extremely high oxidation limit of 6.2 V; however, its high Li ion migration barrier (1.27 eV) may prevent its use as a cathode coating. The same problem also exists for $LiBa(B_3O_5)_3$ and $LiLa(PO_3)_4$, as observed in Table 3.2, and other phosphates with high oxidation limits shown in Table 3.S1, such as $LiGd(PO_3)_4$ (V_{ox} = 5.30 V, E_a = 0.96 eV[242]), $LiK(PO_3)_2$ (V_{ox} =

5.09 V, E_a = 1.89 eV[228]), and $LiDy(PO_3)_4$ (V_{ox} = 4.86 V, E_a = 0.96 eV[243]). The trade-off can be understood by considering the correlation between the oxidation limit and Li content in the material. Figure 3.7A shows the oxidation limits of all 411 Li-containing polyanionic oxides that pass the phase stability filter (filter 2) as a function of their Li atomic fraction (i.e., the ratio of the number of Li atoms to the total number of atoms in the chemical formula). From the blue trend line calculated by the linear fitting of the data points in Figure 3.7A, it can be observed that in general, the oxidation limit decreases with increasing Li fraction for polyanionic oxides. Figure 3.7B is a plot of the maximum Li fraction as a function of oxidation limit for polyanion oxides passing filter 2. For example, the point marked by "$LiPO_3$" in Figure 3.7B has coordinates (5 V, 0.20), meaning that for polyanionic oxides an oxidation limit of 5 V or higher can only be observed in compounds with Li atomic fraction no greater than 0.20. Figure 3.7B shows that the maximum Li fraction decreases drastically at an oxidation limit above 4 V. The low Li fraction in turn indicates a large Li–Li distance and/or low Li–Li coordination number in the material. Both of these factors were observed to be negatively correlated to ionic conductivity in a recent statistical learning study of Li ion conductors.[67] The decreased oxidation limit as the Li content increases may simply be a consequence of the fact that the chemical potential of Li tends to increase as more Li is present in a material. But it is also likely related to the fact that Li removal from a stoichiometry is accompanied by oxygen removal, which in the case of phosphates correlates with the condensation of PO_4^{3-} units. The condensation in turn increases the oxygen covalency, as previously argued. On the other hand, although Figure 3.7B indicates that high oxidation stability can only be achieved in low Li-fraction polyanionic oxides, it is certainly possible that a large overpotential required for O_2 gas evolution (as is for example the case for LLZO[104]) enables higher Li-fraction compounds to be kinetically stabilized at a given voltage. For example, if Li_3PO_4 (V_{ox} = 4.22 V) is kinetically stabilized at 5 V, the limit of Li fraction would increase from 0.20 (in $LiPO_3$) to 0.38 (in Li_3PO_4) at that voltage.

In Figure 3.7A, we also highlight in red the 66 polyanionic oxides that pass the chemical reactivity screening (filter 5), 25 of which have an oxidation limit ≥ 4.5 V (green dashed line). Among the 25 compounds, $LiPO_3$ has the highest Li atomic fraction of 20%. The resulting small Li–Li hopping distance in $LiPO_3$ contributes to the low calculated activation energy for Li vacancy migration of 0.4 eV in crystalline form and 0.72 eV measured in glassy form.[230] Therefore, $LiPO_3$ combines the advantages of excellent high voltage stability (5 V) and a low migration barrier. In fact, the use of $LiPO_3$ on the high-voltage cathode $LiNi_{0.5}Mn_{1.5}O_4$ has been demonstrated to enhance the rate performance and cyclability in a liquid electrolyte cell.[236] For cathodes with a lower cut-off voltage smaller than 4.5 V (e.g., NCM and $LiCoO_2$), the electrochemical stability requirement is less stringent. In this case, we expect that using LiH_2PO_4 or $LiTi_2(PO_4)_3$ with an oxidation limit of 4.6 V as a cathode coating can also result in good cell performance. Indeed, when charged to 4.6 V, $LiTi_2(PO_4)_3$ coating enhanced the capacity retention and rate capacity of a $Li_{1.5}Ni_{0.25}Mn_{0.75}O_{2+\delta}$ cathode in a conventional Li-ion battery.[211]

3.3.3 Challenges with the current coating strategy

Beyond the screening requirements used in this work, there are many other challenges associated with designing an optimal cathode composite. For example, the formation of electronically conductive interphase products at the coating/electrolyte interface would make the coating a mixed conductor and compromise its functionality. At the coating/sulfide interface, there is a driving force for the transition metals to form transition metal sulfides and lithium transition metal sulfides as reaction products. These transition metal sulfides typically have non-negligible electronic conductivity.[244–246] Thus, to further optimize the coating composition, the transition metal content in cathode coating materials should be reduced. In this sense, LiH_2PO_4 and $LiPO_3$ are better choices than $LiTi_2(PO_4)_3$ when paired with sulfide electrolytes. On the other hand, LiH_2PO_4 may potentially produce H_2O and H_2S gas at the interfaces with some oxides and sulfides respectively (Table 3.S4 and 3.S5). However, we expect the amount of these to be small given that the other products are passivating. These volatile products could be removed in the pre-treatment procedures such as annealing, sintering/hot-pressing and vacuum drying. Another side reaction maybe that LiH_2PO_4 exchanges protons with Li ions in $LiCoO_2$ (or NCM), forming H-inserted CoO_2 ($HCoO_2$) and Li_3PO_4 (Table 3.S4). According to the data in Table 3.S2 this exchange reaction is thermodynamically favored with a driving force around 60 meV/atom. The fact that both proton[247] and Li^+ have good mobility in LiH_2PO_4 may facilitate the reaction at room temperature. For spinel $LiMn_2O_4$ cathode, similar exchange reaction to form H-inserted Mn_2O_4 (HMn_2O_4) and Li_3PO_4 has a small driving force (4 meV/atom), while for olivine $LiFePO_4$ cathode the exchange reaction to form H-inserted $FePO_4$ ($HFePO_4$) and Li_3PO_4 is not thermodynamically favorable.

Furthermore, despite the improved performance when applying a cathode coating, there is an inherent paradox of the general cathode coating strategy: a perfect coating that stabilizes the solid electrolyte from oxidation must be electronically isolating; however, the lack of electronic conductivity in the coating would completely prevent active material redox. This phenomenon can be observed in coatings that are too thick and prevent appropriate cycling.[248] This paradox suggests that coatings should either still allow some level of free electron transport or the coatings should be imperfect, allowing the exposed surfaces of the cathode particles to form percolating electronic conduction pathways with the electronically conductive additive and current collector. Figure 3.8 presents a schematic illustration of a coated cathode composite with various interfaces highlighted. Although an imperfect coating would allow contact of the cathode and carbon, it also opens the door for the exposed part of the cathode to contact with the electrolyte, possibly contributing to the observed continuous impedance growth and capacity fade even in cells with a cathode coating.[118,124] Ultimately, to resolve this paradox, an improved morphological design of the different components in the composite cathode might be needed.

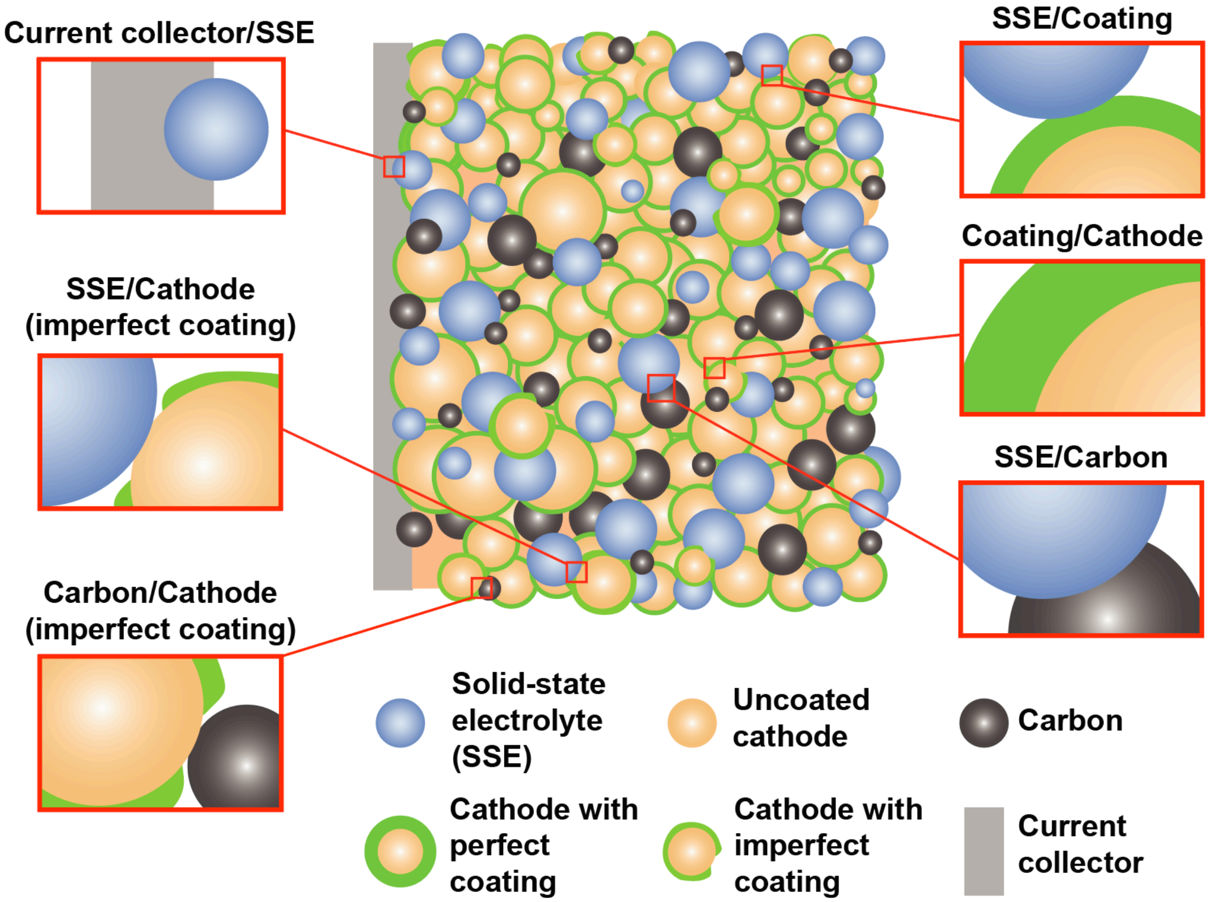

Figure 3.8 Various interfaces in a coated cathode composite.
The general coating strategy only considers the SSE/coating and coating/cathode interfaces, whereas materials decomposition under electrochemical cycling can still occur at other interfaces, i.e., the current collector/SSE, SSE/cathode (imperfect coating), and SSE/carbon interfaces.

Another issue is the oxidation of the solid-state electrolyte at the interfaces with the conductive additive (e.g., carbon) and current collector, where the electrolyte is subject to the full cathode voltage (Figure 3.8). As a result, thiophosphate decomposition is unavoidable when using a strategy of only coating the cathode, and degradation at these interfaces will form ionically insulating "dead space" in electrolyte particles.[84,249] In principle, because neither electron transfer nor Li ion transfer is required at these interfaces, the decomposition of thiophosphates should not immediately affect the low-rate cell performance. However, "dead space" will negatively affect the ionic conductivity of thiophosphate particles and therefore increase the internal resistance of the cell. Thus far, the extent of this "dead space" effect remains unknown.

Application of coatings to a cathode can lead to either an amorphous[119,120] or crystalline form on the cathode surface. Although our studies focused on crystalline coating compounds, we expect the chemical and electrochemical stability to be similar to their amorphous counterparts. As discussed before in the case of $LiPO_3$, the ionic conductivity may however be different. In fact, in some coatings such as $LiNbO_3$, amorphous coatings exhibit higher ionic conductivity than their crystalline counterparts.[250] We note that both the six polyanionic oxides considered in the current study and the other polyanionic oxides in Table 3.S1 mostly consist of phosphates and borates, and in these materials, favorable Li ion conduction has been reported for their glass form.[251,252]

3.3.4 Coating selection

From our results, it is clear that the choice of a coating material needs to be carefully tuned to a specific SSE/cathode combination. For example, Li_2ZrO_3 has the best chemical compatibility at the LMO/LLZO interface among all oxides coatings, whereas the lithium borate is the most stable chemistry for cathode/thiophosphate interfaces (Figure 3.5). It should also be expected that the choice of coating is dependent on the processing techniques that will be used to create the SSB. For example, if high temperature sintering is required to integrate the SSE and cathode particles,[41] then the chemical stability at cathode/coating and SSE/coating may be an overriding concern as interdiffusion of elements is accelerated at elevated temperature.[108,160] If batteries are cold-formed (e.g. by pressing) or mild thermal treatment, then electrochemical stability and lithium ionic conductivity may be more important issues.[83]

Finally, we make recommendations for coating materials in Figure 3.9 for various cathode/SSE interfaces under different processing conditions (sintering/hot-pressing/cold-pressing). Lithium borates are recommended for all interfaces because many compounds in this category show excellent chemical stability and high oxidation limits as shown in Table 3.S1. Although our NEB result indicates that $LiBa(B_3O_5)_3$ has a high migration barrier for lithium ion conduction, it is possible that other borates with higher Li content exhibit reasonable ionic conductivity. Phosphate coatings are recommended to be paired with sulfide SSEs but not with LLZO, because their reactivity with LLZO is high and the fact that processing LLZO incurs high temperature. On the contrary, oxide coatings such as $LiNbO_3$ and $LiTaO_3$ are recommended for pairing with LLZO, with sulfide SSEs they are not optimal because of the high chemical reactivity. As shown before, oxide coatings are featured by their remarkable chemical stability with oxide cathodes, although at high voltage they are electrochemically metastable. Thus, the charging voltage of oxide cathodes may need to be limited when coated with these oxide coatings.

3.4 Conclusions

In summary, we have developed a computational framework to search for cathode coatings in a high-throughput manner. Phase stability, electrochemical stability, chemical reactivity, and ionic and electronic conductivity were used as screening criteria, and the following trends were observed:

1. Because of the high covalency of oxygen, polyanionic oxides have higher oxidation limits and lower reactivity with thiophosphate electrolytes than conventional ternary metal oxide coatings.
2. In general, there is a trade-off between oxidation stability and ionic conductivity in Li-containing polyanionic oxides. Although a high oxidation limit indicates a low Li content in the compound, a high ionic conductivity is correlated to a high Li content.

Six polyanionic oxide coatings were examined in greater detail. Lithium borates such as $LiBa(B_3O_5)_3$ possess excellent electrochemical and chemical stability but may suffer from poor ionic conductivity at low lithium content. Furthermore, three phosphate compounds LiH_2PO_4, $LiTi_2(PO_4)_3$, $LiPO_3$ with good overall characteristics are highlighted for their superior properties as cathode coating materials in solid-state batteries. Based on the results from high-throughput screening and detailed case studies, we make specific recommendations of coating materials for various cathode/SSE interfaces.

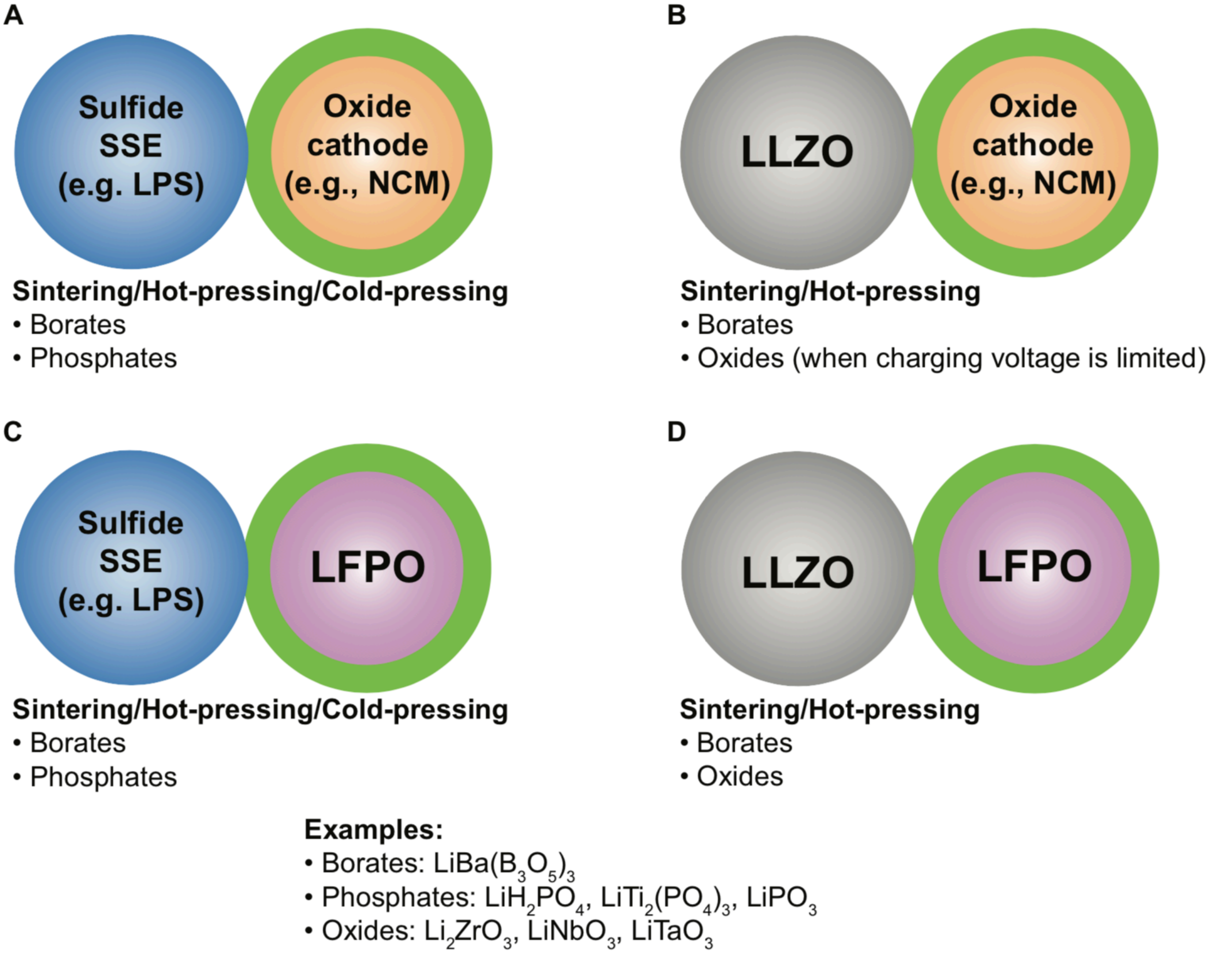

Figure 3.9 Coating recommendations for various cathode/SSE interfaces under different processing conditions.

(A) Oxide cathode/sulfide SSE. (B) Oxide cathode/LLZO. (C) LFPO/sulfide SSE. (D) LFPO/LLZO.

3.5 Methods

First-Principles calculations of bulk energies and band gaps

To calculate the bulk energies and Kohn–Sham band gaps of crystalline materials in the database, we used DFT within the PAW formalism[185], as implemented in the VASP.[253] For the exchange-correlational functional, we employ a mixed scheme of the GGA[187] and GGA with the rotationally invariant Hubbard (+U) correction,[189,254] as described in previous work by Jain et al.[190] An energy cut-off of 520 eV and a k-point grid of at least $500/n_{atom}$ was used for all the calculations. Similar data sets are available online as part of the Materials Project.[159]

Phase stability evaluation

The phase stability of each material was evaluated by computing the lower energy convex hull and corresponding canonical phase diagram at 0 K formed by the ground-state phases in the chemical space defined by all the elements in the material. To construct the convex hull and canonical phase diagram, all known crystalline materials in the chemical space were included and processed using Pymatgen software package.[157] As a result, materials with an energy above the convex hull are expected to decompose into its nearest phases on the convex hull, as this decomposition would lower the total energy of the system. The nearest phases are uniquely defined as the phases that determine the Gibbs triangle (the low-energy facet), which contains the desired composition in the phase diagram. In contrast, materials with an energy exactly on the convex hull are thermodynamically stable against decomposition and therefore pass the phase stability filter. Note that in this work, materials with energies < 0.005 eV/atom above the convex hull also pass the phase stability filter, as they are considered to be stable within DFT or temperature error.

Electrochemical stability window calculation

The calculation of the electrochemical stability window follows the methodology used in the earlier work.[19,81,160] For any lithium chemical potential μ_{Li}, we consider the grand potential Φ of a compound using Equation 1, where c is the composition of the material, $E[c]$ is the enthalpy and $n_{Li}[c]$ is the Li concentration of composition c.

$$\Phi[c, \mu_{Li}] = E[c] - n_{Li}[c]\mu_{Li} \quad (1)$$

For the stability and reaction energy calculations, materials that are metastable (e.g., $Li_{10}GeP_2S_{12}$) are placed exactly on the convex hull to account for the change in free energy when temperature is increased from 0 K to elevated temperature. Similar to using the DFT energy to construct the energy convex hull and canonical phase diagram, one can use the grand potential of materials at given lithium chemical potential μ_{Li} to construct the grand potential convex hull and grand potential phase diagram. The range of μ_{Li}, $[\mu_{ox}, \mu_{red}]$, over which the material is stable in the grand potential phase diagram can be converted into the electrochemical stability window $[V_{red}, V_{ox}]$ using Equation 2 and 3, where μ^0_{Li} is the Li chemical potential of Li metal and e is the elementary charge.

$$V_{red} = (\mu^0_{Li} - \mu_{red})/e \quad (2)$$

$$V_{ox} = (\mu^0_{Li} - \mu_{ox})/e \quad (3)$$

Chemical mixing reaction energy

The calculation of the chemical reaction energy at the solid/solid interfaces (cathode/SSE, cathode/coating, and SSE/coating) followed the methodology used by Richards et al.[81] For two crystalline reactants A and B, the reaction energy ΔE_{rxt} was determined by considering the mixing ratio x that yielded the largest reaction driving force according to Equation 4, where c_a and c_b are the compositions of reactants A and B normalized by their numbers of atoms, respectively; $E_{pd}[c]$ is the energy of the ground-state structure or phase equilibrium at composition c determined from the convex hull. Note that ΔE_{rxt} has the unit of eV/atom or meV/atom as it is normalized by the number of atoms in the reaction.

$$\Delta E_{rxt} = \min_{x\in[0,1]}\{E_{pd}[xc_a + (1-x)c_b] - xE[c_a] - (1-x)E[c_b]\} \quad (4)$$

NEB calculations

To study the Li ion diffusion in the coatings, we performed climbing-image NEB calculations[191,255] for the single-vacancy migration mechanism. For each material, we only considered the crystal structure with the lowest energy in the database. The vacancy was created by removing one Li ion from the pristine structure, and the defect charge was compensated by a uniform background charge to retain the oxidation state for all ions. An energy cutoff of 400 eV was used for all the NEB calculations.

3.6 Supporting information

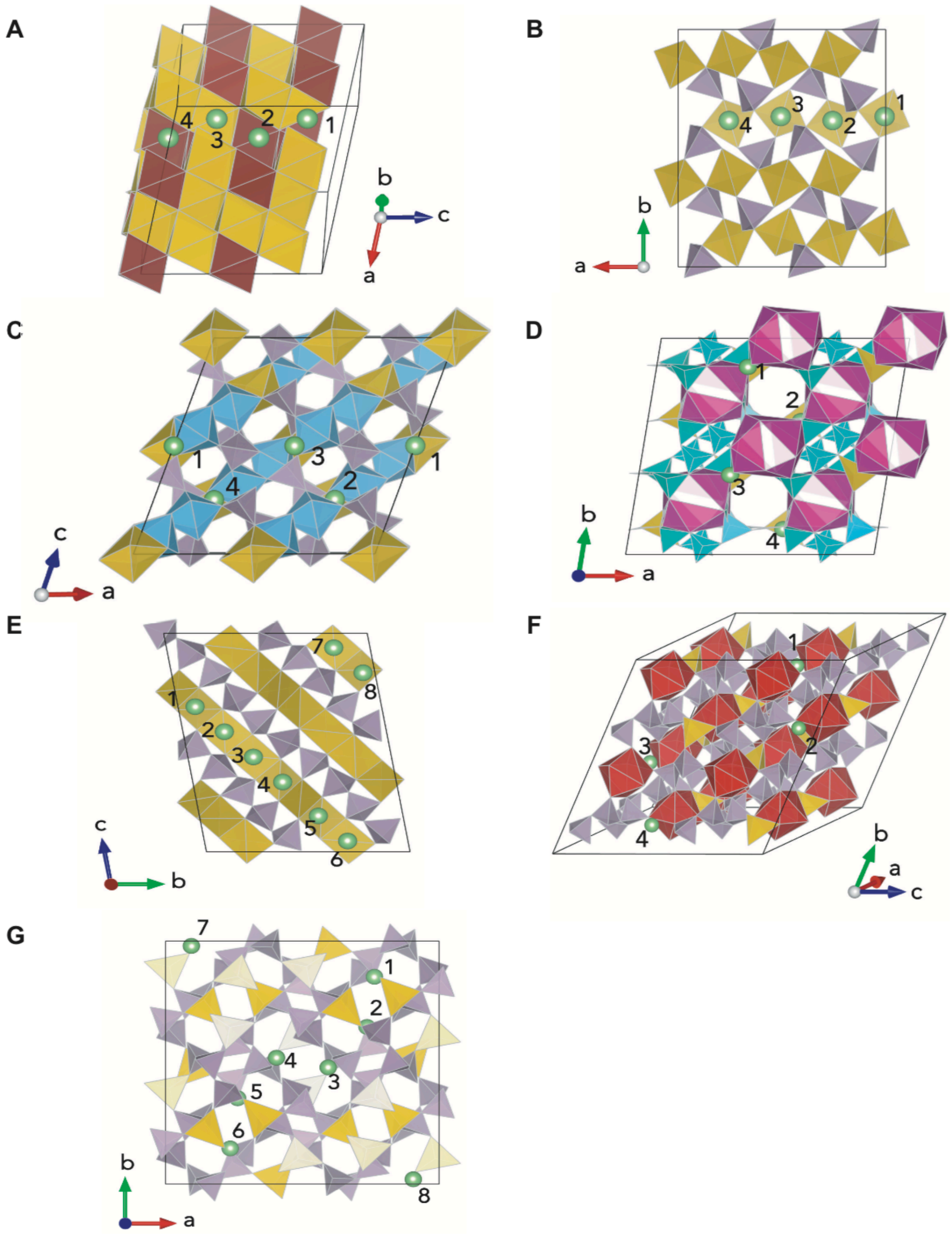

Figure 3.S1 Crystal structures and Li vacancy percolating pathways for Li_2ZrO_3 and the six polyanionic oxides.

Li vacancy positions are labeled by numbers. Green balls: Li vacancies; yellow tetrahedrons: LiO_4; brown octahedrons: ZrO_6; purple tetrahedrons: PO_4; blue octahedrons: TiO_6; pink polyhedrons: BaO_{12}; cyan triangles and tetrahedrons: BO_3 and BO_4; red polyhedrons: LaO_8; CsO_8 polyhedrons are not shown for clarity. (A) Li_2ZrO_3 (1 → 2 → 3 → 4 → 1). (B) LiH_2PO_4 (1 → 2 → 3 → 4 → 1). (C) $LiTi_2(PO_4)_3$ (1 → 2 → 3 → 4 → 1). (D) $LiBa(B_3O_5)_3$ (1 → 2 → 3 → 4 → 1). (E) $LiPO_3$ (1 → 2 → 3 → 4 → 5 → 6 → 7 → 8 → 1). (F) $LiLa(PO_3)_4$ (1 → 2 → 3 → 4 → 1). (G) $LiCs(PO_3)_2$ (1 → 2 → 3 → 4 → 5 → 6 → 7 → 8 → 1).

Table 3.S1 List of 106 ICSD compounds out of 184 total compounds that pass chemical stability screening (filter 4).

V_{red} and V_{ox} are the reduction limit and oxidation limit of electrochemical stability window in V vs. Li metal, respectively; ΔE_{rxt} is the reaction energy of a material with cathode or electrolyte in eV/atom. Compounds are clustered by their anion types: Cl: chlorides; F: fluorides; NP: non-polyanionic oxides; OF: oxyfluorides; P: polyanionic oxides, and then ranked by V_{ox} in decreasing order within each cluster. Compounds with a trailing star (*) are the ones picked for detailed stability and conductivity studies.

Compounds	**Type**	V_{red}	V_{ox}	ΔE_{rxt} **w/. LPS**	ΔE_{rxt} **w/. fully lithiated NCM**	ΔE_{rxt} **w/. half-lithiated NCM**
$LiGaCl_4$	Cl	2.11	4.51	-0.084	-0.062	-0.035
$LiCs_2YCl_6$	Cl	0.43	4.38	0.000	-0.019	-0.023
$LiCs_2LuCl_6$	Cl	0.43	4.36	0.000	-0.031	-0.027
$LiCs_2ScCl_6$	Cl	0.63	4.34	-0.010	-0.038	-0.030
$LiCs_2InCl_6$	Cl	2.01	4.3	-0.038	-0.012	-0.020
$LiCsCl_2$	Cl	0	4.27	0.000	0.000	-0.017
LiCl	Cl	0	4.25	0.000	0.000	-0.013
$LiRbCl_2$	Cl	0	4.25	0.000	0.000	-0.016
$LiGdCl_4$	Cl	0.76	4.25	-0.049	-0.058	-0.034
Li_2ZnCl_4	Cl	1.96	4.25	-0.067	-0.020	-0.022
$LiBF_4$	F	1.96	7.15	-0.008	-0.099	-0.031
$LiCaGaF_6$	F	2.25	6.84	-0.092	-0.070	-0.011
$LiHF_2$	F	2.46	6.81	-0.063	-0.089	-0.041
$LiCs_2Al_3F_{12}$	F	1.07	6.8	-0.023	-0.039	-0.002
Li_2TiF_6	F	2.15	6.73	-0.065	-0.083	-0.019
Li_2CaHfF_8	F	1.03	6.73	0.000	-0.052	-0.005
Li_2SiF_6	F	1.87	6.69	-0.005	-0.094	-0.032
$Li_3Zr_4F_{19}$	F	1.47	6.67	-0.035	-0.076	-0.017
$LiCaAlF_6$	F	1.09	6.65	0.000	-0.042	-0.003
$LiYF_4$	F	0.37	6.64	0.000	-0.016	0.000

Li_2HfF_6	F	1.05	6.64	0.000	-0.060	-0.006
$LiSrAlF_6$	F	1.08	6.63	-0.007	-0.041	-0.003
$LiKBeF_4$	F	0.81	6.61	-0.022	-0.026	-0.002
LiK_2AlF_6	F	0.88	6.61	-0.029	-0.016	0.000
$Li_3Na_3Al_2F_{12}$	F	0.99	6.59	0.000	-0.026	-0.001
Li_2ZrF_6	F	1.26	6.56	-0.017	-0.064	-0.007
$Li_2RbBe_2F_7$	F	0.85	6.56	-0.007	-0.037	-0.003
$LiBaZr_2F_{11}$	F	1.35	6.53	-0.039	-0.066	-0.009
Li_2BeF_4	F	0.9	6.52	0.000	-0.044	-0.004
Li_3GaF_6	F	2.26	6.52	-0.087	-0.067	-0.010
$LiBaAlF_6$	F	1.05	6.52	-0.034	-0.038	-0.002
$LiCsBeF_4$	F	0.75	6.52	-0.001	-0.021	0.000
Li_3AlF_6	F	1.09	6.5	0.000	-0.040	-0.003
$Li_3Na_3In_2F_{12}$	F	2.44	6.47	-0.095	-0.054	-0.007
Li_4ZrF_8	F	1.21	6.41	-0.012	-0.056	-0.006
$Li_3Na_3Sc_2F_{12}$	F	0.53	6.4	-0.007	-0.026	0.000
LiF	F	0	6.39	0.000	0.000	0.000
$LiKYF_5$	F	0.35	6.39	-0.037	-0.008	0.000
$LiLuF_4$	F	0.31	6.32	0.000	-0.021	0.000
$LiCsF_2$	F	0.61	5.98	-0.046	0.000	0.000
$LiCaCrF_6$	F	2.52	5.33	-0.093	-0.069	-0.035
$LiBaCrF_6$	F	2.4	5.24	-0.099	-0.067	-0.033
Li_3CrF_6	F	2.5	5.12	-0.087	-0.067	-0.034
$Li_3Na_3Cr_2F_{12}$	F	2.23	5.11	-0.080	-0.052	-0.022
$Li_2K_5NdF_{10}$	F	0.58	4.99	-0.096	-0.025	-0.020
$Li_3V(H_4O_3)_4$	NP	1.92	4.17	-0.093	0.000	0.000
$LiAl_5O_8$	NP	0.85	4.09	0.000	-0.015	0.000
LiB_6O_9F	OF	1.92	4.77	0.000	-0.051	-0.010
$LiKMg_2Si_4(O_5F)_2$	OF	1.13	4.58	0.000	-0.007	0.000
$LiCrPO_4F$	OF	2.55	4.52	-0.090	-0.066	-0.037
$Li_2Ca_3Be_3Si_3(O_6F)_2$	OF	1.01	4.04	-0.028	-0.001	0.000
$LiCs(PO_3)_2^*$	P	2.15	6.23	-0.063	-0.062	-0.013
$LiGd(PO_3)_4$	P	2.52	5.3	-0.034	-0.095	-0.037
$LiSm(PO_3)_4$	P	2.5	5.19	-0.034	-0.095	-0.038
$LiK(PO_3)_2$	P	2.41	5.09	-0.048	-0.075	-0.029
$LiLa(PO_3)_4^*$	P	2.51	5.03	-0.035	-0.095	-0.038
$LiPO_3^*$	P	2.52	5.01	-0.030	-0.089	-0.035
$LiAl(PO_3)_4$	P	2.61	5.01	-0.042	-0.100	-0.042
$LiSr(B_3O_5)_3$	P	1.63	4.89	-0.007	-0.018	-0.002

$LiY(PO_3)_4$	P	2.59	4.87	-0.040	-0.099	-0.041
$LiDy(PO_3)_4$	P	2.6	4.86	-0.041	-0.099	-0.042
$LiBa(B_3O_5)_3^*$	P	1.3	4.83	-0.001	-0.010	0.000
$Li_3Ba_2(PO_3)_7$	P	2.63	4.77	-0.054	-0.094	-0.038
$LiH_2B_5O_9$	P	1.86	4.7	0.000	-0.020	-0.001
$LiInP_2O_7$	P	2.41	4.61	-0.087	-0.067	-0.012
$LiTi_2(PO_4)_3^*$	P	2.37	4.59	-0.046	-0.072	-0.014
$LiH_2PO_4^*$	P	2.23	4.58	-0.021	-0.058	-0.015
$LiCs(B_3O_5)_2$	P	1.14	4.52	0.000	0.000	0.000
$LiZr_2(PO_4)_3$	P	2.06	4.52	-0.005	-0.057	-0.005
$LiScP_2O_7$	P	2.29	4.51	-0.005	-0.057	-0.015
$Li_4Be_3P_3ClO_{12}$	P	1.75	4.5	0.000	-0.028	-0.013
$LiCrPHO_5$	P	2.22	4.46	-0.078	-0.047	-0.023
$Li_4Be_3P_3BrO_{12}$	P	1.74	4.43	0.000	-0.027	-0.009
$LiKZnP_2O_7$	P	2.3	4.43	-0.085	-0.050	-0.014
$LiCa_9Mg(PO_4)_7$	P	1.38	4.43	-0.017	-0.002	0.000
$LiCs_2Al(PO_4)_2$	P	1.6	4.43	-0.041	-0.015	0.000
$Li_4P_2O_7$	P	2.33	4.36	-0.007	-0.051	-0.015
LiB_3O_5	P	2.09	4.35	-0.003	-0.021	-0.008
$Li_3B_7O_{12}$	P	1.36	4.35	0.000	-0.011	0.000
$Li_2InP_2HO_8$	P	2.36	4.31	-0.073	-0.054	-0.007
$Li_2ScP_2HO_8$	P	2.16	4.31	-0.003	-0.042	-0.005
$Li_9Ga_3P_8O_{29}$	P	2.42	4.26	-0.061	-0.067	-0.016
$Li_2Al(BO_2)_5$	P	1.62	4.25	0.000	-0.013	0.000
$LiMgPO_4$	P	1.63	4.23	0.000	-0.024	-0.001
$Li_3Sc_2(PO_4)_3$	P	1.9	4.23	0.000	-0.040	-0.003
Li_3PO_4	P	0.71	4.22	0.000	0.000	0.000
$Li_4Zn(PO_4)_2$	P	2.14	4.22	-0.063	-0.028	-0.003
$LiB_3P(HO_3)_3$	P	2.33	4.22	-0.012	-0.050	-0.015
$Li_4Co(PO_4)_2$	P	2.66	4.19	-0.084	-0.030	-0.017
$LiTaSiO_5$	P	1.55	4.17	-0.098	-0.012	0.000
$Li_2TiIn(PO_4)_3$	P	2.52	4.16	-0.073	-0.065	-0.011
$LiTiPO_5$	P	2.37	4.15	-0.056	-0.061	-0.011
$LiMn(PO_3)_3$	P	2.6	4.13	-0.094	-0.099	-0.055
$LiAl(Si_2O_5)_2$	P	1.34	4.12	0.000	-0.023	-0.001
$LiCaPO_4$	P	1.25	4.1	-0.018	0.000	0.000
$LiAl(SiO_3)_2$	P	1.33	4.1	0.000	-0.017	-0.001
$LiAlSiO_4$	P	1.14	4.09	0.000	-0.009	0.000
$LiNa_2AlP_2H_2O_9$	P	2.12	4.08	-0.028	-0.031	-0.004

$LiNaZr(Si_2O_5)_3$	P	1.29	4.07	-0.020	-0.018	0.000
$LiAlPHO_5$	P	2.02	4.06	-0.010	-0.042	-0.004
$LiTi_3MnCr(PO_4)_6$	P	2.68	4.05	-0.078	-0.076	-0.032
Li_2NaPO_4	P	0.71	4.02	-0.030	0.000	0.000
$Li_3Cr_2(PO_4)_3$	P	2.67	4.02	-0.081	-0.063	-0.034
$Li_2Cs_4\ (Si_2O_5)_3$	P	0.96	4.02	-0.065	0.000	0.000
$Li_4B_7O_{12}Cl$	P	1.39	4.01	0.000	-0.010	-0.013
$Li_3KZr_2(Si_2O_5)_6$	P	1.29	4.01	-0.012	-0.018	0.000

Table 3.S2 Reaction energies ΔE_{rxt} at fully lithiated cathode/SSE, fully lithiated cathode/coating and coating/SSE interfaces in meV/atom.

		Fully lithiated cathodes				**SSEs**			
		NCM	LCO	LMO	LFPO	LPSCl	LGPS	LPS	LLZO
Non-polyanionic oxides	Li_2ZrO_3	0	0	-33	-66	-88	-90	-115	-4
	$LiNbO_3$	-4	0	0	-23	-123	-126	-164	-69
	$LiTaO_3$	0	0	0	-20	-115	-108	-139	-62
Polyanionic oxides	LiH_2PO_4	-58	-61	-17	0	-46	-35	-21	-130
	$LiTi_2(PO_4)_3$	-72	-58	-11	0	-71	-62	-46	-186
	$LiBa(B_3O_5)_3$	-10	0	0	0	-5	-3	-1	-78
	$LiPO_3$	-89	-76	-36	-10	-52	-43	-30	-202
	$LiLa(PO_3)_4$	-95	-80	-41	-10	-63	-53	-35	-218
	$LiCs(PO_3)_2$	-62	-55	-6	0	-85	-77	-63	-155
SSEs	LPSCl	-330	-339	-421	-101				
	LGPS	-351	-362	-464	-94				
	LPS	-422	-426	-531	-84				
	LLZO	-1	-2	-63	-94				

Table 3.S3 Reaction energies ΔE_{rxt} at half-lithiated cathode/SSE and half-lithiated cathode/coating interfaces in meV/atom.

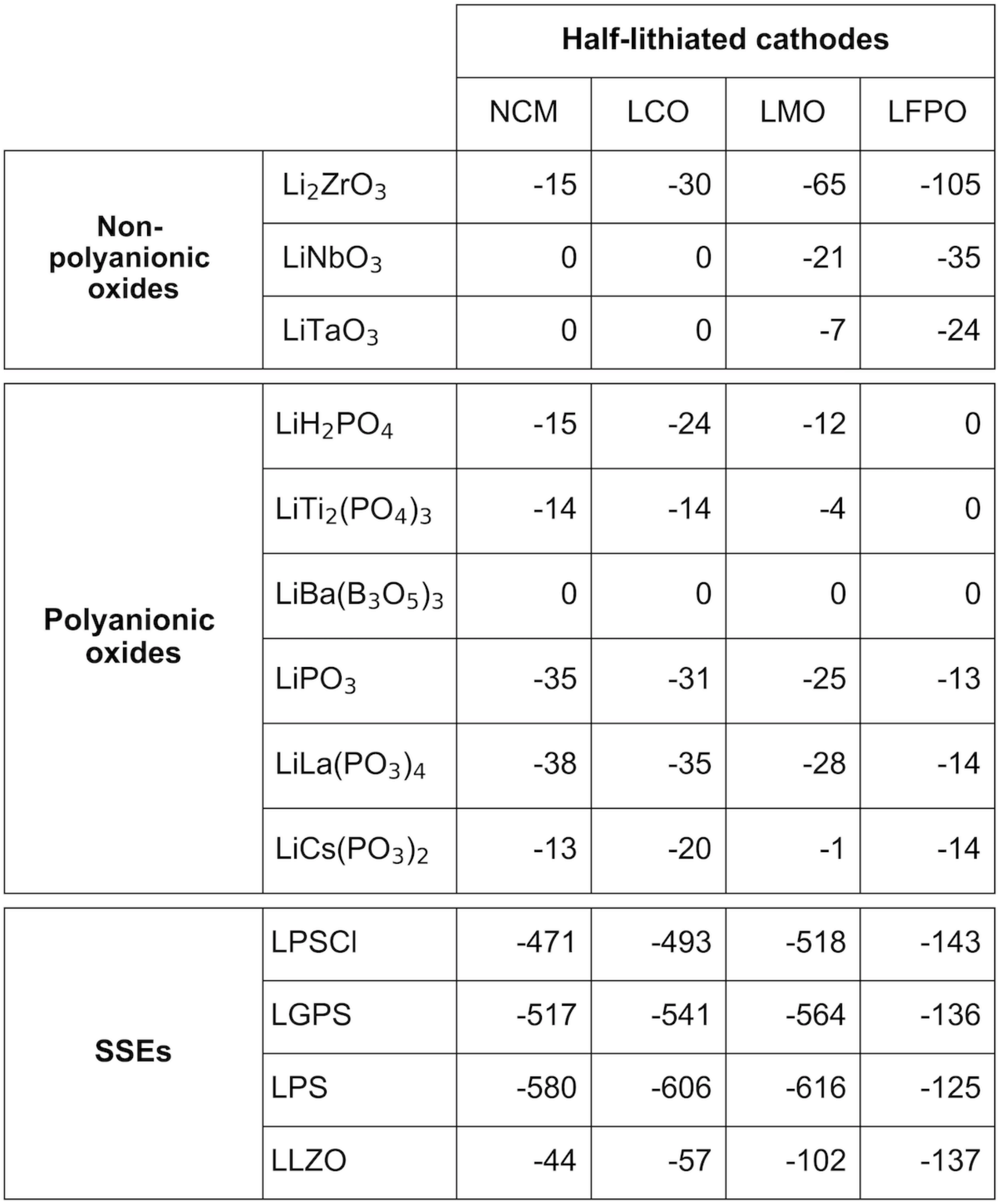

		Half-lithiated cathodes			
		NCM	LCO	LMO	LFPO
Non-polyanionic oxides	Li_2ZrO_3	-15	-30	-65	-105
	$LiNbO_3$	0	0	-21	-35
	$LiTaO_3$	0	0	-7	-24
Polyanionic oxides	LiH_2PO_4	-15	-24	-12	0
	$LiTi_2(PO_4)_3$	-14	-14	-4	0
	$LiBa(B_3O_5)_3$	0	0	0	0
	$LiPO_3$	-35	-31	-25	-13
	$LiLa(PO_3)_4$	-38	-35	-28	-14
	$LiCs(PO_3)_2$	-13	-20	-1	-14
SSEs	LPSCl	-471	-493	-518	-143
	LGPS	-517	-541	-564	-136
	LPS	-580	-606	-616	-125
	LLZO	-44	-57	-102	-137

Table 3.S4 Chemical reaction products from the most favorable reactions at cathodes/coating interfaces or cathode/SSE interfaces.

Interfaces	Fully lithiated cathode	Half-lithiated cathode
NCM/Li_2ZrO_3	stable	$LiNiO_2$, NiO, Li_2MnO_3, ZrO_2, $Li_2Co_3NiO_8$
$LiCoO_2$/ Li_2ZrO_3	stable	Li_2CoO_3, $LiCoO_2$, ZrO_2
$LiMn_2O_4$/Li_2ZrO_3	$LiMnO_2$, Li_2MnO_3, ZrO_2	Li_2MnO_3, $LiMnO_2$, ZrO_2
$LiFePO_4$/Li_2ZrO_3	Li_3PO_4, FeO, ZrO_2	ZrO_2, Li_3PO_4, Fe_3O_4, FeO
NCM/$LiNbO_3$	Li_3NbO_4, $LiMnCoO_4$, NiO	stable
$LiCoO_2$/$LiNbO_3$	stable	stable
$LiMn_2O_4$/$LiNbO_3$	stable	Mn_2O_3, $Li_5Mn_7O_{16}$, Nb_2O_5
$LiFePO_4$/$LiNbO_3$	Nb_2FeO_6, Li_3PO_4	Li_3PO_4, Nb_2FeO_6, Fe_2O_3, Nb_2O_5
NCM/$LiTaO_3$	stable	stable
$LiCoO_2$/$LiTaO_3$	stable	stable
$LiMn_2O_4$/$LiTaO_3$	stable	$Li_5Mn_7O_{16}$, $LiTa_3O_8$, Mn_2O_3
$LiFePO_4$/$LiTaO_3$	Ta_2FeO_6, Li_3PO_4	Li_3PO_4, $TaFeO_4$, Ta_2FeO_6, $TaPO_5$
NCM/LiH_2PO_4	$HCoO_2$, Li_3PO_4, $Li_2Mn_3NiO_8$, $Ni(HO)_2$	$Ni_3P_2(HO)_{16}$, O_2, Li_3PO_4, $LiMnCoO_4$, $Ni_3(PO_4)_2$
$LiCoO_2$/LiH_2PO_4	$HCoO_2$, Li_3PO_4	$HCoO_2$, CoO_2, Li_3PO_4
$LiMn_2O_4$/LiH_2PO_4	$MnPH_2O_5$, Li_3PO_4, H_2O, MnO_2	MnO_2, Li_3PO_4, $MnPH_2O_5$, H_2O
$LiFePO_4$/LiH_2PO_4	stable	stable
NCM/$LiTi_2(PO_4)_3$	$LiMnCoO_4$, Li_3PO_4, $Ti(NiO_2)_2$	O_2, $LiMnCoO_4$, TiO_2, Li_3PO_4, $Ni_3(PO_4)_2$
$LiCoO_2$/$LiTi_2(PO_4)_3$	Co_3O_4, TiO_2, $Li_5(CoO_2)_{12}$, Li_3PO_4	Co_3O_4, CoO_2, TiO_2, Li_3PO_4
$LiMn_2O_4$/$LiTi_2(PO_4)_3$	MnO_2, Mn_2O_3, TiO_2, Li_3PO_4	Mn_2O_3, Li_3PO_4, TiO_2, MnO_2
$LiFePO_4$/$LiTi_2(PO_4)_3$	stable	stable
NCM/$LiBa(B_3O_5)_3$	$LiMnCoO_4$, NiO, $LiBO_2$, $Ba_2Li(BO_2)_5$	stable
$LiCoO_2$/$LiBa(B_3O_5)_3$	stable	stable
$LiMn_2O_4$/$LiBa(B_3O_5)_3$	stable	stable
$LiFePO_4$/$LiBa(B_3O_5)_3$	stable	stable
NCM/$LiPO_3$	$LiMnCoO_4$, Li_3PO_4, $Ni_3(PO_4)_2$	$LiMnCoO_4$, O_2, Li_3PO_4, $Ni_3(PO_4)_2$
$LiCoO_2$/$LiPO_3$	$Li_5(CoO_2)_{12}$, Li_3PO_4, Co_3O_4	$LiCoPO_4$, CoO_2, Li_3PO_4
$LiMn_2O_4$/$LiPO_3$	MnO_2, $MnPO_4$, Li_3PO_4	$Li_4P_2O_7$, $MnPO_4$, MnO_2
$LiFePO_4$/$LiPO_3$	$Fe_2P_2O_7$, $Li_4P_2O_7$	$Li_4P_2O_7$, $Fe_2P_2O_7$, $LiFeP_2O_7$
NCM/$LiLa(PO_3)_4$	$LiMnCoO_4$, $LaPO_4$, Li_3PO_4, $Ni_3(PO_4)_2$	$LiMnCoO_4$, O_2, $LaPO_4$, Li_3PO_4, $Ni_3(PO_4)_2$
$LiCoO_2$/$LiLa(PO_3)_4$	CoO_2, $LaPO_4$, Co_3O_4, Li_3PO_4	$CoPO_4$, $LaPO_4$, $Li_4P_2O_7$, CoO_2

$LiMn_2O_4/LiLa(PO_3)_4$	MnO_2, $MnPO_4$, Li_3PO_4, $LaPO_4$	$Li_4P_2O_7$, $LaPO_4$, $MnPO_4$, MnO_2
$LiFePO_4/LiLa(PO_3)_4$	$Li_4P_2O_7$, $LaPO_4$, $Fe_2P_2O_7$	$LiFeP_2O_7$, $LaPO_4$, $Fe_2P_2O_7$, $Li_4P_2O_7$
$NCM/LiCs(PO_3)_2$	Cs_3PO_4, $CsCoPO_4$, $Co(NiO_2)_2$, $Li_2Mn_3NiO_8$, $LiMnCoO_4$, Li_3PO_4	$Li_2Mn_3NiO_8$, Li_3PO_4, $Ni_3(PO_4)_2$, $CsCoPO_4$, $CsMnO_4$, O_2
$LiCoO_2/LiCs(PO_3)_2$	$CsCoPO_4$, $Li_5(CoO_2)_{12}$, Li_3PO_4	$CsCoPO_4$, CoO_2, Li_3PO_4
$LiMn_2O_4/LiCs(PO_3)_2$	$Li_5Mn_7O_{16}$, Li_3PO_4, Cs_3PO_4, Mn_2O_3	Mn_2O_3, Li_3PO_4, Cs_3PO_4, MnO_2
$LiFePO_4/LiCs(PO_3)_2$	stable	$CsFeP_2O_7$, $Li_4P_2O_7$, $Fe_2P_2O_7$
NCM/LPSCl	Ni_3S_2, Li_2SO_4, Li_2S, LiCl, MnS, Co_9S_8, Li_3PO_4	MnS, Li_2SO_4, Ni_3S_2, Li_3PO_4, Li_2O, Co_9S_8, LiCl
$LiCoO_2$/LPSCl	Li_3PO_4, Li_2S, Co_9S_8, Li_2SO_4, LiCl	Li_2SO_4, Li_3PO_4, Li_2O, Co_9S_8, LiCl
$LiMn_2O_4$/LPSCl	LiCl, Li_3PO_4, Li_2SO_4, Li_2S, MnS	Li_2SO_4, Li_3PO_4, Li_2O, LiCl, MnS
$LiFePO_4$/LPSCl	FeS_2, Li_3PO_4, $FePS_3$, LiCl, FeP	FeP, $FePS_3$, $Li_4P_2O_7$, LiCl, FeS_2
NCM/LGPS	MnS, Co_2NiS_4, Li_2SO_4, Li_3PO_4, Li_4GeO_4, Li_2S, Ni_3S_2	MnS, Li_2SO_4, Co_9S_8, Li_2S, Li_4GeO_4, Li_3PO_4, Ni_3S_2
$LiCoO_2$/LGPS	Li_2SO_4, Li_2S, Li_4GeO_4, Li_3PO_4, Co_9S_8	Li_2O, Li_2SO_4, Li_3PO_4, Li_4GeO_4, Co_9S_8
$LiMn_2O_4$/LGPS	Li_4GeO_4, MnS, Li_2SO_4, Li_3PO_4, Li_2S	Li_2GeO_3, MnS, Li_4GeO_4, Li_3PO_4, Li_2SO_4
$LiFePO_4$/LGPS	GeS_2, Li_3PO_4, $FePS_3$, FeP, FeS_2	GeS_2, $Li_4P_2O_7$, $FePS_3$, FeP, FeS_2
NCM/LPS	Ni_3S_4, MnS, Co_2NiS_4, Li_3PO_4, MnS_2, Li_2S	Li_2S, Li_3PO_4, MnS, Ni_3S_2, Co_9S_8, Li_2SO_4
$LiCoO_2$/LPS	Li_2SO_4, Li_2S, Li_3PO_4, Co_9S_8	Li_2S, Li_2SO_4, Li_3PO_4, Co_9S_8
$LiMn_2O_4$/LPS	Li_2S, Li_3PO_4, Li_2SO_4, MnS	Li_2SO_4, MnS, SO_2, Li_3PO_4
$LiFePO_4$/LPS	$Li_4P_2O_7$, FeP, $FePS_3$, FeS_2	FeS_2, $Li_4P_2O_7$, FeP, $FePS_3$
NCM/LLZO	Li_5CoO_4, NiO, La_2O_3, $Li_6Zr_2O_7$, Li_2MnO_3	La_2MnNiO_6, NiO, $LiNiO_2$, Li_2CoO_3, $La_2Zr_2O_7$, Li_2MnO_3
$LiCoO_2$/LLZO	$Li_6Zr_2O_7$, La_2O_3, Li_5CoO_4	$La_2Zr_2O_7$, $LiCoO_2$, La_2O_3, Li_2CoO_3
$LiMn_2O_4$/LLZO	$LaMnO_3$, Li_2MnO_3, $LiMnO_2$, $La_2Zr_2O_7$	Li_2MnO_3, $LaMnO_3$, $La_2Zr_2O_7$, $LiMnO_2$
$LiFePO_4$/LLZO	La_3FeO_6, Li_3PO_4, $La_2Zr_2O_7$, Fe, FeO	Fe_3O_4, $La_2Zr_2O_7$, Li_3PO_4, $LaPO_4$, FeO

Table 3.S5 Chemical reaction products for the most favorable reactions at SSE/coating interfaces.

Interfaces	Reaction products
$LPSCl/Li_2ZrO_3$	Li_2S, Li_3PO_4, Li_2ZrS_3, LiCl
$LGPS/Li_2ZrO_3$	Li_4GeS_4, Li_2ZrS_3, Li_3PO_4

LPS/Li_2ZrO_3	Li_3PO_4, Li_2ZrS_3
LLZO/Li_2ZrO_3	$Li_6Zr_2O_7$, La_2O_3
LPSCl/$LiNbO_3$	Li_2S, LiCl, $Li_5(NbS_2)_7$, S, Li_3PO_4
LGPS/$LiNbO_3$	S, Li_2S, Li_3PO_4, Li_4GeS_4, $Li_5(NbS_2)_7$
LPS/$LiNbO_3$	S, Li_3PO_4, $Li_5(NbS_2)_7$, Li_2S
LLZO/$LiNbO_3$	Li_3NbO_4, $LaNbO_4$, $La_2Zr_2O_7$
LPSCl/$LiTaO_3$	TaS_3, Li_3PO_4, $Li_2(TaS_2)_3$, LiCl, Li_3TaS_4
LGPS/$LiTaO_3$	TaS_3, Li_3PO_4, Li_3TaS_4, $Li_2(TaS_2)_3$, Li_2GeS_3
LPS/$LiTaO_3$	$Li_2(TaS_2)_3$, Li_3PO_4, TaS_3, Li_3TaS_4
LLZO/$LiTaO_3$	Li_3TaO_4, $La_2Zr_2O_7$, La_3TaO_7
LPSCl/LiH_2PO_4	H_2S, Li_3PS_4, LiCl, Li_3PO_4
LGPS/LiH_2PO_4	P_2S_5, H_2S, Li_3PO_4, GeS_2
LPS/LiH_2PO_4	H_2S, P_2S_5, Li_3PO_4
LLZO/LiH_2PO_4	Li_3PO_4, $La_2Zr_2O_7$, $La(HO)_3$, LiH_3O_2
LPSCl/$LiTi_2(PO_4)_3$	Li_3PO_4, $Ti(PS_3)_2$, TiS_3, LiCl, TiS_2
LGPS/$LiTi_2(PO_4)_3$	Li_3PO_4, $Ti(PS_3)_2$, GeS_2, TiS_3, TiS_2
LPS/$LiTi_2(PO_4)_3$	S, TiS_3, Li_3PO_4, $Ti(PS_3)_2$
LLZO/$LiTi_2(PO_4)_3$	Li_3PO_4, $La_2Ti_2O_7$, ZrO_2, $LaPO_4$
LPSCl/$LiBa(B_3O_5)_3$	$Ba(BS_2)_2$, $BaLiBS_3$, $Ba_3(PS_4)_2$, LiCl, $Li_3B_7O_{12}$
LGPS/$LiBa(B_3O_5)_3$	$Li_3B_7O_{12}$, Li_3PS_4, $Li_3B_5S_9$, $BaLi_2GeS_4$, Li_2GeS_3
LPS/$LiBa(B_3O_5)_3$	$Ba_3(PS_4)_2$, S, $Li_3B_7O_{12}$, $BaPS_3$, BS_2
LLZO/$LiBa(B_3O_5)_3$	$BaLiBO_3$, Li_3BO_3, $LaBO_3$, $La_2Zr_2O_7$
LPSCl/$LiPO_3$	Li_3PS_4, LiCl, Li_3PO_4
LGPS/$LiPO_3$	Li_3PO_4, P_2S_5, GeS_2
LPS/$LiPO_3$	P_2S_5, Li_3PO_4
LLZO/$LiPO_3$	Li_3PO_4, ZrO_2, $LaPO_4$
LPSCl/$LiLa(PO_3)_4$	LiCl, Li_3PO_4, P_2S_5, $LaPS_4$
LGPS/$LiLa(PO_3)_4$	P_2S_5, Li_3PO_4, GeS_2, $LaPS_4$
LPS/$LiLa(PO_3)_4$	P_2S_5, $Li_4P_2O_7$, $LaPS_4$
LLZO/$LiLa(PO_3)_4$	Li_3PO_4, $LaPO_4$, ZrO_2
LPSCl/$LiCs(PO_3)_2$	P_2S_5, Li_3PO_4, LiCl, $CsPS_3$
LGPS/$LiCs(PO_3)_2$	GeS_2, $CsPS_3$, Li_3PO_4, $Li_4P_2O_7$
LPS/$LiCs(PO_3)_2$	P_2S_5, $CsPS_3$, $Li_4P_2O_7$
LLZO/$LiCs(PO_3)_2$	Cs_3PO_4, Li_3PO_4, $La_2Zr_2O_7$, $LaPO_4$

Table 3.S6 All NEB calculated migration barriers for single Li vacancy migration for Li_2ZrO_3 and the six polyanionic oxides.

Materials	NEB activation energies for single hop (eV)
Li_2ZrO_3	0.48, 0.55, 0.58, 0.7, 0.8
LiH_2PO_4	0.33, 1.20, 1.24, 1.32, 1.42, 1.99
$LiTi_2(PO_4)_3$	0.42
$LiBa(B_3O_5)_3$	1.96
$LiPO_3$	0.1, 0.25, 0.26, 0.32, 0.36, 0.40, 0.50

$LiLa(PO_3)_4$	1.39, 1.65, 2.60
$LiCs(PO_3)_2$	0.43, 0.84, 1.27, 1.28, 1.54, 1.70

Chapter 4: Conclusions and outlook

Part of this chapter has been published in:
Xiao, Y., Wang, Y., Bo, S. H., Kim, J. C., Miara, L. J., & Ceder, G. (2020). Understanding interface stability in solid-state batteries. Nature Reviews Materials, 5, 105–126.

4.1 Conclusions

In conclusion, this dissertation employs first-principles-based computational methods to tackle two critical bottlenecks in the development of SSBs: the search for new SSE materials, and the creation of stable interfaces in SSBs.

Chapter 2 presented a feature-guided computational search for lithium oxide SICs. Based on the analysis of the Li diffusion networks of lithium garnet and NASICON structures, we identified a common ion-conduction pattern, denoted “activated diffusion network,” in both compounds. In this pattern, the local environments in the pristine Li diffusion network are quiescent for ionic conduction, but stuffing an excess Li ion into the network creates an “activated local environment” where the Li migration barrier becomes much lower via a cooperative motion of nearby Li ions. The activated local environment can propagate through the diffusion network, leading to superionic conduction in the Li-stuffed material. Then, three features of diffusion network were considered beneficial for activating such an ion-conduction pattern upon Li stuffing, i.e., a 3D percolating network, short distances between occupied Li sites, and “homogenous local environments.” Using these network features as screening criteria, we identified 7 promising lithium oxide SIC candidates with σ_{rt} of ~0.1 mS/cm or higher predicted by AIMD simulations. Notably, the candidates Li_2TeO_4 and $LiMg(SeO_3)_2$ indeed show high topological similarity to garnet and NASICON in their Li diffusion networks, respectively. Furthermore, several structural frameworks that have not been previously considered for oxide SSEs emerged, including spinel, oxy-argyrodite, sodalite and $LiM(SeO_3)_2$, presenting exciting opportunities for future development of oxide SSEs.

In Chapter 3, a high-throughput computational screening was performed to search for optimal cathode coating materials for SSBs. The screening results showed that fluorides, chlorides and polyanionic oxides exhibit better oxidation stability and chemical stability (against thiophosphate SSE) than conventional ternary metal oxide coatings. Among polyanionic oxides, lithium borates were highlighted due to their exceptional (electro)chemical stability at various interfaces of different cathode/SSE combinations. Three phosphate compounds LiH_2PO_4, $LiTi_2(PO_4)_3$, and $LiPO_3$ were identified as particularly appealing candidates due to their combined high (electro)chemical stability and low activation energies for Li transport. In this study, we found that for polyanionic oxides, the strong covalency between non-metal element M and O in the many MO_x polyhedral units lowers the energy of the oxygen orbitals, thereby protecting them from oxidation. This effect explains the increased oxidation stability and also the decreased chemical reactivity of the polyanionic compounds compared with conventional metal oxide coating materials. Besides, we identified a general trade-off between ionic conductivity and oxidation stability of polyanionic oxides: although a high oxidation limit indicates a low Li content in the compound, a high ionic conductivity is correlated to a high Li content. Finally, we noted that coating selection depends on the specific cathode and SSE combination and processing technique. We recommended phosphate coatings to be paired with sulfide SSEs, and metal oxide coatings such as $LiNbO_3$ and $LiTaO_3$ for pairing with LLZO. Lithium borates were recommended for all oxide cathode/sulfide SSE interfaces.

4.2 Outlook

The recent advances in computational modeling and experimental synthesis, processing, and characterization techniques have greatly narrowed the gap between experimental observations and computational predictions. For the SSE development, ionic conductivities and activation energies predicted using AIMD simulation and DFT-based NEB method showed reasonably good agreement with experimentally measured values.[69,132,161,194] Moreover, the mechanisms underlying the high ionic conductivity of Li-ion conductors are reasonably well established thanks to the insights from first-principles computations.[62,64] These insights have led to the rapid development of new SICs such as $Li_{1+2x}Zn_{1-x}PS_4$ ($\sigma_{rt} = 8 \times 10^{-4}$ S/cm)[69,70] and $Li_{1+x}Ta_{1-x}Zr_xSiO_5$ ($\sigma_{rt} = 2.97 \times 10^{-5}$ S/cm).[71,72]

However, multiple challenges lie ahead of us in SSE modeling. For the modeling of ion transport in solid materials, the throughput of first-principles computations is bottlenecked by their high computational cost. Also, the room-temperature ionic conductivity predicted by AIMD simulations is typically obtained by extrapolating from high-temperature data assuming the Arrhenius relationship, which does not hold for materials undergoing phase transition between room temperature and simulated temperatures.[256] Therefore, the next important task in SSE modeling is to develop low-cost computational techniques (e.g., machine learning potentials[257]) to speed up the simulation of ion transport even at room temperature. Another issue is that the total ionic conductivity of an SSE is often limited by the grain-boundary resistance, especially for oxide SSEs. However, the grain-boundary resistance cannot always be trivially separated from that of the bulk in conventional impedance measurements.[69] Directly computing the grain-boundary ionic conductivity, on the other hand, requires the ability to model the atomic structure of the grain boundary to a reasonable degree of accuracy, which is a challenging task in its own right. Furthermore, to predict the overall ionic conductivity of an SSE pellet, experimental data and/or mesoscale modeling will be required to describe the microstructure and inter-particle contact in a pellet as a function of the material's mechanical property and processing conditions. For the study of the ion-conduction mechanism in SICs, although previous works have unraveled various mechanisms contributing to superionic conduction, there is still plenty of room for discovering new mechanisms by studying in detail the ion trajectories from AIMD simulations, especially for SICs in amorphous form. It is also intriguing to develop a unified ion conduction theory that resembles the energy band theory of electronic conductivity for solids, although the task will be extremely challenging due to the strong correlation between ions. Experimentally, a fast and efficient synthesis-processing-testing workflow should be developed to keep up with the accumulating number of computationally predicted SICs. This task requires innovations in techniques such as low-temperature processing[258] and local ionic conductivity measurements[259] as the conventional high-temperature sintering and pelleting procedures have become the rate-limiting steps in the experimental development of oxide SSEs.

For the modeling of interface reactions, high-throughput computing[260,261] and the establishment of large databases of ab initio phase diagrams, such as the Materials Project,[159] have made it fairly straightforward to compute the thermodynamic reaction products that will form at an interface. Many of these predicted decomposition products have been confirmed using advanced characterization techniques. Even when the predicted interphases are not observed in experiments, the computational results often capture the qualitative features of the interfacial reactions, such as the redox center driving the electrochemical decomposition, the preferred bond formation upon chemical mixing and the formation of a stable interface, an MCI or an SEI. The predictive power of these interface models can effectively guide the reverse engineering of interfaces in SSBs, either by interface modifications[94] or coating design as demonstrated in Chapter 3. Nevertheless, factors such as the rate of elemental diffusion, new phase nucleation and whether new phases formed at the interface will be amorphous or crystalline are difficult to predict using current computational methods. The time scale relevant to experimental observations cannot be achieved in explicit interface modeling using ab initio techniques. Further development of these models should aim to include kinetic factors to predict, for example, the most likely reaction pathways and products (including amorphous phases), stricter bounds for kinetic stabilization and the upper bound of the processing temperature. On the experimental side, efforts should be made to elucidate the composition and structure of individual interfaces and interphases under processing and battery-cycling conditions and how they individually affect the cell performance. Stable interfaces should be distinguished from interfaces at which passivation slows down the reaction. This task requires the development of non-destructive, spatially resolved characterization techniques, as well as in situ or operando techniques that can reveal the compositional and structural evolution of the interface. Such experimental data can be used synergistically with computational modeling to shed light on the mechanisms and kinetic pathways of interfacial reactions. Finally, to engineer stable interfaces in SSBs, the current cathode coating strategy still suffers from multiple problems as discussed in Chapter 3, including the unprotected SSE/carbon and SSE/current collector interfaces, and the inherent paradox of electron transport across the cathode coating layer. These challenges call for a more sophisticated morphological design of different components in the electrode composite of SSBs.

References

1 E. Quartarone and P. Mustarelli, *Chem. Soc. Rev.*, 2011, **40**, 2525–2540.

2 P. Arora, R. E. White and M. Doyle, *J. Electrochem. Soc.*, 1998, **145**, 3647–3667.

3 J. Vetter, P. Novák, M. R. Wagner, C. Veit, K.-C. Möller, J. O. Besenhard, M. Winter, M. Wohlfahrt-Mehrens, C. Vogler and A. Hammouche, *J. Power Sources*, 2005, **147**, 269–281.

4 J. Li, C. Ma, M. Chi, C. Liang and N. J. Dudney, *Adv. Energy Mater.*, 2015, **5**, 1401408.

5 D. Lin, Y. Liu and Y. Cui, *Nat. Nanotechnol.*, 2017, **12**, 194–206.

6 W. Xu, J. Wang, F. Ding, X. Chen, E. Nasybulin, Y. Zhang and J.-G. Zhang, *Energy Environ. Sci.*, 2014, **7**, 513–537.

7 R. Bhattacharyya, B. Key, H. Chen, A. S. Best, A. F. Hollenkamp and C. P. Grey, *Nat. Mater.*, 2010, **9**, 504–510.

8 I. Epelboin, M. Froment, M. Garreau, J. Thevenin and D. Warin, *J. Electrochem. Soc.*, 1980, **127**, 2100–2104.

9 F. Han, J. Yue, X. Zhu and C. Wang, *Adv. Energy Mater.*, 2018, **8**, 1703644.

10 X. Yu, J. B. Bates, G. E. Jellison and F. X. Hart, *J. Electrochem. Soc.*, 1997, **144**, 524–532.

11 L. Porz, T. Swamy, B. W. Sheldon, D. Rettenwander, T. Frömling, H. L. Thaman, S. Berendts, R. Uecker, W. C. Carter and Y.-M. Chiang, *Adv. Energy Mater.*, 2017, **7**, 1701003.

12 Y. Ren, Y. Shen, Y. Lin and C.-W. Nan, *Electrochem. Commun.*, 2015, **57**, 27–30.

13 L. O. Valøen and J. N. Reimers, *J. Electrochem. Soc.*, 2005, **152**, A882–A891.

14 A. Ponrouch, E. Marchante, M. Courty, J.-M. Tarascon and M. Rosa Palacín, *Energy Environ. Sci.*, 2012, **5**, 8572–8583.

15 R. Kanno and M. Murayama, *J. Electrochem. Soc.*, 2001, **148**, A742–A746.

16 M. Murayama, N. Sonoyama, A. Yamada and R. Kanno, *Solid State Ion.*, 2004, **170**, 173–180.

17 N. Kamaya, K. Homma, Y. Yamakawa, M. Hirayama, R. Kanno, M. Yonemura, T. Kamiyama, Y. Kato, S. Hama, K. Kawamoto and A. Mitsui, *Nat. Mater.*, 2011, **10**, 682–686.

18 Y. Kato, S. Hori, T. Saito, K. Suzuki, M. Hirayama, A. Mitsui, M. Yonemura, H. Iba and R. Kanno, *Nat. Energy*, 2016, **1**, 16030.

19 S. Ping Ong, Y. Mo, W. Davidson Richards, L. Miara, H. Sug Lee and G. Ceder, *Energy Environ. Sci.*, 2013, **6**, 148–156.

20 A. Hayashi, S. Hama, H. Morimoto, M. Tatsumisago and T. Minami, *J. Am. Ceram. Soc.*, 2001, **84**, 477–79.

21 Y. Seino, T. Ota, K. Takada, A. Hayashi and M. Tatsumisago, *Energy Environ. Sci.*, 2014, **7**, 627–631.

22 H.-J. Deiseroth, S.-T. Kong, H. Eckert, J. Vannahme, C. Reiner, T. Zaiß and M. Schlosser, *Angew. Chem. Int. Ed.*, 2008, **47**, 755–758.

23 R. P. Rao and S. Adams, *Phys. Status Solidi A*, 2011, **208**, 1804–1807.

24 A. Hayashi, K. Noi, A. Sakuda and M. Tatsumisago, *Nat. Commun.*, 2012, **3**, 856.

25 M. Jansen and U. Henseler, *J. Solid State Chem.*, 1992, **99**, 110–119.

26 A. Banerjee, K. H. Park, J. W. Heo, Y. J. Nam, C. K. Moon, S. M. Oh, S.-T. Hong and Y. S. Jung, *Angew. Chem.*, 2016, **128**, 9786–9790.

27 W. D. Richards, T. Tsujimura, L. J. Miara, Y. Wang, J. C. Kim, S. P. Ong, I. Uechi, N. Suzuki and G. Ceder, *Nat. Commun.*, 2016, **7**, 11009.

28 Z. Zhang, E. Ramos, F. Lalère, A. Assoud, K. Kaup, P. Hartman and L. F. Nazar, *Energy Environ. Sci.*, 2018, **11**, 87–93.

29 V. Thangadurai, S. Narayanan and D. Pinzaru, *Chem. Soc. Rev.*, 2014, **43**, 4714–4727.
30 N. Anantharamulu, K. Koteswara Rao, G. Rambabu, B. Vijaya Kumar, V. Radha and M. Vithal, *J. Mater. Sci.*, 2011, **46**, 2821–2837.
31 Y. Zhao and L. L. Daemen, *J. Am. Chem. Soc.*, 2012, **134**, 15042–15047.
32 S. Stramare, V. Thangadurai and W. Weppner, *Chem. Mater.*, 2003, **15**, 3974–3990.
33 Yung-Fang Yu Yao and J. T. Kummer, *J. Inorg. Nucl. Chem.*, 1967, **29**, 2453–2475.
34 H. Y.-P. Hong, *Mater. Res. Bull.*, 1978, **13**, 117–124.
35 P. G. Bruce and A. R. West, *J. Solid State Chem.*, 1982, **44**, 354–365.
36 H. Aono, E. Sugimoto, Y. Sadaoka, N. Imanaka and G. Adachi, *J. Electrochem. Soc.*, 1990, **137**, 1023–1027.
37 S. García-Martín, U. Amador, A. Morata-Orrantia, J. Rodríguez-Carvajal and M. Á. Alario-Franco, *Z. Für Anorg. Allg. Chem.*, 2009, **635**, 2363–2373.
38 C. Ma, K. Chen, C. Liang, C.-W. Nan, R. Ishikawa, K. More and M. Chi, *Energy Environ. Sci.*, 2014, **7**, 1638–1642.
39 X. Xu, Z. Wen, J. Wu and X. Yang, *Solid State Ion.*, 2007, **178**, 29–34.
40 S. Li, J. Zhu, Y. Wang, J. W. Howard, X. Lü, Y. Li, R. S. Kumar, L. Wang, L. L. Daemen and Y. Zhao, *Solid State Ion.*, 2016, **284**, 14–19.
41 S. Ohta, J. Seki, Y. Yagi, Y. Kihira, T. Tani and T. Asaoka, *J. Power Sources*, 2014, **265**, 40–44.
42 Y. Inaguma and M. Nakashima, *J. Power Sources*, 2013, **228**, 250–255.
43 J. Cuan, Y. Zhou, T. Zhou, S. Ling, K. Rui, Z. Guo, H. Liu and X. Yu, *Adv Mater*, 2018, **31**, 1803533.
44 J. A. Teprovich, H. Colón-Mercado, A. L. W. Ii, P. A. Ward, S. Greenway, D. M. Missimer, H. Hartman, J. Velten, J. H. Christian and R. Zidan, *J. Mater. Chem. A*, 2015, **3**, 22853–22859.
45 Y. Sadikin, M. Brighi, P. Schouwink and R. Černý, *Adv. Energy Mater.*, 2015, **5**, 1501016.
46 W. S. Tang, K. Yoshida, A. V. Soloninin, R. V. Skoryunov, O. A. Babanova, A. V. Skripov, M. Dimitrievska, V. Stavila, S. Orimo and T. J. Udovic, *ACS Energy Lett.*, 2016, **1**, 659–664.
47 T. Asano, A. Sakai, S. Ouchi, M. Sakaida, A. Miyazaki and S. Hasegawa, *Adv. Mater.*, 2018, **30**, 1803075.
48 R. Schlem, S. Muy, N. Prinz, A. Banik, Y. Shao-Horn, M. Zobel and W. G. Zeier, *Adv. Energy Mater.*, 2019, **10**, 1903719.
49 L. Zhou, C. Y. Kwok, A. Shyamsunder, Q. Zhang, X. Wu and L. Nazar, *Energy Environ. Sci.*, 2020, **13**, 2056–2063.
50 K.-H. Park, K. Kaup, A. Assoud, Q. Zhang, X. Wu and L. F. Nazar, *ACS Energy Lett.*, 2020, **5**, 533–539.
51 J. Liang, X. Li, S. Wang, K. R. Adair, W. Li, Y. Zhao, C. Wang, Y. Hu, L. Zhang, S. Zhao, S. Lu, H. Huang, R. Li, Y. Mo and X. Sun, *J. Am. Chem. Soc.*, 2020, **142**, 7012–7022.
52 R. Schlem, A. Banik, M. Eckardt, M. Zobel and W. G. Zeier, *ACS Appl. Energy Mater.*, 2020, **3**, 10164–10173.
53 Q. Zhao, S. Stalin, C.-Z. Zhao and L. A. Archer, *Nat. Rev. Mater.*, 2020, **5**, 229–252.
54 C. Wang, K. Fu, S. P. Kammampata, D. W. McOwen, A. J. Samson, L. Zhang, G. T. Hitz, A. M. Nolan, E. D. Wachsman, Y. Mo, V. Thangadurai and L. Hu, *Chem. Rev.*, 2020, **120**, 4257–4300.
55 J. B. Goodenough, H. Y.-P. Hong and J. A. Kafalas, *Mater. Res. Bull.*, 1976, **11**, 203–220.
56 H. Y.-P. Hong, *Mater. Res. Bull.*, 1976, **11**, 173–182.

57 Y. Inaguma, C. Liquan, M. Itoh, T. Nakamura, T. Uchida, H. Ikuta and M. Wakihara, *Solid State Commun.*, 1993, **86**, 689–693.

58 V. Thangadurai, H. Kaack and W. J. F. Weppner, *J. Am. Ceram. Soc.*, 2003, **86**, 437–440.

59 R. Murugan, V. Thangadurai and W. Weppner, *Angew. Chem. Int. Ed.*, 2007, **46**, 7778–7781.

60 G. Schwering, A. Hönnerscheid, L. van Wüllen and M. Jansen, *ChemPhysChem*, 2003, **4**, 343–348.

61 K. Takada, *Acta Mater.*, 2013, **61**, 759–770.

62 Y. Wang, W. D. Richards, S. P. Ong, L. J. Miara, J. C. Kim, Y. Mo and G. Ceder, *Nat. Mater.*, 2015, **14**, 1026–1031.

63 R. Jalem, Y. Yamamoto, H. Shiiba, M. Nakayama, H. Munakata, T. Kasuga and K. Kanamura, *Chem. Mater.*, 2013, **25**, 425–430.

64 X. He, Y. Zhu and Y. Mo, *Nat. Commun.*, 2017, **8**, 15893.

65 B. Kozinsky, S. A. Akhade, P. Hirel, A. Hashibon, C. Elsässer, P. Mehta, A. Logeat and U. Eisele, *Phys. Rev. Lett.*, 2016, **116**, 055901.

66 X. He, Q. Bai, Y. Liu, A. M. Nolan, C. Ling and Y. Mo, *Adv. Energy Mater.*, 2019, **9**, 1902078.

67 A. D. Sendek, Q. Yang, E. D. Cubuk, K.-A. N. Duerloo, Y. Cui and E. J. Reed, *Energy Environ. Sci.*, 2017, **10**, 306–320.

68 L. Kahle, A. Marcolongo and N. Marzari, *Energy Environ. Sci.*, 2020, **13**, 928–948.

69 N. Suzuki, W. D. Richards, Y. Wang, L. J. Miara, J. C. Kim, I.-S. Jung, T. Tsujimura and G. Ceder, *Chem. Mater.*, 2018, **30**, 2236–2244.

70 K. Kaup, F. Lalère, A. Huq, A. Shyamsunder, T. Adermann, P. Hartmann and L. F. Nazar, *Chem. Mater.*, 2018, **30**, 592–596.

71 S. Xiong, X. He, A. Han, Z. Liu, Z. Ren, B. McElhenny, A. M. Nolan, S. Chen, Y. Mo and H. Chen, *Adv. Energy Mater.*, 2019, **9**, 1803821.

72 Q. Wang, J.-F. Wu, Z. Lu, F. Ciucci, W. K. Pang and X. Guo, *Adv. Funct. Mater.*, 2019, **29**, 1904232.

73 K. Takada, N. Ohta, L. Zhang, X. Xu, B. T. Hang, T. Ohnishi, M. Osada and T. Sasaki, *Solid State Ion.*, 2012, **225**, 594–597.

74 S. Wenzel, S. Randau, T. Leichtweiß, D. A. Weber, J. Sann, W. G. Zeier and J. Janek, *Chem. Mater.*, 2016, **28**, 2400–2407.

75 S. Wenzel, T. Leichtweiss, D. Krüger, J. Sann and J. Janek, *Solid State Ion.*, 2015, **278**, 98–105.

76 A. Sakuda, A. Hayashi and M. Tatsumisago, *Chem. Mater.*, 2010, **22**, 949–956.

77 Y. Zhu, X. He and Y. Mo, *J. Mater. Chem. A*, 2016, **4**, 3253–3266.

78 R. Koerver, F. Walther, I. Aygün, J. Sann, C. Dietrich, W. G. Zeier and J. Janek, *J. Mater. Chem. A*, 2017, **5**, 22750–22760.

79 K. Yoon, J.-J. Kim, W. M. Seong, M. H. Lee and K. Kang, *Sci. Rep.*, 2018, **8**, 8066.

80 W. Zhang, T. Leichtweiß, S. P. Culver, R. Koerver, D. Das, D. A. Weber, W. G. Zeier and J. Janek, *ACS Appl. Mater. Interfaces*, 2017, **9**, 35888–35896.

81 W. D. Richards, L. J. Miara, Y. Wang, J. C. Kim and G. Ceder, *Chem. Mater.*, 2016, **28**, 266–273.

82 Y. Zhu, X. He and Y. Mo, *ACS Appl. Mater. Interfaces*, 2015, **7**, 23685–23693.

83 R. Koerver, I. Aygün, T. Leichtweiß, C. Dietrich, W. Zhang, J. O. Binder, P. Hartmann, W. G. Zeier and J. Janek, *Chem. Mater.*, 2017, **29**, 5574–5582.

84 T. Hakari, M. Deguchi, K. Mitsuhara, T. Ohta, K. Saito, Y. Orikasa, Y. Uchimoto, Y. Kowada, A. Hayashi and M. Tatsumisago, *Chem. Mater.*, 2017, **29**, 4768–4774.

85 T. Swamy, X. Chen and Y.-M. Chiang, *Chem. Mater.*, 2019, **31**, 707–713.

86 I.-H. Chu, H. Nguyen, S. Hy, Y.-C. Lin, Z. Wang, Z. Xu, Z. Deng, Y. S. Meng and S. P. Ong, *ACS Appl. Mater. Interfaces*, 2016, **8**, 7843–7853.

87 V. Lacivita, Y. Wang, S.-H. Bo and G. Ceder, *J. Mater. Chem. A*, 2019, **7**, 8144–8155.

88 J. Haruyama, K. Sodeyama and Y. Tateyama, *ACS Appl. Mater. Interfaces*, 2017, **9**, 286–292.

89 Y. Tian, T. Shi, W. D. Richards, J. Li, J. Chul Kim, S.-H. Bo and G. Ceder, *Energy Environ. Sci.*, 2017, **10**, 1150–1166.

90 Y. Mo, S. P. Ong and G. Ceder, *Chem. Mater.*, 2012, **24**, 15–17.

91 L. E. Camacho-Forero and P. B. Balbuena, *J. Power Sources*, 2018, **396**, 782–790.

92 S.-J. Choi, S.-H. Lee, Y.-C. Ha, J.-H. Yu, C.-H. Doh, Y. Lee, J.-W. Park, S.-M. Lee and H.-C. Shin, *J. Electrochem. Soc.*, 2018, **165**, A957–A962.

93 P. Bron, B. Roling and S. Dehnen, *J. Power Sources*, 2017, **352**, 127–134.

94 Y. Tian, Y. Sun, D. C. Hannah, Y. Xiao, H. Liu, K. W. Chapman, S.-H. Bo and G. Ceder, *Joule*, 2019, **3**, 1037–1050.

95 M. Suyama, A. Kato, A. Sakuda, A. Hayashi and M. Tatsumisago, *Electrochimica Acta*, 2018, **286**, 158–162.

96 E. A. Wu, C. S. Kompella, Z. Zhu, J. Z. Lee, S. C. Lee, I.-H. Chu, H. Nguyen, S. P. Ong, A. Banerjee and Y. S. Meng, *ACS Appl. Mater. Interfaces*, 2018, **10**, 10076–10086.

97 F. Schipper, E. M. Erickson, C. Erk, J.-Y. Shin, F. F. Chesneau and D. Aurbach, *J. Electrochem. Soc.*, 2016, **164**, A6220–A6227.

98 E. Antolini and M. Ferretti, *J. Solid State Chem.*, 1995, **117**, 1–7.

99 L. Miara, A. Windmüller, C.-L. Tsai, W. D. Richards, Q. Ma, S. Uhlenbruck, O. Guillon and G. Ceder, *ACS Appl. Mater. Interfaces*, 2016, **8**, 26842–26850.

100 K. Park, B.-C. Yu, J.-W. Jung, Y. Li, W. Zhou, H. Gao, S. Son and J. B. Goodenough, *Chem. Mater.*, 2016, **28**, 8051–8059.

101 S. Ohta, T. Kobayashi and T. Asaoka, *J. Power Sources*, 2011, **196**, 3342–3345.

102 M. Kotobuki and K. Kanamura, *Ceram. Int.*, 2013, **39**, 6481–6487.

103 M. Kotobuki, K. Kanamura, Y. Sato and T. Yoshida, *J. Power Sources*, 2011, **196**, 7750–7754.

104 F. Han, Y. Zhu, X. He, Y. Mo and C. Wang, *Adv. Energy Mater.*, 2016, **6**, 1501590.

105 R. Jalem, Y. Morishita, T. Okajima, H. Takeda, Y. Kondo, M. Nakayama and T. Kasuga, *J. Mater. Chem. A*, 2016, **4**, 14371–14379.

106 X. Ma, B. Kang and G. Ceder, *J. Electrochem. Soc.*, 2010, **157**, A925–A931.

107 A. Manthiram, K. Chemelewski and E.-S. Lee, *Energy Environ. Sci.*, 2014, **7**, 1339–1350.

108 K. H. Kim, Y. Iriyama, K. Yamamoto, S. Kumazaki, T. Asaka, K. Tanabe, C. A. J. Fisher, T. Hirayama, R. Murugan and Z. Ogumi, *J. Power Sources*, 2011, **196**, 764–767.

109 M. Nakayama, M. Kotobuki, H. Munakata, M. Nogami and K. Kanamura, *Phys. Chem. Chem. Phys.*, 2012, **14**, 10008–10014.

110 H. Nemori, Y. Matsuda, S. Mitsuoka, M. Matsui, O. Yamamoto, Y. Takeda and N. Imanishi, *Solid State Ion.*, 2015, **282**, 7–12.

111 Y. Kim, A. Yoo, R. Schmidt, A. Sharafi, H. Lee, J. Wolfenstine and J. Sakamoto, *Front. Energy Res.*, 2016, **4**, 20.

112 D. Rettenwander, R. Wagner, A. Reyer, M. Bonta, L. Cheng, M. M. Doeff, A. Limbeck, M. Wilkening and G. Amthauer, *J. Phys. Chem. C*, 2018, **122**, 3780–3785.

113 C. Ma, Y. Cheng, K. Yin, J. Luo, A. Sharafi, J. Sakamoto, J. Li, K. L. More, N. J. Dudney and M. Chi, *Nano Lett.*, 2016, **16**, 7030–7036.

114 X. Han, Y. Gong, K. (Kelvin) Fu, X. He, G. T. Hitz, J. Dai, A. Pearse, B. Liu, H. Wang, G. Rubloff, Y. Mo, V. Thangadurai, E. D. Wachsman and L. Hu, *Nat. Mater.*, 2017, **16**, 572–579.

115 N. Ohta, K. Takada, L. Zhang, R. Ma, M. Osada and T. Sasaki, *Adv. Mater.*, 2006, **18**, 2226–2229.

116 S. J. Visco, V. Y. Nimon, A. Petrov, K. Pridatko, N. Goncharenko, E. Nimon, L. De Jonghe, Y. M. Volfkovich and D. A. Bograchev, *J. Solid State Electrochem.*, 2014, **18**, 1443–1456.

117 K. Takahashi, K. Hattori, T. Yamazaki, K. Takada, M. Matsuo, S. Orimo, H. Maekawa and H. Takamura, *J. Power Sources*, 2013, **226**, 61–64.

118 K. Okada, N. Machida, M. Naito, T. Shigematsu, S. Ito, S. Fujiki, M. Nakano and Y. Aihara, *Solid State Ion.*, 2014, **255**, 120–127.

119 K. Takada, N. Ohta, L. Zhang, K. Fukuda, I. Sakaguchi, R. Ma, M. Osada and T. Sasaki, *Solid State Ion.*, 2008, **179**, 1333–1337.

120 N. Ohta, K. Takada, I. Sakaguchi, L. Zhang, R. Ma, K. Fukuda, M. Osada and T. Sasaki, *Electrochem. Commun.*, 2007, **9**, 1486–1490.

121 T. Kato, T. Hamanaka, K. Yamamoto, T. Hirayama, F. Sagane, M. Motoyama and Y. Iriyama, *J. Power Sources*, 2014, **260**, 292–298.

122 H. Kitaura, A. Hayashi, K. Tadanaga and M. Tatsumisago, *Solid State Ion.*, 2011, **192**, 304–307.

123 S. H. Jung, K. Oh, Y. J. Nam, D. Y. Oh, P. Brüner, K. Kang and Y. S. Jung, *Chem. Mater.*, 2018, **30**, 8190–8200.

124 S. Ito, S. Fujiki, T. Yamada, Y. Aihara, Y. Park, T. Y. Kim, S.-W. Baek, J.-M. Lee, S. Doo and N. Machida, *J. Power Sources*, 2014, **248**, 943–950.

125 J. Janek and W. G. Zeier, *Nat. Energy*, 2016, **1**, 16141.

126 J. C. Bachman, S. Muy, A. Grimaud, H.-H. Chang, N. Pour, S. F. Lux, O. Paschos, F. Maglia, S. Lupart, P. Lamp, L. Giordano and Y. Shao-Horn, *Chem. Rev.*, 2016, **116**, 140–162.

127 Y. Xiao, Y. Wang, S.-H. Bo, J. C. Kim, L. J. Miara and G. Ceder, *Nat. Rev. Mater.*, 2020, **5**, 105–126.

128 A. Manthiram, X. Yu and S. Wang, *Nat. Rev. Mater.*, 2017, **2**, 16103.

129 W. Huang, K. Yoshino, S. Hori, K. Suzuki, M. Yonemura, M. Hirayama and R. Kanno, *J. Solid State Chem.*, 2019, **270**, 487–492.

130 Z. Liu, W. Fu, E. A. Payzant, X. Yu, Z. Wu, N. J. Dudney, J. Kiggans, K. Hong, A. J. Rondinone and C. Liang, *J. Am. Chem. Soc.*, 2013, **135**, 975–978.

131 L. Zhou, A. Assoud, A. Shyamsunder, A. Huq, Q. Zhang, P. Hartmann, J. Kulisch and L. F. Nazar, *Chem. Mater.*, 2019, **31**, 7801–7811.

132 W. D. Richards, Y. Wang, L. J. Miara, J. Chul Kim and G. Ceder, *Energy Environ. Sci.*, 2016, **9**, 3272–3278.

133 H. Xie, J. A. Alonso, Y. Li, M. T. Fernández-Díaz and J. B. Goodenough, *Chem. Mater.*, 2011, **23**, 3587–3589.

134 C. A. Geiger, E. Alekseev, B. Lazic, M. Fisch, T. Armbruster, R. Langner, M. Fechtelkord, N. Kim, T. Pettke and W. Weppner, *Inorg. Chem.*, 2011, **50**, 1089–1097.

135 M. Xu, M. S. Park, J. M. Lee, T. Y. Kim, Y. S. Park and E. Ma, *Phys. Rev. B*, 2012, **85**, 052301.

136 Y. Chen, E. Rangasamy, C. Liang and K. An, *Chem. Mater.*, 2015, **27**, 5491–5494.

137 M. P. O'Callaghan and E. J. Cussen, *Chem. Commun.*, 2007, 2048–2050.

138 B. Lang, B. Ziebarth and C. Elsässer, *Chem. Mater.*, 2015, **27**, 5040–5048.

139 M. Aykol, S. Kim, V. I. Hegde, S. Kirklin and C. Wolverton, *Phys. Rev. Mater.*, 2019, **3**, 025402.

140 M. P. O'Callaghan, A. S. Powell, J. J. Titman, G. Z. Chen and E. J. Cussen, *Chem. Mater.*, 2008, **20**, 2360–2369.

141 Y. Li, J.- Tao Han, C.- An Wang, H. Xie and J. B. Goodenough, *J. Mater. Chem.*, 2012, **22**, 15357–15361.

142 Y. Wang and W. Lai, *Electrochem. Solid State Lett.*, 2012, **15**, A68–A71.

143 S. Hamdoune, D. Tran Qui and E. J. L. Schouler, *Solid State Ion.*, 1986, **18–19**, 587–591.

144 K. Arbi, S. Mandal, J. M. Rojo and J. Sanz, *Chem. Mater.*, 2002, **14**, 1091–1097.

145 N. V. Kosova, E. T. Devyatkina, A. P. Stepanov and A. L. Buzlukov, *Ionics*, 2008, **14**, 303–311.

146 K. Arbi, J. M. Rojo and J. Sanz, *J. Eur. Ceram. Soc.*, 2007, **27**, 4215–4218.

147 X. Lu, S. Wang, R. Xiao, S. Shi, H. Li and L. Chen, *Nano Energy*, 2017, **41**, 626–633.

148 K. Arbi, M. Hoelzel, A. Kuhn, F. García-Alvarado and J. Sanz, *Inorg. Chem.*, 2013, **52**, 9290–9296.

149 Y. A. Du and N. a. W. Holzwarth, *J. Electrochem. Soc.*, 2007, **154**, A999–A1004.

150 F. H. Stillinger, *Science*, 1995, **267**, 1935–1939.

151 S. Sastry, P. G. Debenedetti and F. H. Stillinger, *Nature*, 1998, **393**, 554–557.

152 P. G. Debenedetti and F. H. Stillinger, *Nature*, 2001, **410**, 259–267.

153 R. Malik, D. Burch, M. Bazant and G. Ceder, *Nano Lett.*, 2010, **10**, 4123–4127.

154 J. O'Rourke and A. P. of C. S. J. O'Rourke, *Computational Geometry in C*, Cambridge University Press, 1998.

155 M. D. Foster, I. Rivin, M. M. J. Treacy and O. Delgado Friedrichs, *Microporous Mesoporous Mater.*, 2006, **90**, 32–38.

156 A. Belsky, M. Hellenbrandt, V. L. Karen and P. Luksch, *Acta Crystallogr. B*, 2002, **58**, 364–369.

157 S. P. Ong, W. D. Richards, A. Jain, G. Hautier, M. Kocher, S. Cholia, D. Gunter, V. L. Chevrier, K. A. Persson and G. Ceder, *Comput. Mater. Sci.*, 2013, **68**, 314–319.

158 Y. Meesala, A. Jena, H. Chang and R.-S. Liu, *ACS Energy Lett.*, 2017, **2**, 2734–2751.

159 A. Jain, S. P. Ong, G. Hautier, W. Chen, W. D. Richards, S. Dacek, S. Cholia, D. Gunter, D. Skinner, G. Ceder and K. A. Persson, *APL Mater.*, 2013, **1**, 011002.

160 L. J. Miara, W. D. Richards, Y. E. Wang and G. Ceder, *Chem. Mater.*, 2015, **27**, 4040–4047.

161 S.-H. Bo, Y. Wang, J. C. Kim, W. D. Richards and G. Ceder, *Chem. Mater.*, 2016, **28**, 252–258.

162 G. Hautier, C. Fischer, V. Ehrlacher, A. Jain and G. Ceder, *Inorg. Chem.*, 2011, **50**, 656–663.

163 C. González, M. L. López, M. Gaitán, M. L. Veiga and C. Pico, *Mater. Res. Bull.*, 1994, **29**, 903–910.

164 D. Z. C. Martin, A. R. Haworth, W. L. Schmidt, P. J. Baker, R. Boston, K. E. Johnston and N. Reeves-McLaren, *Phys. Chem. Chem. Phys.*, 2019, **21**, 23111–23118.

165 W. Zhang, D.-H. Seo, T. Chen, L. Wu, M. Topsakal, Y. Zhu, D. Lu, G. Ceder and F. Wang, *Science*, 2020, **367**, 1030–1034.

166 Y. Wang, A. Huq and W. Lai, *Solid State Ion.*, 2014, **255**, 39–49.

167 S. Ganapathy, A. Vasileiadis, J. R. Heringa and M. Wagemaker, *Adv. Energy Mater.*, 2017, **7**, 1601781.

168 S.-T. Kong, H.-J. Deiseroth, J. Maier, V. Nickel, K. Weichert and C. Reiner, *Z. Für Anorg. Allg. Chem.*, 2010, **636**, 1920–1924.

169 N. J. J. de Klerk, I. Rosłoń and M. Wagemaker, *Chem. Mater.*, 2016, **28**, 7955–7963.

170 W. Huang, C. LinDong, S. Hori, K. Suzuki, M. Yonemura, M. Hirayama and R. Kanno, *Mater. Adv.*, 2020, **1**, 334–340.

171 L. Pauling, *Z. Für Krist. - Cryst. Mater.*, 1930, **74**, 213–225.

172 G. M. Johnson and M. T. Weller, *Inorg. Chem.*, 1999, **38**, 2442–2450.

173 I. Hassan and H. D. Grundy, *Acta Crystallogr. B*, 1984, **40**, 6–13.

174 G. Kelemen, W. Lortz and G. Sch□n, *J. Mater. Sci.*, 1989, **24**, 333–338.

175 Y. Chen, D. An, M. Zhang, C. Hu, M. Mutailipu, Z. Yang, X. Lu and S. Pan, *Inorg. Chem. Front.*, 2017, **4**, 1100–1107.

176 D. W. Lee and K. M. Ok, *Inorg. Chem.*, 2013, **52**, 5176–5184.

177 S. Y. Song and K. M. Ok, *Cryst. Growth Des.*, 2016, **16**, 3076–3080.

178 G. Giester, *Monatshefte Für Chem. Chem. Mon.*, 1994, **125**, 535–538.

179 D. Di Stefano, A. Miglio, K. Robeyns, Y. Filinchuk, M. Lechartier, A. Senyshyn, H. Ishida, S. Spannenberger, D. Prutsch, S. Lunghammer, D. Rettenwander, M. Wilkening, B. Roling, Y. Kato and G. Hautier, *Chem*, 2019, **5**, 2450–2460.

180 A. Aatiq, M. Ménétrier, L. Croguennec, E. Suard and C. Delmas, *J. Mater. Chem.*, 2002, **12**, 2971–2978.

181 V. A. Blatov, G. D. Ilyushin, O. A. Blatova, N. A. Anurova, A. K. Ivanov-Schits and L. N. Dem'yanets, *Acta Crystallogr. B*, 2006, **62**, 1010–1018.

182 N. A. Anurova, V. A. Blatov, G. D. Ilyushin, O. A. Blatova, A. K. Ivanov-Schitz and L. N. Dem'yanets, *Solid State Ion.*, 2008, **179**, 2248–2254.

183 N. A. Anurova and V. A. Blatov, *Acta Crystallogr. B*, 2009, **65**, 426–434.

184 F. Meutzner, W. Münchgesang, N. A. Kabanova, M. Zschornak, T. Leisegang, V. A. Blatov and D. C. Meyer, *Chem. – Eur. J.*, 2015, **21**, 16601–16608.

185 P. E. Blöchl, *Phys. Rev. B*, 1994, **50**, 17953–17979.

186 G. Kresse and J. Furthmüller, *Phys. Rev. B*, 1996, **54**, 11169–11186.

187 J. P. Perdew, K. Burke and M. Ernzerhof, *Phys. Rev. Lett.*, 1996, **77**, 3865–3868.

188 V. I. Anisimov, J. Zaanen and O. K. Andersen, *Phys. Rev. B*, 1991, **44**, 943–954.

189 S. L. Dudarev, G. A. Botton, S. Y. Savrasov, C. J. Humphreys and A. P. Sutton, *Phys. Rev. B*, 1998, **57**, 1505–1509.

190 A. Jain, G. Hautier, S. P. Ong, C. J. Moore, C. C. Fischer, K. A. Persson and G. Ceder, *Phys. Rev. B*, 2011, **84**, 045115.

191 H. Jónsson, G. Mills and K. W. Jacobsen, in *Classical and Quantum Dynamics in Condensed Phase Simulations*, WORLD SCIENTIFIC, 1998, pp. 385–404.

192 S. Nosé, *J. Chem. Phys.*, 1984, **81**, 511–519.

193 W. G. Hoover, *Phys. Rev. A*, 1985, **31**, 1695–1697.

194 X. He, Y. Zhu, A. Epstein and Y. Mo, *Npj Comput. Mater.*, 2018, **4**, 18.

195 C. R. A. Catlow, *Computer Modeling in Inorganic Crystallography*, Elsevier, 1997.

196 P. Robert and A. Roux, *Spatiotemporal Anal. Resolv. Plasma Turbul. START Eur Space Agency WPP ESA WPP-047*, 1993, 289–293.

197 E. W. Dijkstra, *Numer. Math.*, 1959, **1**, 269–271.

198 Y. Mo, S. P. Ong and G. Ceder, *Chem. Mater.*, 2012, **24**, 15–17.
199 S. Ping Ong, Y. Mo, W. Davidson Richards, L. Miara, H. Sug Lee and G. Ceder, *Energy Environ. Sci.*, 2013, **6**, 148–156.
200 M. Aykol, S. Kim, V. I. Hegde, D. Snydacker, Z. Lu, S. Hao, S. Kirklin, D. Morgan and C. Wolverton, *Nat. Commun.*, 2016, **7**, 13779.
201 A. Sakuda, H. Kitaura, A. Hayashi, K. Tadanaga and M. Tatsumisago, *Electrochem. Solid-State Lett.*, 2008, **11**, A1–A3.
202 Z. Rong, D. Kitchaev, P. Canepa, W. Huang and G. Ceder, *J. Chem. Phys.*, 2016, **145**, 074112.
203 A. Jain, S. P. Ong, W. Chen, B. Medasani, X. Qu, M. Kocher, M. Brafman, G. Petretto, G.-M. Rignanese, G. Hautier, D. Gunter and K. A. Persson, *Concurr. Comput. Pract. Exp.*, 2015, **27**, 5037–5059.
204 G. Hautier, C. C. Fischer, A. Jain, T. Mueller and G. Ceder, *Chem. Mater.*, 2010, **22**, 3762–3767.
205 M. A. Green, *J. Appl. Phys.*, 1990, **67**, 2944–2954.
206 P. Canepa, G. Sai Gautam, D. Broberg, S.-H. Bo and G. Ceder, *Chem. Mater.*, 2017, **29**, 9657–9667.
207 A. F. Kohan, G. Ceder, D. Morgan and C. G. Van de Walle, *Phys. Rev. B*, 2000, **61**, 15019–15027.
208 S. H. Lee, B. K. Koo, J.-C. Kim and K. M. Kim, *J. Power Sources*, 2008, **184**, 276–283.
209 H. Lee, M. G. Kim and J. Cho, *Electrochem. Commun.*, 2007, **9**, 149–154.
210 S.-H. Kang and M. M. Thackeray, *Electrochem. Commun.*, 2009, **11**, 748–751.
211 G. Wang, X. Wang, L. Yi, L. Wang, R. Yu, M. Liu, D. Wang, Q. Ren and X. Yang, *RSC Adv.*, 2016, **6**, 46325–46335.
212 H. D. Lutz, W. Schmidt and H. Haeuseler, *J. Phys. Chem. Solids*, 1981, **42**, 287–289.
213 P. Hartwig, W. Weppner and W. Wichelhaus, *Mater. Res. Bull.*, 1979, **14**, 493–498.
214 R. Kanno, Y. Takeda and O. Yamamoto, *Solid State Ion.*, 1988, **28**, 1276–1281.
215 J. Fu, *Solid State Ion.*, 1997, **104**, 191–194.
216 A. Martínez-Juárez, C. Pecharromán, J. E. Iglesias and J. M. Rojo, *J. Phys. Chem. B*, 1998, **102**, 372–375.
217 Y. Li, W. Zhou, X. Chen, X. Lü, Z. Cui, S. Xin, L. Xue, Q. Jia and J. B. Goodenough, *Proc. Natl. Acad. Sci.*, 2016, **113**, 13313–13317.
218 Y. Deng, C. Eames, B. Fleutot, R. David, J.-N. Chotard, E. Suard, C. Masquelier and M. S. Islam, *ACS Appl. Mater. Interfaces*, 2017, **9**, 7050–7058.
219 Y. Hamon, A. Douard, F. Sabary, C. Marcel, P. Vinatier, B. Pecquenard and A. Levasseur, *Solid State Ion.*, 2006, **177**, 257–261.
220 H. Tang, Z. Deng, Z. Lin, Z. Wang, I.-H. Chu, C. Chen, Z. Zhu, C. Zheng and S. P. Ong, *Chem. Mater.*, 2018, **30**, 163–173.
221 J. A. Dean and N. A. Lange, Eds., *Lange's handbook of chemistry*, McGraw-Hill, 1999.
222 S. Seki, Y. Kobayashi, H. Miyashiro, Y. Mita and T. Iwahori, *Chem. Mater.*, 2005, **17**, 2041–2045.
223 N. Kuwata, N. Iwagami, Y. Matsuda, Y. Tanji and J. Kawamura, *ECS Trans.*, 2009, **16**, 53–60.
224 S. Yu, A. Mertens, H. Tempel, R. Schierholz, H. Kungl and R.-A. Eichel, *ACS Appl. Mater. Interfaces*, 2018, **10**, 22264–22277.

225 Ya. V. Baklanova, I. Yu. Arapova, A. L. Buzlukov, A. P. Gerashenko, S. V. Verkhovskii, K. N. Mikhalev, T. A. Denisova, I. R. Shein and L. G. Maksimova, *J. Solid State Chem.*, 2013, **208**, 43–49.
226 E. A. Sherstobitova, A. F. Gubkin, I. A. Bobrikov, A. V. Kalashnova and M. I. Pantyukhina, *Electrochimica Acta*, 2016, **209**, 574–581.
227 M. A. París, A. Martínez-Juárez, J. M. Rojo and J. Sanz, *J. Phys. Condens. Matter*, 1996, **8**, 5355–5366.
228 N. El Horr, A. Hammou and M. Bagieu, *J. Solid State Chem.*, 1991, **90**, 361–366.
229 F. Mounir, H.-N. Karima, B. S. Khaled and F. Mokhtar, *Phys. B Condens. Matter*, 2012, **407**, 2593–2600.
230 B. K. Money and K. Hariharan, *Appl. Phys. A*, 2007, **88**, 647–652.
231 F. Zhou, K. Kang, T. Maxisch, G. Ceder and D. Morgan, *Solid State Commun.*, 2004, **132**, 181–186.
232 J. P. Perdew, *Int. J. Quantum Chem.*, 1985, **28**, 497–523.
233 J. Wolfenstine, J. L. Allen, J. Sumner and J. Sakamoto, *Solid State Ion.*, 2009, **180**, 961–967.
234 R. Amin and Y.-M. Chiang, *J. Electrochem. Soc.*, 2016, **163**, A1512–A1517.
235 A. Schwöbel, R. Hausbrand and M. A. P. Jaegermann, *Solid State Ion.*, 2015, **273**, 51–54.
236 J. Chong, J. Zhang, H. Xie, X. Song, G. Liu, V. Battaglia, S. Xun and R. Wang, *RSC Adv.*, 2016, **6**, 19245–19251.
237 D.-H. Seo, J. Lee, A. Urban, R. Malik, S. Kang and G. Ceder, *Nat. Chem.*, 2016, **8**, 692–697.
238 Z. Lu and J. R. Dahn, *J. Electrochem. Soc.*, 2002, **149**, A815–A822.
239 A. R. Armstrong, M. Holzapfel, P. Novák, C. S. Johnson, S.-H. Kang, M. M. Thackeray and P. G. Bruce, *J. Am. Chem. Soc.*, 2006, **128**, 8694–8698.
240 G. Hautier, A. Jain, S. P. Ong, B. Kang, C. Moore, R. Doe and G. Ceder, *Chem. Mater.*, 2011, **23**, 3495–3508.
241 A. K. Padhi, K. S. Nanjundaswamy, C. Masquelier, S. Okada and J. B. Goodenough, *J. Electrochem. Soc.*, 1997, **144**, 1609–1613.
242 H. Ettis, H. Naïli and T. Mhiri, *J. Solid State Chem.*, 2006, **179**, 3107–3113.
243 M. Férid, K. Horchani, A. Touai, A. Madani, H. Boussetta and M. Trabetsi-Ayedi, *J. Phys. IV Proc.*, 2004, **113**, 115–118.
244 C. Wagner, *Prog. Solid State Chem.*, 1975, **10**, 3–16.
245 J. Yang, C. Bao, K. Zhu, T. Yu, F. Li, J. Liu, Z. Li and Z. Zou, *Chem. Commun.*, 2014, **50**, 4824–4826.
246 S.-C. Han, H.-S. Kim, M.-S. Song, J.-H. Kim, H.-J. Ahn and J.-Y. Lee, *J. Alloys Compd.*, 2003, **351**, 273–278.
247 T. Rhimi, G. Leroy, B. Duponchel, K. Khirouni, S. Guermazi and M. Toumi, *Ionics*, 2018, **24**, 1305–1312.
248 H.-S. Kim, Y. Kim, S.-I. Kim and S. W. Martin, *J. Power Sources*, 2006, **161**, 623–627.
249 K. Yoon, J.-J. Kim, W. M. Seong, M. H. Lee and K. Kang, *Sci. Rep.*, 2018, **8**, 8066.
250 A. M. Glass, K. Nassau and T. J. Negran, *J. Appl. Phys.*, 1978, **49**, 4808–4811.
251 S. W. Martin, *J. Am. Ceram. Soc.*, 1991, **74**, 1767–1784.
252 H. L. Tuller, D. P. Button and D. R. Uhlmann, *J. Non-Cryst. Solids*, 1980, **40**, 93–118.
253 G. Kresse and J. Furthmüller, *Comput. Mater. Sci.*, 1996, **6**, 15–50.
254 V. I. Anisimov, J. Zaanen and O. K. Andersen, *Phys. Rev. B*, 1991, **44**, 943–954.
255 G. Henkelman, B. P. Uberuaga and H. Jónsson, *J. Chem. Phys.*, 2000, **113**, 9901–9904.
256 J. B. Boyce and B. A. Huberman, *Phys. Rep.*, 1979, **51**, 189–265.

257 T. Xie and J. C. Grossman, *Phys. Rev. Lett.*, 2018, **120**, 145301.
258 J. Guo, H. Guo, A. L. Baker, M. T. Lanagan, E. R. Kupp, G. L. Messing and C. A. Randall, *Angew. Chem. Int. Ed.*, 2016, **55**, 11457–11461.
259 S. Smetaczek, A. Wachter-Welzl, R. Wagner, D. Rettenwander, G. Amthauer, L. Andrejs, S. Taibl, A. Limbeck and J. Fleig, *J. Mater. Chem. A*, 2019, **7**, 6818–6831.
260 S. Curtarolo, G. L. W. Hart, M. B. Nardelli, N. Mingo, S. Sanvito and O. Levy, *Nat. Mater.*, 2013, **12**, 191–201.
261 A. Jain, G. Hautier, C. J. Moore, S. Ping Ong, C. C. Fischer, T. Mueller, K. A. Persson and G. Ceder, *Comput. Mater. Sci.*, 2011, **50**, 2295–2310.